ARTICLE

Check for updates

Discovery of archaeal fusexins homologous to eukaryotic HAP2/GCS1 gamete fusion proteins

David Moi [1,2,3,14], Shunsuke Nishio [4,14], Xiaohui Li[5,14], Clari Valansi[5], Mauricio Langleib[6,7], Nicolas G. Brukman[5], Kateryna Flyak [5], Christophe Dessimoz[2,3,8,9], Daniele de Sanctis[10], Kathryn Tunyasuvunakool [11], John Jumper [11], Martin Graña [7✉], Héctor Romero [6,12✉], Pablo S. Aguilar [1,13✉], Luca Jovine [4✉] & Benjamin Podbilewicz [5✉]

Sexual reproduction consists of genome reduction by meiosis and subsequent gamete fusion. The presence of genes homologous to eukaryotic meiotic genes in archaea and bacteria suggests that DNA repair mechanisms evolved towards meiotic recombination. However, fusogenic proteins resembling those found in gamete fusion in eukaryotes have so far not been found in prokaryotes. Here, we identify archaeal proteins that are homologs of fusexins, a superfamily of fusogens that mediate eukaryotic gamete and somatic cell fusion, as well as virus entry. The crystal structure of a trimeric archaeal fusexin (Fusexin1 or Fsx1) reveals an archetypical fusexin architecture with unique features such as a six-helix bundle and an additional globular domain. Ectopically expressed Fusexin1 can fuse mammalian cells, and this process involves the additional globular domain and a conserved fusion loop. Furthermore, archaeal fusexin genes are found within integrated mobile elements, suggesting potential roles in cell-cell fusion and gene exchange in archaea, as well as different scenarios for the evolutionary history of fusexins.

[1] Instituto de Fisiología, Biología Molecular y Neurociencias (IFIBYNE-CONICET), Buenos Aires, Argentina. [2] Department of Computational Biology, University of Lausanne, Lausanne, Switzerland. [3] Swiss Institute of Bioinformatics, Lausanne, Switzerland. [4] Department of Biosciences and Nutrition, Karolinska Institutet, Huddinge, Sweden. [5] Department of Biology, Technion- Israel Institute of Technology, Haifa, Israel. [6] Unidad de Genómica Evolutiva, Facultad de Ciencias, Universidad de la República, Montevideo, Uruguay. [7] Unidad de Bioinformática, Institut Pasteur de Montevideo, Montevideo, Uruguay. [8] Department of Genetics, Evolution and Environment, Centre for Life's Origins and Evolution, University College London, London, UK. [9] Department of Computer Science, University College London, London, UK. [10] ESRF—The European Synchrotron, Grenoble, France. [11] DeepMind, London, UK. [12] Centro Universitario Regional Este - CURE, Centro Interdisciplinario de Ciencia de Datos y Aprendizaje Automático - CICADA, Universidad de la República, Montevideo, Uruguay. [13] Instituto de Investigaciones Biotecnológicas Universidad Nacional de San Martín (IIB-CONICET), San Martín, Buenos Aires, Argentina. [14] These authors contributed equally: David Moi, Shunsuke Nishio, Xiaohui Li. ✉email: mgrana@pasteur.edu.uy; eletor@fcien.edu.uy; paguilar@iib.unsam.edu.ar; luca.jovine@ki.se; podbilew@technion.ac.il

How early eukaryotes developed the capacity for gamete fusion is a central question entangled with the origin of the eukaryotic cell itself. The widespread presence of a conserved set of meiosis, gamete, and nuclear fusion proteins among extant eukaryotes indicates that meiotic sex emerged once, predating the last eukaryotic common ancestor (LECA)[1,2]. Two essential molecular events are required for meiotic sex: DNA recombination and plasma membrane fusion. Prokaryotic cells contain DNA repair machines that may have been precursors of the recombination machinery used in eukaryotic meiosis[1,2]. However, the genes encoding for proteins that are essential and sufficient to merge plasma membranes have not been identified in prokaryotes[3].

In eukaryotes, different families of cellular and viral fusion proteins (fusogens) have been described[3]. For example, class I viral fusogens include the spike glycoproteins of Influenza, HIV, Ebola, and SARS-CoV that have similar structures that appear to have converged during evolution as a way to merge viral and eukaryotic membranes[4–6]. More recently it was shown that myoblast fusion requires two unrelated proteins to form muscles in vertebrates[7,8]. However, many fusogens have not been identified yet, and the molecular basis of gamete fusion in fungi and vertebrates remain unclear[9].

The first eukaryotic cell–cell fusogen was discovered only two decades ago by genetic screens in C. elegans[10]. The fusogen EFF-1 and its paralog AFF-1 fuse one-third of all the somatic cells in the skin, excretory, reproductive, nervous and digestive systems of nematodes. The functions of these cellular fusions are to sculpt cells, tissues, and organs to restrict cellular fates for a robust development[11]. In the absence of sequence similarity between EFF-1, AFF-1, and other known proteins, predictions of the structure of AFF-1 suggested structural similarity to class II viral fusogens[12]. EFF-1 and AFF-1 can fuse cells in C. elegans, promote fusion between heterologous cells, and substitute a viral fusogen to mediate plasma membrane fusion only when these fusogenic proteins are expressed in both fusing membranes[13–15]. The crystal structure of the ectodomain of EFF-1 demonstrated structural similarity with class II viral fusogens such as the glycoproteins on the surface of Zika, dengue, and rubella viruses[16]. Thus, these eukaryotic and viral fusogens have remarkably similar functions and structures despite undetectable sequence similarity. However, their mechanisms of membrane fusion are different because EFF-1 and AFF-1 use a bilateral mechanism while class II viral fusogens use a unilateral mechanism[13–15].

More recently, genetic screens uncovered a protein involved in gamete fusion, HAP2/GCS1, which is conserved in Arabidopsis, Chlamydomonas, Plasmodium, Tetrahymena, and Dictyostelium[17–21]. Later, structural bioinformatics, crystallographic structure elucidation and functional assays demonstrated that HAP2/GCS1 is a bona fide fusogen homologous to EFF-1, AFF-1, and class II viral fusogens[22–24]. The crystal structures of HAP2/GCS1 from Chlamydomonas and Arabidopsis showed remarkable structural conservation without sequence similarity[23,25,26]. This superfamily of fusion proteins was named fusexins: fusion proteins essential for sexual reproduction and exoplasmic merger of plasma membranes[22–24]. Thus, the fusexin superfamily encompasses class II viral fusogens (viral fusexins) that fuse the envelope of some animal viruses with the membranes of host cells during infection[5,6]; EFF-1 and AFF-1 (somatic fusexins) that promote cell fusion during syncytial organ development[10,13,15,16]; and HAP2/GCS1 (sexual fusexins; hereafter referred to as HAP2) that mediate gamete fusion[17–19].

Although it is assumed that sexual fusexins were already present in the LECA[1,27], their shared ancestry with viral fusexins posed a "the virus or the egg" evolutionary dilemma[22,24,28]. In one scenario, fusexins are proper eukaryal innovations that were captured by some viruses and used for host invasion. Alternatively, a viral fusexin gene was transferred to an early eukaryotic cell and then repurposed for gamete fusion. Solving this evolutionary conundrum is not a trivial task because sequence-based phylogenetics cannot be applied to the whole fusexin superfamily due to lack of sequence conservation.

Here we identify a family of fusexins in genomes of Archaea and prokaryotic fractions of metagenomes from very diverse environments. We provide crystallographic and functional evidence suggesting that these proteins are cellular fusogens. Genomic analyses show that archaeal fusexins are carried by integrated mobile genetic elements. Evolutionary analyses of the whole fusexin superfamily reveal alternative working models regarding the relationships between viral, eukaryotic and archaeal fusexins and the emergence of meiotic sex during eukaryogenesis.

Results

Fusexin genes in Archaea. To search for fusexins we used the crystallographic structures of C. reinhardtii, A. thaliana, and T. cruzi HAP2 (Cr/At/TcHAP2)[23,25,26] to build dedicated Hidden Markov Models (HMMs) for scanning the Uniclust30 database. We detected 24 high-confidence candidates in prokaryotes: 8 belong to isolated and cultivated archaea, and the remaining 16 to metagenome-assembled genomes (MAGs, Supplementary Table 1). We then built HMMs of the candidate ectodomains and compared them to HMMs of sexual, somatic, and viral fusexins. Figure 1a shows that the prokaryotic candidates have detectable sequence similarities with HAP2, with E-values below 0.001 and HHblits-derived probabilities higher than 0.95 (Supplementary Fig. 1a). We named these proteins Fusexin1 (Fsx1). fsx1 genes found in cultivated and isolated prokaryotes are restricted to the Haloarchaea class (also called Halobacteria, Euryarchaeota superphylum) whereas MAGs containing Fsx1s include all major Archaea superphyla (Supplementary Table 1). Next, we used this Fsx1 sequence set to search the Metaclust database, which comprises 1.59 billion clustered proteins from over 2200 metagenomic/metatranscriptomic datasets. Performing a scan pipeline using PHMMER, PSI-BLAST, HMM–HMM comparisons and topology filtering we found 96 high-confidence fsx1 genes. The identified fsx1s come from different environments (with pre-eminence of saline samples) and a wide temperature range (−35 to 80 °C, see Supplementary Data 1).

Fsx1 is a structural homolog of HAP2/GCS1. To experimentally investigate the presence of fusexin-like proteins in Archaea, a selection of the candidate genes was expressed in mammalian cells (Supplementary Fig. 1b, c). High-level expression was observed for a metagenomic Fsx1 sequence from a hypersaline environment, predicted to encode a ~55 kDa ectodomain region (Fsx1$_E$) followed by three transmembrane domains (TMs) (Supplementary Data 1). Fsx1$_E$ is a monomer in solution but crystallized as a homotrimer in the presence of 2.5 M NaCl, 0.2 M CaCl$_2$ (Supplementary Fig. 2). These conditions precluded experimental phasing, and attempts to phase the data by molecular replacement (MR) with different kinds of homology models also failed, due to insufficient sequence identity to known fusexin structures. However, we could determine the structure of Fsx1$_E$ at 2.3 Å resolution by running MR with a combination of fragments from ab initio predictions generated by AlphaFold2[29] (Fig. 1b, Supplementary Figs. 3, 4 and Supplementary Table 2).

The Fsx1$_E$ homotrimer has overall dimensions of 119 × 77 × 76 Å (Fig. 1b). Each protomer consists of four domains (Fig. 2a, b), the first three of which match the approximate dimensions and relative arrangement of domains I–III of known fusexins in their post-fusion conformation[30]; accordingly, fold
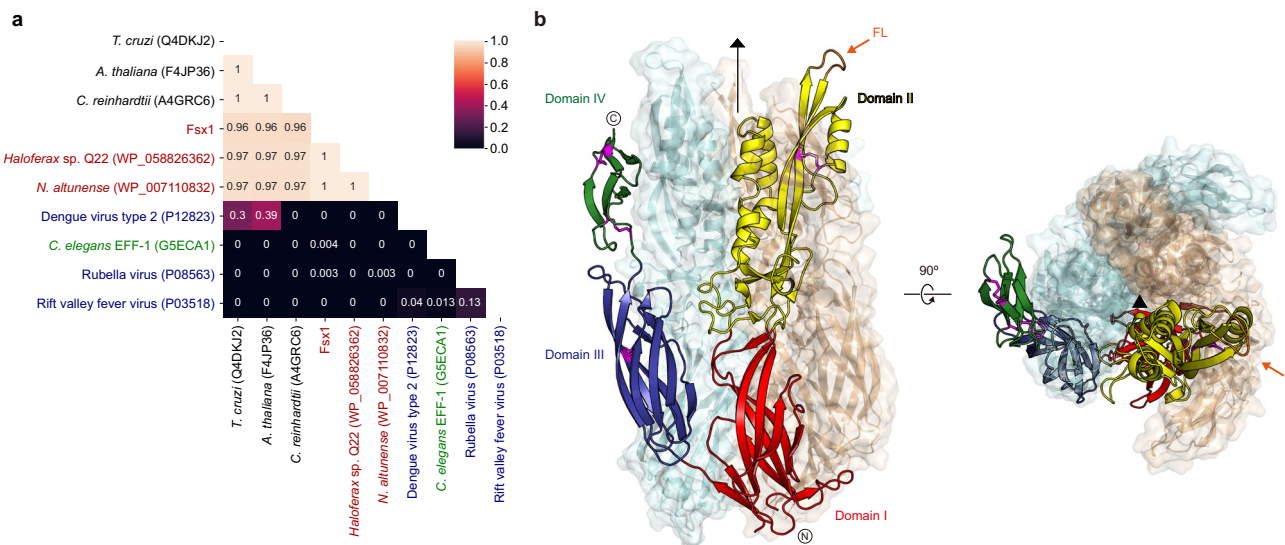
Fig. 1 Fsx1 is a member of the fusexin protein superfamily. a HMM vs. HMM homology probabilities of a subset of eukaryotic, viral, and archaeal fusexin ectodomains. With exception of Fsx1, which derives from a metagenomic sequence, archaeal fusexins (red), viral fusexins (blue), EFF-1 (green) and HAP2s (black) are indicated by RefSeq/UniProt identifiers. **b** Crystal structure of the trimeric ectodomain of Fsx1. The three-fold non-crystallographic axis is indicated. Subunit A is shown as a cartoon colored by domain, with disulfides and the fusion loop (FL) colored magenta and orange, respectively; subunits B, C are in mixed cartoon/surface representation.

and interface similarity searches identify HAP2 as the closest structural homolog of $Fsx1_E$, followed by viral fusexins and *C. elegans* EFF-1 (Fig. 2c, d). Fsx1 domains I and III are relatively sequence-conserved among archaeal homologs (Supplementary Figs. 5a and 6) and closely resemble the corresponding domains of HAP2 (RMSD 2.1 Å over 218 Cα), including the invariant disulfide bond between domain III strands βC and βF[23] ($C_3389–C_4432$; Fig. 2, Supplementary Fig. 4c). On the other hand, Fsx1 domain II shares the same topology as that of HAP2 but differs significantly in its secondary structure elements and their relative orientation, as well as disulfide bonds (Fig. 2c). In particular, Fsx1 domain II is characterized by a four-helix hairpin, whose N-terminal half interacts with the same region of the other two subunits to generate a six-helix bundle around the molecule's three-fold axis (Figs. 1b and 3a–c and Supplementary Figs. 4a and 5b, c).

Notably, unlike previously characterized viral and eukaryotic fusexins, Fsx1 also contains a fourth globular domain conserved among archaeal homologs (Figs. 1b, 2 and Supplementary Figs. 4d and 6). Its antiparallel β-sandwich, which includes the two C-terminal disulfides of Fsx1, resembles the carbohydrate-binding fold of dust mite allergen Der p 23 and related chitin-binding proteins[31] (Fig. 3d); accordingly, it is also structurally similar to a high-confidence AlphaFold2 model of the C-terminal domain of acidic mammalian chitinase[32]. In addition to being coaxially stacked with domain III as a result of a loop/loop interaction stabilized by the $C_5457–C_6477$ disulfide, domain IV contributes to the quaternary structure of the protein by interacting with domain II of the adjacent subunit to which domain III also binds (Figs. 1b and 3c).

The $Fsx1_E$ monomer has a net charge of −67, and another feature stabilizing its homotrimeric assembly is a set of Ca^{2+} and Na^+ ions that interacts with negatively charged residues at the interface between subunits (Fig. 3a–c and Supplementary Figs. 4a and 5b). Additional metal ions bind to sites located within individual subunits; in particular, a Ca^{2+} ion shapes the conformation of the domain II cd loop (S143-V148) so that its uncharged surface protrudes from the rest of the molecule (Fig. 3e, f and Supplementary Fig. 5d). Strikingly, the position of

this element matches that of the fusion loops (FLs) of other fusexins, including the Ca^{2+}-binding fusion surface of rubella virus E1 protein[33,34] (Fig. 3e). Moreover, as previously observed in the case of CrHAP2[26], the loops of each trimer interact with those of another trimer within the Fsx1 crystal lattice.

In summary, despite significant differences in the fold of domain II, the unprecedented presence of a domain IV and extreme electrostatic properties, the overall structural similarity between Fsx1 and viral or eukaryotic fusexins suggests that this prokaryotic molecule also functions to fuse membranes.

Fsx1 can fuse eukaryotic cells. To test the fusogenic activities of the candidate archaeal fusexins we studied their fusion activity upon transfection in eukaryotic cells[15,16,22]. Cells with either red or green nuclei are mixed with each other and fusion is measured by the formation of hybrid cells with both red and green nuclei revealing merger of their cytoplasms. For this, we co-cultured two batches of Baby Hamster Kidney (BHK) cells independently transfected with Fsx1 and co-expressing either nuclear H2B-RFP or H2B-GFP[22]. We then performed immunofluorescence against a V5 tag fused to the cytoplasmic tail of Fsx1 (Fig. 4a, b, and Supplementary Fig. 7a, b). We observed a five-fold increase in the mixing of the nuclear H2B-GFP and H2B-RFP compared to vector control, showing that Fsx1 is a bona fide fusogen, as efficient as the fusexin AtHAP2 (Fig. 4c). To determine whether Fsx1 expression is required in both fusing cells or, alternatively, it suffices in one of the fusing partners, we mixed BHK-Fsx1 coexpressing cytoplasmic GFP with BHK cells expressing only nuclear RFP. We found increased multinucleation of GFP+ cells (revealing cell–cell fusion) but very low mixing with RFP+ cells not expressing Fsx1. In contrast, the vesicular stomatitis virus G-glycoprotein (VSVG) fusogen-induced efficient unilateral fusion[15] (Fig. 4d–f). While VSVG requires acidic pH for maximum fusion activity Fsx1-mediated multinucleation was not stimulated by low pH (Supplementary Fig. 1e). Thus, Fsx1 acts in a bilateral way, similarly to EFF-1 and AFF-1 fusexins[14,15,35]. We then performed live imaging using spinning disk confocal microscopy and observed bilateral cell-cell fusion of BHK-Fsx1 cells (Fig. 4g, h).
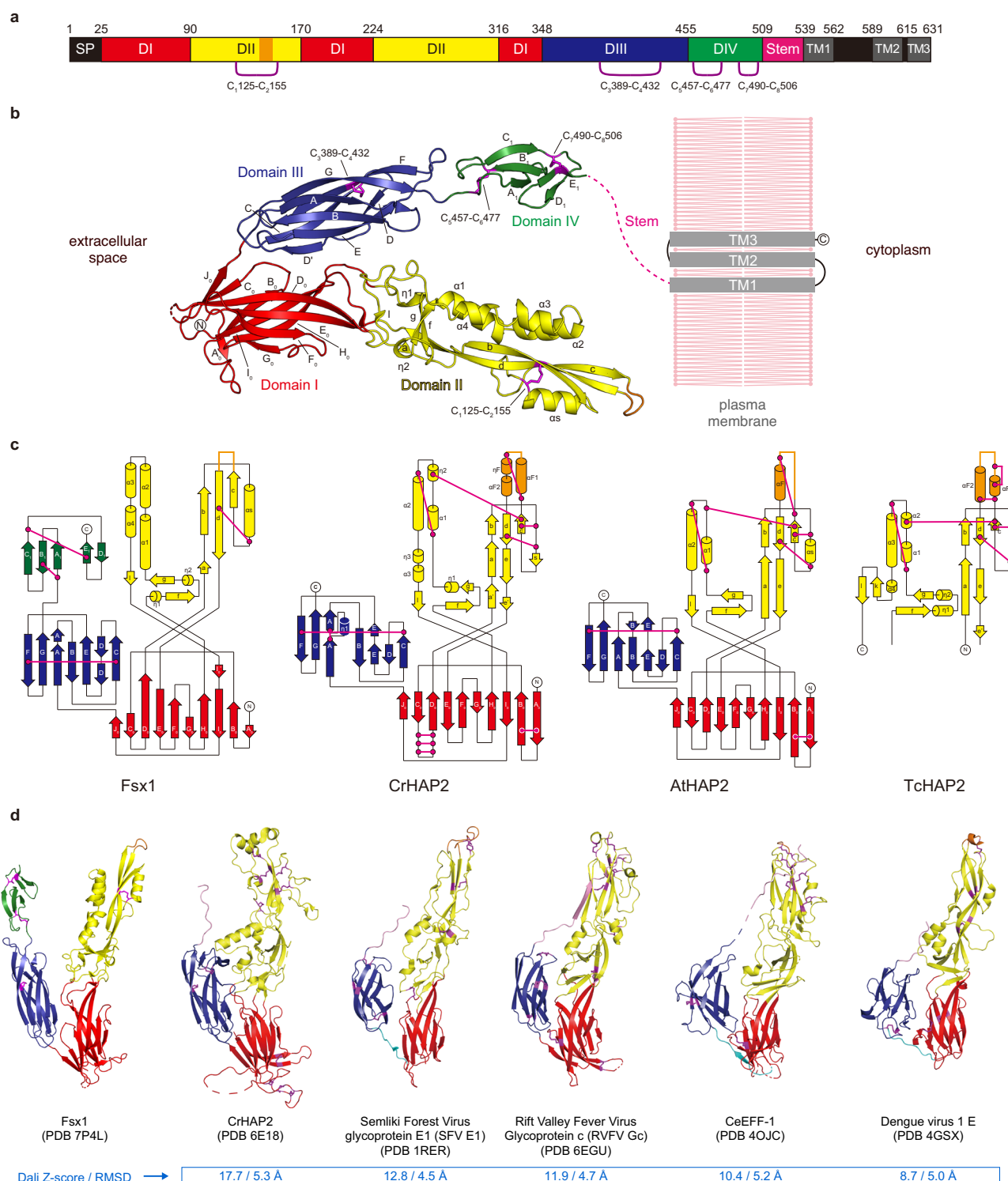
Fig. 2 Domain architecture of Fsx1 and topological comparison with HAP2. a Schematic diagram of the domains of Fsx1. SP, signal peptide; TM, predicted transmembrane helices. Note that Fsx1 is predicted to contain three C-terminal TMs, with a cytoplasmic loop between TM1 and TM2 that lacks Cys residues; on the other hand, HAP2 homologs are characterized by having a single TM, followed by a cytoplasmic tail that often contains Cys implicated in fusion[64]. **b** Crystal structure of the ectodomain of Fsx1 and predicted topology of the full-length protein relative to the plasma membrane. Domains I–IV are shown in red, yellow, blue, and green, respectively; disulfide bonds are indicated and colored magenta. **c** Topology diagrams of the ectodomains of Fsx1, *C. reinhardtii* HAP2 (PDB 6E18 [https://www.rcsb.org/structure/6E18])[65], *A. thaliana* HAP2 (PDB 5OW3 [https://www.rcsb.org/structure/5OW3])[25], and *T. cruzi* HAP2 (PDB 5OW4 [https://www.rcsb.org/structure/5OW4])[25]. Domains and disulfide bonds are colored as in panel **b**. Note how, although domain II of Fsx1 has the same topology as the corresponding domain of HAP2, it contains only one of its conserved disulfide bonds ($C_1 125$–$C_2 155$, corresponding to C147-C210/disulfide bond 3 of CrHAP2[23]). **d** Side-by-side comparison of Fsx1$_E$ and known class II fusogens. Elements are colored as in panel **b**; the stem region and the linker between domains I and III are shown in pink and cyan, respectively.
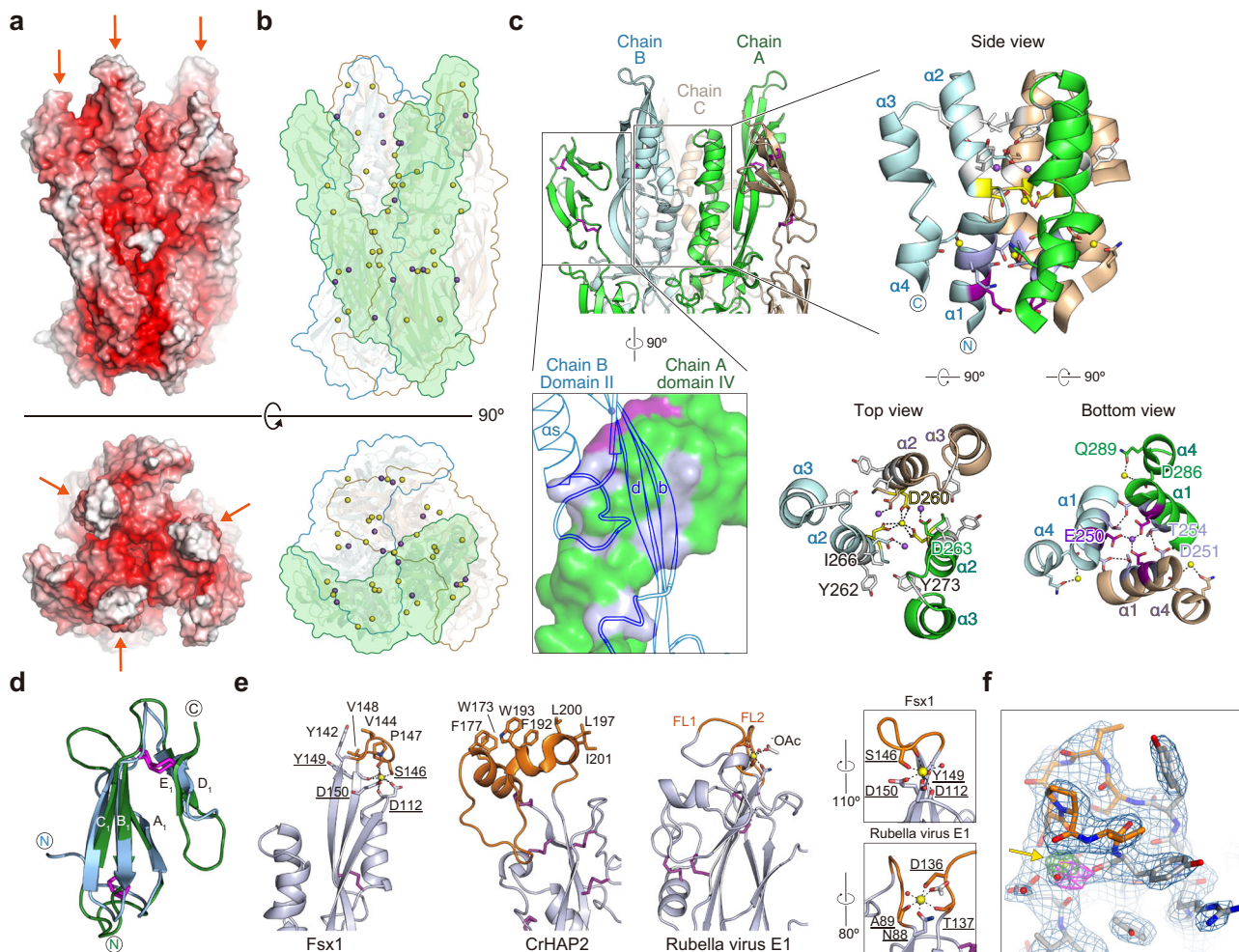
Fig. 3 Distinct structural features of Fsx1. a Fsx1$_E$ surface colored by electrostatic potential from red (-10 kT/e) to blue ($+10$ kT/e) through white (0 kT/e). Orange arrows indicate the FLs. **b** Location of the Ca^{2+} and Na$^+$ ions (depicted as yellow and purple spheres, respectively; see also Supplementary Figs. 4 and 5) stabilizing the Fsx1$_E$ trimer. The molecular surface of a protomer is shaded green and the outline of the other two subunits is colored cyan and wheat. **c** Details of interactions at the level of the six-helical bundle made by domain II of the Fsx1 subunits (right subpanels) and the domain IV/domain II interface (bottom left subpanel). Selected side chains are colored by the type of inter-chain contacts in which they are involved (gray: hydrophobic interaction; blue bell: hydrogen bonding; yellow: Ca^{2+} coordination; fuchsia: Na$^+$ coordination), with dashed lines indicating hydrogen bonds. Note that the helical bundle of Fsx1 is not a leucine-zipper coiled-coil structure, such as those found in class I/III viral fusion proteins or in the SNARE four-helix bundles, and see also Supplementary Fig. 5b. **d** Superposition of Fsx1 domain IV (green) and Der p 23 (PDB 4ZCE [https://www.rcsb.org/structure/4ZCE][31], blue) (Dali Z-score 3.6, RMSD 2.2 Å). **e** Comparison of the Fsx1 region that includes the FL and the corresponding parts of CrHAP2 and Rubella virus E1 protein (PDB 4B3V [https://www.rcsb.org/structure/4B3V][33]). Residues coordinating the Ca^{2+} ion that stabilizes the Fsx1 FL are underlined, and compared to the E1 protein Ca^{2+}-binding region in the boxed panels on the far right. **f** The Fsx1 FL adopts a highly ordered conformation stabilized by a Ca^{2+} ion. Presence and identity of the latter, indicated by a yellow arrow, are supported by two other maps shown in addition to the 2mFo-DFc map (blue mesh, contoured at 1.0 σ): a difference map calculated upon omitting all metal ions from the model (thick green(+)/red($-$) mesh, 6.0 σ) and a phased anomalous difference map calculated from a 2.9 Å-resolution dataset collected at 7.1 keV (thick magenta mesh, 3.2 σ).

Structure–function analysis of Fsx1. To compare archaeal Fsx1 activity with fusexins from eukaryotes and viruses, we introduced mutations into three different structural domains of Fsx1 and tested surface expression and fusogenic activity in mammalian cells.

First, to test whether the putative FL of Fsx1 (143-SVTSPV-148) is involved in fusion, we replaced it with a linker of 4G between Y142A and Y149A (Figs. 3e, 5a, and Supplementary Fig. 5d; ΔFL → AG$_4$A). This replacement does not affect surface expression yet reduces cell–cell fusion to levels similar to those of the negative control (Fig. 5b–f).

Second, we asked whether domain IV, which is only present in archaeal fusexins, has a function in the fusion process. For this, we replaced the entire domain with the stem region of EFF-1 (Figs. 3d and 5a; ΔDIV → EFF-1 stem). While this mutant Fsx1 reaches the cell surface, suggesting that it folds normally, it

shows a significantly reduced activity compared to wild-type Fsx1 (Fig. 5b–f).

Third, to test whether the three TMs of Fsx1 are required for fusion, we replaced them with the TM and cytoplasmic domains of EFF-1 (Fig. 5a; ΔTMs → EFF-1 TM) or a glycosylphosphatidylinositol (GPI) anchor signal (Fig. 5a; ΔTMs → GPI). We found that both Fsx1 mutants remained active (Fig. 5b), indicating that the Fsx1 TMs are not essential for fusion. Finally, we also replaced the TM and cytoplasmic domains of AtHAP2 with a signal for GPI and found that the protein also maintained its fusogenic activity (Figs. 4c, and 5a, b). Thus, contrary to some viral fusogens in which the GPI-anchored glycoproteins fail to drive complete fusion[36–38], lipid-anchored Fsx1 or eukaryotic HAP2 promote syncytia formation when expressed on the surface of BHK cells.
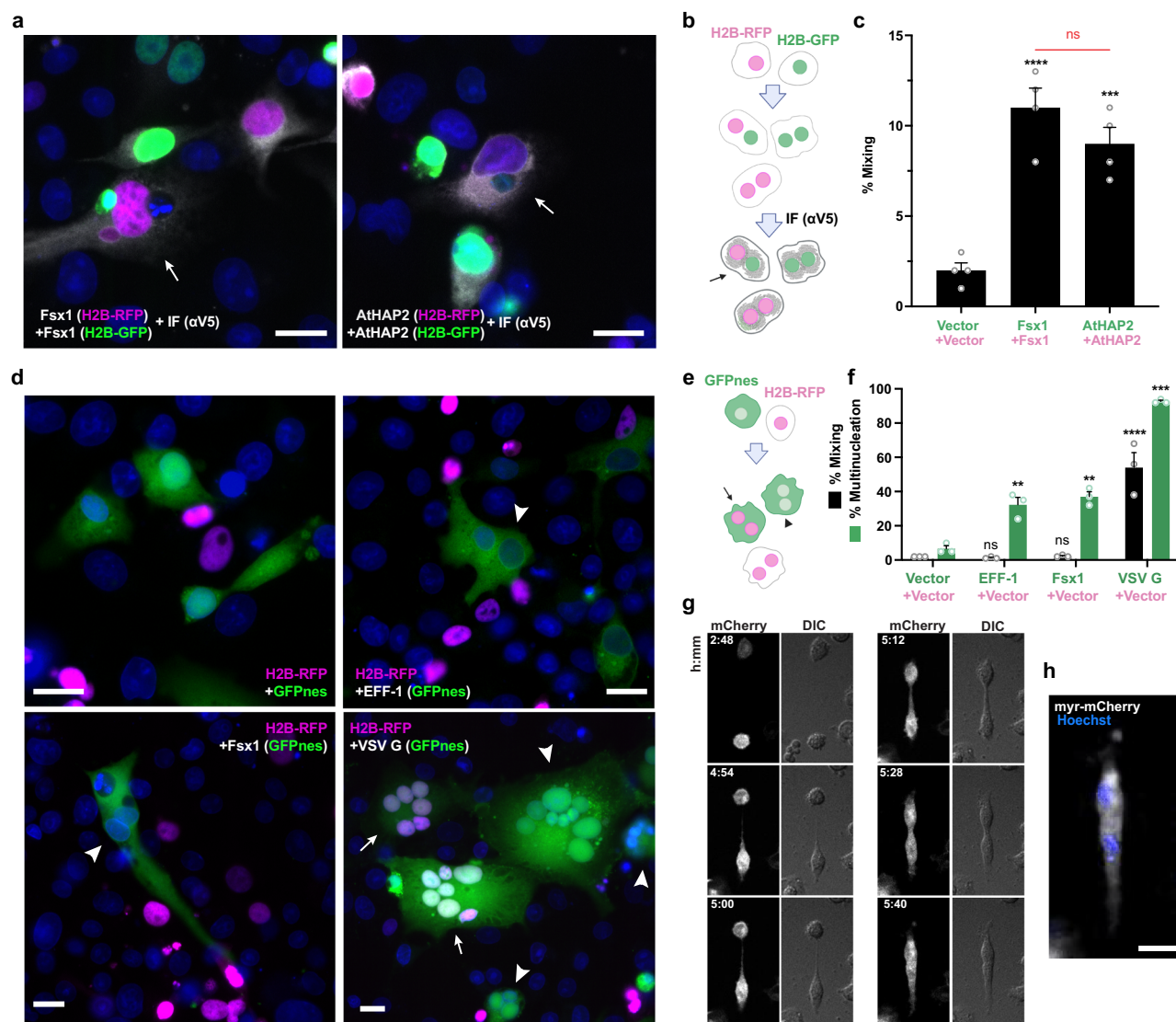
Fig. 4 Fsx1 mediates bilateral cell–cell fusion. a–c Cell–cell fusion was measured by content-mixing, indicated by the appearance of multinucleated cells containing green nuclei (H2B-GFP) and magenta nuclei (H2B-RFP). Immunofluorescence against the V5 tag was also performed (gray). **a** Images of mixed cells. DAPI, blue. Scale bars, 20 μm. See also Supplementary Fig. 7a. **b** Scheme of experimental design. **c** Quantification of content-mixing. The mixing indices presented as means ± SEM of four independent experiments. Comparisons by one-way ANOVA followed by Bonferroni's test. ns = non-significant, ***$p < 0.001$, ****$p < 0.0001$. Source data are provided as a Source Data file. **d–f** Unilateral fusion was evaluated by mixing control cells expressing nuclear H2B-RFP (magenta) with cells expressing GFP with a nuclear export signal (GFPnes, green cytoplasm) only or together with Fsx1, EFF-1 or VSV G. **d** Images of cells transfected with empty::GFPnes vector, Fsx1::GFPnes, EFF-1::GFPnes or VSV G::GFPnes. Fsx1 and EFF-1 show multinucleated GFPnes positive cells (arrowheads). VSV G multinucleated cells are found with GFP only (arrowheads) or with both markers (arrows). Scale bars, 20 μm. See also Supplementary Fig. 7e. **e** Scheme of experimental design. **f** Quantification of content-mixing experiments in which only the GFP population of cells express Fsx1, EFF-1, VSV G, or none of them (vector). Bar chart showing means ± SEM of three independent experiments. Comparisons by one-way ANOVA followed by Dunett's test against the vector. ns = non-significant, **$p < 0.01$, ***$p < 0.001$, ****$p < 0.0001$. Source data are provided as a Source Data file. **g** Spinning disk microscopy time-lapse images indicating the merging of two cells expressing myr-mCherry and Fsx1. Time in hours:minutes. The red channel (mCherry, white) and the DIC are shown. Refer to Supplementary Movie 1. **h** For the last point a Z-projection showing the myr-mCherry fluorescence (white) and the nuclei Hoechst (blue; Supplementary Movie 2). Scale bar, 20 μm.

Fsx1s are ancient fusogens associated with integrated mobile elements. The *fsx1* genes here identified are present in a wide physicochemical landscape (Fig. 6a). We observed that the branching pattern of Fsx1 sequences from complete genomes is incompatible with their species tree (Fig. 6a, b). This and the sparse pattern of Fsx1 presence in Archaea led us to perform genomic comparisons of related species with and without the *fsx1* gene. These revealed >50 kbp DNA insertions in the genomes of species with *fsx1* genes (Fig. 7a). To investigate them, we performed k-mer spectrum analysis on *fsx1*-containing Pure Culture

Genomes (PCGs) and found divergent regions containing the *fsx1* ORF (Fig. 7b). Gene content analyses of *fsx1*-containing regions show that they share a portion of their genes (Supplementary Fig. 9) and display conserved synteny (Fig. 8), suggesting common ancestry. These regions are enriched in ORFs homologous to proteins involved in DNA mobilization and integration (Fig. 8 and Supplementary Table 3). Thus, our results indicate that *fsx1* genes are contained in integrated mobile elements (IMEs) that can be mobilized by a conjugative-like, cell fusion-dependent mechanism.
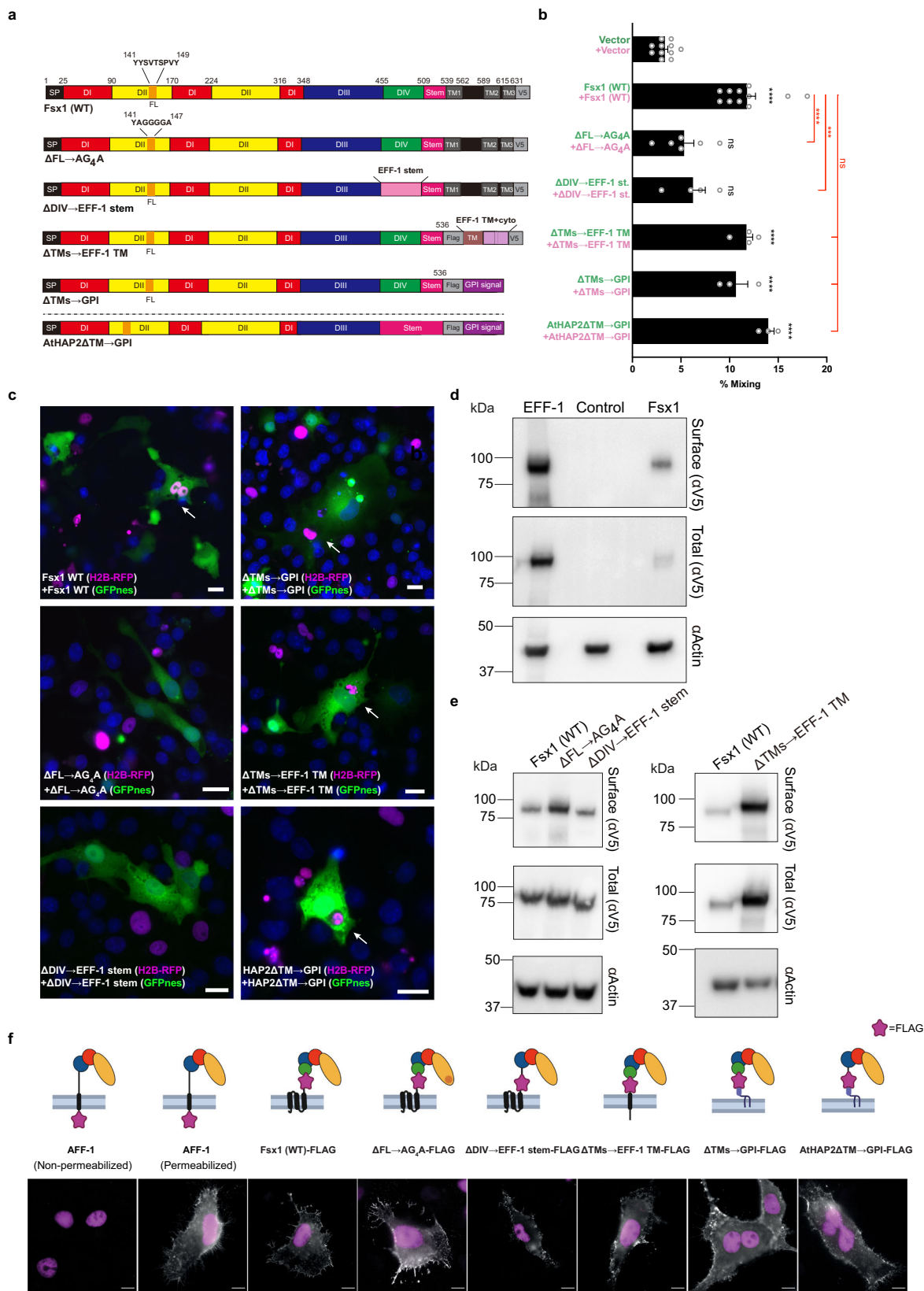
To describe Fsx1's tempo and mode of evolution we first compared archaeal and sexual fusexins, which share enough sequence conservation to apply standard phylogenetic analyses, not possible for somatic and viral fusexins, as these methods are not able to cope with such amount of divergence (Fig. 1a

and Supplementary Fig. 1a). We built maximum likelihood (ML) phylogenies for a set of Fsx1 sequences derived from isolated species and metagenomes, and a subset of HAP2s which capture the full phylogenetic diversity present in eukaryotic lineages (Supplementary Fig. 10a). A major finding

Fig. 5 Structure–function analysis of Fsx1. a Schematic diagram of wild-type Fsx1, four mutants and AtHAP2ΔTM → GPI. SP signal peptide, FL fusion loop. For colors and abbreviations see legend of Fig. 2. **b** Quantification of content-mixing (cell–cell fusion) in populations of cells expressing vectors ($n = 7$), Fsx1 (wt) ($n = 7$), its mutants (ΔFL → AG$_4$A ($n = 6$), ΔDIV → EFF-1 stem ($n = 4$), ΔTMs → EFF-1 TM ($n = 4$), ΔTMs → GPI ($n = 3$), or AtHAP2ΔTM → GPI ($n = 3$). Bar chart showing means ± SEM. Comparisons by one-way ANOVA followed by Bonferroni's test against the vector (black) and against Fsx1 (red). ns = non-significant, ***$p < 0.001$, ****$p < 0.0001$. Source data are provided as a Source Data file. **c** Representative merged images from the experiments in (**b**): magenta (RFP); green (GFP) and blue (DAPI). Fused cells with RFP and GFP (arrows). Scale bars, 20 μm. See also Supplementary Fig. 7f. **d** Immunoblot of EFF-1-V5, control (untransfected cells) and Fsx1-V5 expressing cells. "Surface" indicates surface biotinylation followed by affinity purification using neutravidin agarose beads; "Total" indicates the expression in whole cell extracts. Actin is used as a loading control. The amount of initial cells for Fsx1 is 4 times higher than EFF-1. $n = 3$. **e** Surface biotinylation as explained in panel **d** for cells expressing Fsx1-V5 (WT), ΔFL → AG$_4$A-V5, ΔDIV → EFF-1 stem-V5 or ΔTMs→EFF-1 TM-V5. $n = 3$. **f** Immunofluorescence images on non-permeabilized cells expressing Fsx1-FLAG (WT), AFF-1-FLAG (negative control, cytotail), Fsx1-ΔFL → AG$_4$A-FLAG, Fsx1-ΔDIV → EFF-1 stem-FLAG, AFF-1-FLAG (permeabilized), Fsx1-ΔTMs → EFF-1 TM-FLAG, Fsx1-ΔTMs → GPI and AtHAP2-ΔTM → GPI. The FLAG tag was inserted before the first TM or the GPI signal of each construct except for *C. elegans* AFF-1 in which the FLAG is at C-terminal after the cytoplasmic tail. Transfected BHK cells were incubated with anti-FLAG antibody on ice before fixation. Non-permeabilized staining of FLAG antibody showed the surface expression of Fsx1 and the mutants. *C. elegans* AFF-1 tagged with a cytoplasmic FLAG is a negative control for non-permeabilized staining. Permeabilized staining of CeAFF-1-FLAG shows the localization on plasma membrane and internal compartments (see also Supplementary Fig. 7g). Scale bars, 10 μm.

comes from these phylogenies: eukaryal and archaeal fusexins cluster into strongly supported clades suggesting they diverged before LECA.

To place *fsx1* in the broader fusexin superfamily context, we performed structural phylogenetic analysis comparing crystal structures from viral, somatic, and eukaryotic gamete fusogens (Supplementary Fig. 10b). This structure-based tree supports a viral origin of somatic fusexins (EFF-1)[16] and is also compatible with archaeal fusexins appearing before the radiation of eukaryotes.

Discussion

All *fsx1* genes found in cultured and isolated genomes are restricted to the Haloarchaea clade. Although 83% of *fsx1* genes were found in saline environments, they are not restricted to a particular niche, neither geographically nor environmentally and, by extension, potentially not restricted to halophilic archaea (Supplementary Data 1 and Fig. 6a). Only 16 out of 88 *fsx1* metagenomic genes have taxonomy assigned. The 16 MAG-containing fusexins are distributed in other archaeal clades (including Asgard) and also in bacteria but we take those taxonomic assignments with caution. *fsx1*-containing MAGs are highly fragmented and were assembled using methods that include sequence composition (k-mer) criteria, allocating scaffolds with similar k-mer spectra into MAGs. As *fsx1* genes from PCGs are located within distinctive k-mer regions and the metagenomic contigs containing the *fsx1* gene are compositionally homogeneous, and plausibly are also IMEs, it is quite possible that MAG-fusexins are misassigned. The association of haloarchaeal *fsx1s* with IMEs (Fig. 8), genomic comparisons of close species (Fig. 7a) and the incompatibility between their sequence phylogeny and cognate species tree (Fig. 6), indicate lateral mobility within the Haloarchaea class. This evidence suggests that Fsx1s mediate a cell fusion-dependent genetic exchange in archaea. This hypothesis is consistent with the genetic structure and lifestyle of halophilic archaea which are notorious for being polyploid[39] and undergoing massive genetic exchanges that overcome species and genera barriers[40,41]. Moreover, compelling evidence of archaeal cell fusion comes from studies showing bilateral DNA exchange that correlates with cytoplasmic bridges made up of fused lipid bilayers connecting haloarchaeal cells[42–44]. Thus, it is plausible that Haloarchaea evolved HGT mechanisms based on conjugative-like DNA mobilization and cell–cell fusion[45].

The "virus or the egg" dilemma[28] posits that fusexins may have been either viral innovations (class II fusogens), later acquired by eukaryotes, or vice versa. Archaeal fusexins expand this dilemma:

gamete fusogens may have prokaryotic origins. Both structure- and sequence-based trees (Supplementary Fig. 10) do not solve but provide insights to address this conundrum, in which we distinguish three main hypotheses indicating alternative origins: Virus, Eukarya, and Archaea (Fig. 9). For all three scenarios we assume that sexual fusexins (HAP2) were present in the LECA[1,27].

A Virus-first scenario has circumstantial evidence favoring it. Exaptation of viral genes is documented for all three domains of life[46]. To be consistent with the observed basal divergence between archaeal and eukaryal (HAP2) fusexins (Supplementary Fig. 10a) the Virus-first hypothesis must include two HGT events before the eukaryal radiation (Fig. 9a). Thus, an archaeon could have exapted a fusexin from an enveloped archaeal virus and then transferred it to an early eukaryote. The reciprocal is also formally possible: an eukaryal viral fusexin was exapted by a pre-LECA eukaryotic cell and then transferred to an archaeon, before the eukaryal radiation. Alternatively, the ancestral fusexin-containing virus was able to infect both archaea and eukaryal cells (Fig. 9a). These putative events are at odds with the distribution of fusexins in extant viruses. All currently known viral fusexins belong to RNA viruses that are confined to a few multicellular hosts: vertebrates, arthropods, and flowering plants[47,48]. This distribution favors a scenario where viral fusexins, like many other eukaryotic viral proteins, have eukaryotic cellular origins[49]. Unlike currently known fusexin-containing viruses, all isolated archaeal viruses to date have DNA genomes. The recently elucidated structure of VP5, a haloarchaeal virus envelope protein that mediates cell invasion shows a fold that differs from all previously known viral fusion proteins, including fusexins[50]. Although there is no evidence for the presence of fusexins in archaeal viruses, upcoming metagenomic and structural analyses may provide support to the Virus-first hypothesis.

The widespread presence of sexual fusexins in Eukarya indicates evolutionary success, in line with the Eukarya-first hypothesis (Fig. 9b). However, introduction of an eukaryal fusexin into the Archaeal domain is less supported by currently available evidence as interdomain gene transfers from eukaryotes to archaea are hardly documented and thought to be scarce[45,51].

The presence of *fsx1* genes in Haloarchaea IMEs is consistent with gene transfer in the opposite direction. Eukaryogenesis, and by extension the emergence of sex, is marked by massive horizontal gene transfer events to the archaeal ancestor of eukaryotes[52], disregarding if it belonged to the Asgard super-phylum or to a sister group of Archaea[53]. During the First
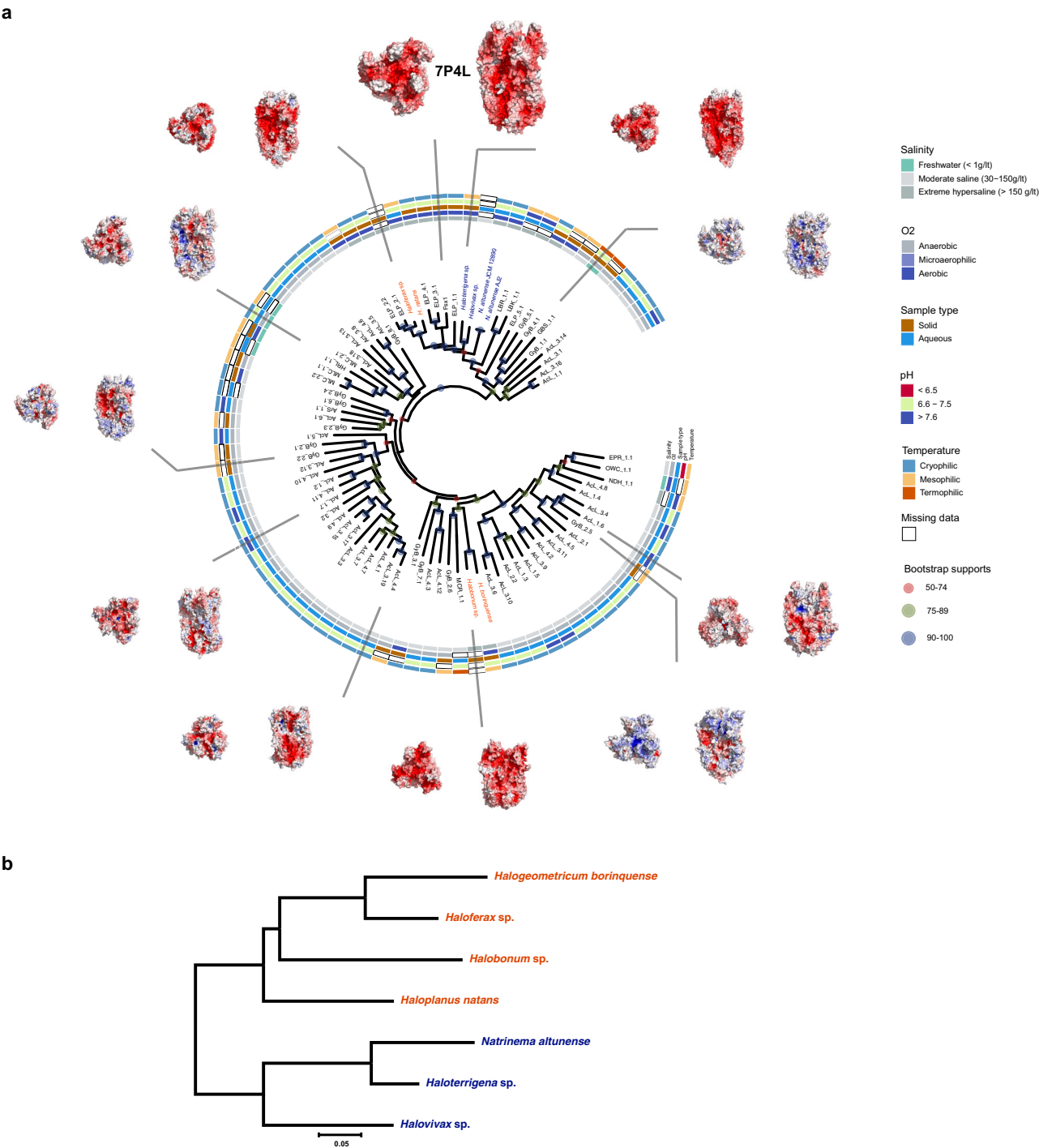
Fig. 6 Environmental distribution of Fsx1s. a Archaeal fusexins unrooted phylogeny, environmental details, and trimeric models[66] based on the Fsx1 X-ray structure (PDB 7P4L [https://www.rcsb.org/structure/7P4L], enlarged). Tree tip IDs coming from metagenomic data coded by sampling site, sample id and sequence (see Supplementary Data 1). Fsx1s from cultivated genomes are shown as Natrialbales and Haloferacales orders in blue and red, respectively. Surfaces colored and oriented as in Fig. 3a. Found in diverse environments and often differing in global surface properties, modeled trimers share hydrophobic tips. **b** Panel with phylogenomic tree for *fsx1*-containing cultured archaeal species, showing incongruences between Fsx1s in Haloferacales.

Eukaryotic Common Ancestor (FECA) to LECA transition, in addition to the alphaproteobacterial endosymbiont-related inherited genes, the pre-LECA received hundreds of archaeal genes from other lineages, including Euryarchaeota[54]. Thus, an Archaea-first hypothesis (Fig. 9c) considers horizontal transfer of archaeal fusexins into the ancestor of eukaryotes. A weakness of this hypothesis is the sparse distribution of fusexins in archaeal genomes. This distribution is not a product of a recent

HGT from Eukarya, as phylogenetic analysis indicates basal divergence between eukaryotic and archaeal fusexins (Supplementary Fig. 10a). Lateral mobility of extant *fsx1* genes within Haloarchaea, their relative confinement to few archaeal lineages and their basal divergence from sexual fusexins suggests they are molecular relics, and that cell fusion-based HGT might have declined during archaeal evolution in favor of conjugation, transduction and transformation.
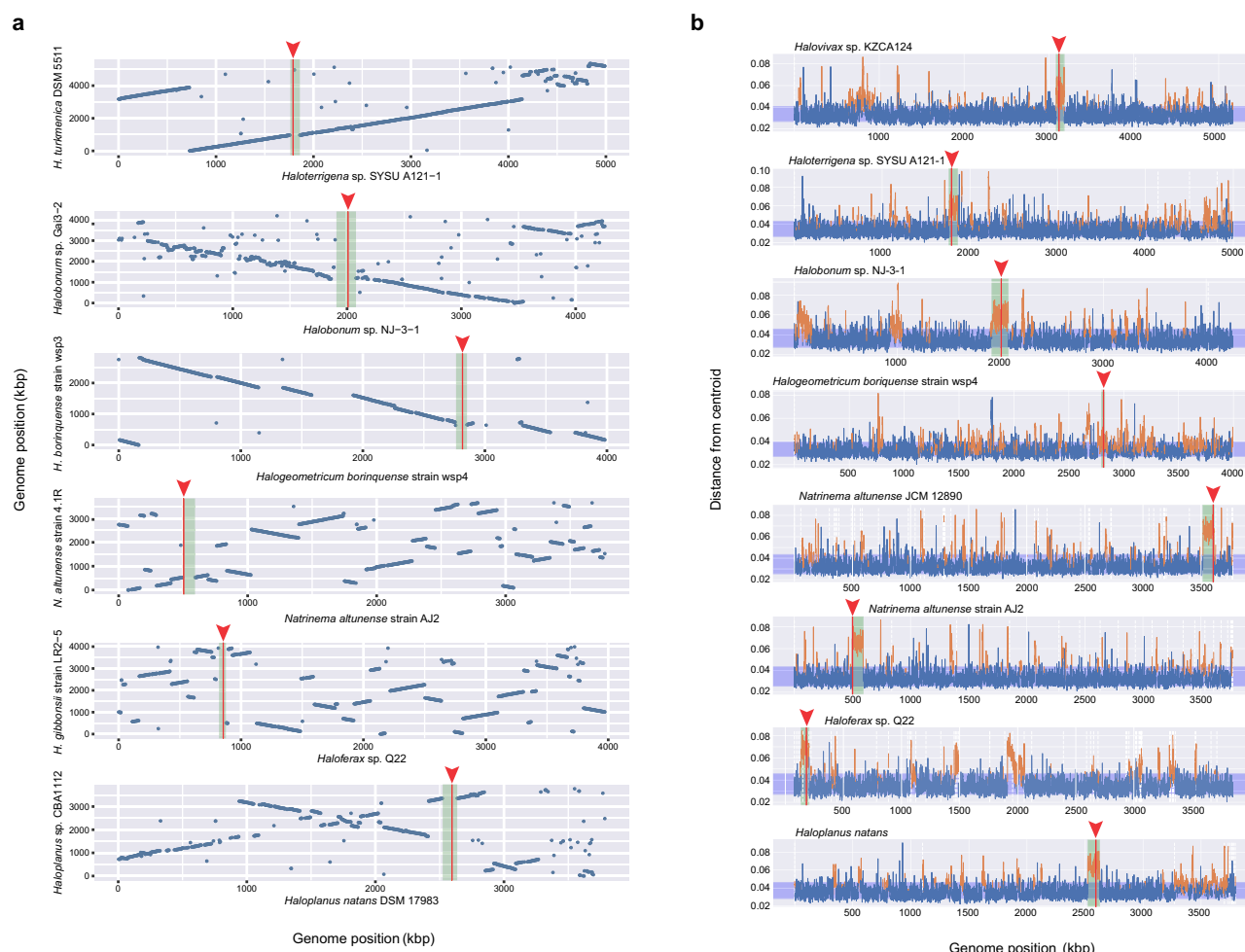
Fig. 7 Genomic features of Fsx1s. a Whole genome comparison of species with and without *fsx1*. Each blue dot represents a segment of 500 bp with more than 80% identity between the species harboring *fsx1* (e.g., *Haloplanus natans* DSM 17083) and the species with no *fsx1* (e.g., *Haloplanus* sp. CBA1112, see Supplementary Table 4). Species with *fsx1* are in the *x*-axis, the base of the green rectangles represent the detected IME carrying the *fsx1* gene, locus of *fsx1* is in red vertical line and pointed with a red arrowhead. **b** K-mer spectra deviation of *fsx1*-containing IMEs. K-mer spectrum deviation from centroid is shown for each of the Pure Culture Genomes (PCGs) where *fsx1* was detected. Blue region shows the standard deviation. Locus of *fsx1* is in red vertical line and pointed with a red arrowhead, the mobile element containing *fsx1* is in green. Dashed vertical white lines indicate the end of a contig in the genome assembly. *fsx1* is consistently found within regions that deviate from the core genome's spectrum, indicating they belong to a mobile element. Kbp, kilo base pairs.

This third scenario, an Archaeal origin of fusexins, poses new challenges to both sex origins and eukaryogenesis models. Discovery of the Asgard superphylum[55] and the recent cultivation of one of its members[56] support eukaryogenesis scenarios where populations of bacteria and archaea lived in syntrophy, transferring metabolites and genes[57]. Acquisition of a *fsx1* gene during the FECA to LECA transition could have enabled pre-LECA cells to undergo genome expansion, explore syncytial forms[58] and evolve into mononucleated cells fully equipped for meiosis and gamete fusion[59]. Our findings raise the possibility that gamete fusion is the product of over two billion years of evolution of this ancient archaeal cell fusion machine.

The archaeal proteins herein identified place fusexins in yet another domain of life, with different membrane chemistries and along a broad niche landscape, from cold hypersaline lakes to hot springs and hydrothermal vents (Fig. 6a). Our structural and functional analyses show that Fsx1 has both conserved and divergent properties when compared to eukaryotic and viral fusexins (Figs. 3 and 4). Like its viral counterparts, Fsx1 has an uncharged loop required for fusion. However, unlike previously known fusexins, Fsx1 harbors an additional domain (IV) involved in

fusogenic activity that may bind sugars (Figs. 2d and 3d). Considering that cell surface glycosylation was found to be important for fusion-based mating of halophilic archaea[60], this domain may actively promote fusion by interacting with carbohydrates attached to lipids or proteins such as S-layer glycoproteins[42]. Unlike HAP2s, Fsx1 homologs have 1–4 TMs and a variable Cys number (5–30, see Supplementary Data 1). Like eukaryotic fusexins, Fsx1 mediates BHK cell fusion in a bilateral fashion (Fig. 4f). However, in contrast to viral fusogens[36–38,61,62], the fusion activity of Fsx1 is maintained following substitution of its three TMs with a single TM or a GPI anchor. The retention of fusion activity when the transmembrane domains are replaced by a GPI anchor supports the model in which Fsx1 mediates homotypic fusion with fusogens required on both target membranes. These findings also suggest that interaction between the TMs during fusion is not essential for trimerization and expansion of the fusion pores. Since GPI-anchored AtHAP2 is also fusogenic, other fusexins may also drive complete cell fusion without a specific involvement of TMs. Future studies will address the function of the six-helix bundle formed by Fsx1 domain II, which is unprecedented among fusexins and raises an unexpected structural connection with class I viral fusogens[5,6].
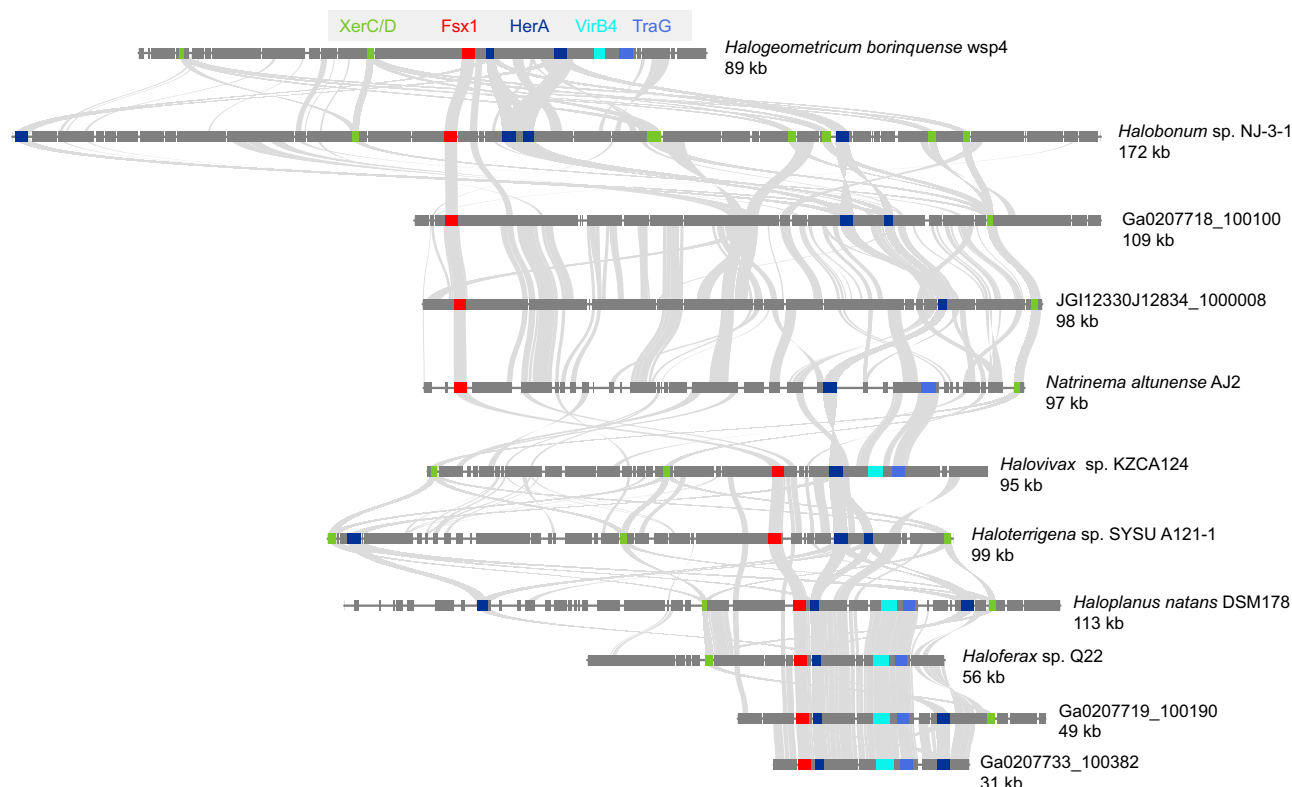
Fig. 8 Fsx1s are embedded in integrated mobile elements (IMEs). Synteny plots for IMEs from PCGs and metagenomic data. Annotated regions plus inferred ORFs belonging to homologous clusters identified by the workflow depicted in Supplementary Fig. 8. Homology relationships are represented by gray links. *fsx1* genes are marked in red and selected ORFs homologous to IME signature genes are labeled and color-coded. XerC/XerD recombinases (green); HerA helicase (dark blue); VirB4, Type IV secretion system (T4SS) pathway (cyan); TraG/TraD/VirD4 family enzyme, ATPase, T4SS (see Supplementary Table 3 and Supplementary Data 2, 3 for details). The 11 segments analyzed correspond to the cluster marked in Supplementary Fig. 9.

What are the limitations of this study? First, the description of the cellular and molecular functions of the *fsx1* family presented in this work is reliant upon expression within a heterologous system designed to probe fusion activity. Despite membrane chemistry differing from the type that would be associated with haloarchaeal hosts of the IME, Fsx1 was able to promote membrane fusion reliably. Second, evolutionary analysis and comparative genomics confirm *fsx1*'s link to IMEs. These sequences appear to be spread across a wide variety of niches all across the globe despite a relatively sparse distribution in sequenced archaeal genomes. Third, in this study we focused on describing the Fsx1 family evolutionarily, structurally and functionally to place it within its context in the Fusexin superfamily, but future studies will be needed to elucidate which biological processes *fsx1* is involved in as well as its relationship to the rest of the archaeal mobilome and virome. Additionally, structural features, such as the presence of a fourth domain, were modified in order to observe their effect on fusion activity within our experimental system, but it remains to be seen what importance they have in their native context. Future work will focus on studying *fsx1* in archaeal experimental systems as well as leverage metagenomic sampling and assembly techniques to exhaustively detect possible *fsx1* homologs in environments where it may be facilitating horizontal gene transfer.

Methods

Initial fusexin search using structurally guided MSAs. HMMs were prepared using structurally guided multiple sequence alignments (MSAs) of known eukaryotic HAP2 sequences (ectodomains only). Structural MSAs were derived using I-TASSER[68]-generated models of HAP2 homologs for *Erythranthe guttata* (A0A022QRC8), *Phytomonas* sp. isolate EM1 (W6KUI1), *Plasmodium falciparum* (A0A1C3KGX6), *Chlorella variabilis* (E1Z455) and the HAP2 crystal structures for

Chlamydomonas reinhardtii (PDB 6E18 [https://www.rcsb.org/structure/6E18][65], 6DBS [https://www.rcsb.org/structure/6DBS][26]) and *Arabidopsis thaliana* (PDB 5OW3 [https://www.rcsb.org/structure/5OW3][25]).

Searches for fusexin homologs using structurally guided MSAs were performed for 3 iterations on the Uniclust database[69] using default HHblits[70] parameters.

HMM-based distance matrices. A taxonomically representative list of known viral and eukaryotic fusexin homologs, covering major lineages, was manually curated. A MSA was built for each homolog by using the sequence as a query on the Uniclust database with HHblits for three iterations. This set of MSAs was compiled into an HH-suite database and each MSA was used as a query against this database to establish a profile-based distance matrix using the probability of homology (Fig. 1a and Supplementary Fig. 1).

Metaclust database search pipeline. We searched the Metaclust[71] dataset (nr50) using an HMM made of Fsx1 sequences found in PCGs and MAGs (Supplementary Data 1; see also codes, notebooks and datasets available at Zenodo[63]). Fsx1 sequences were aligned using ClustalO[72] with default settings for 3 iterations and the resulting MSA was used as a query with HMMER hmmsearch[73] against the Metaclust50 dataset[71]. All returned sequences with an *E*-value < 0.0001 with a match length greater than 100 residues were selected for further analysis. PSI-BLAST[74] was also used on the Metaclust (nr90) with Fsx1 sequences found in PCGs and MAGs with default parameters for 3 iterations. All returned sequences with an *E*-value < 0.0001 and an alignment length greater than 100 were added to the pool of candidates. Manual curation was performed using membrane protein topology predictor TOPCONS[75] and distant homology searches using HHblits[76] against PDB70.

DNA constructs. Ten archaeal genes were synthesized (GenScript) and cloned into pGene/V5-His vectors (Supplementary Table 5). Details of nucleotides used for synthesis and protein sequences are described in Supplementary Data 4.

For structural studies, a synthetic gene fragment encoding the extracellular region of a metagenomic Fsx1 ORF (IMG genome 3300000868, scaffold JGI12330J12834_ 1000008, ORF 8; Supplementary Data 1) (GenScript) was subcloned by PCR in frame with the 5′ chicken Crypα signal peptide- and 3′ 8xHis-tag-encoding sequences of pLJ6, a mammalian expression vector derived from
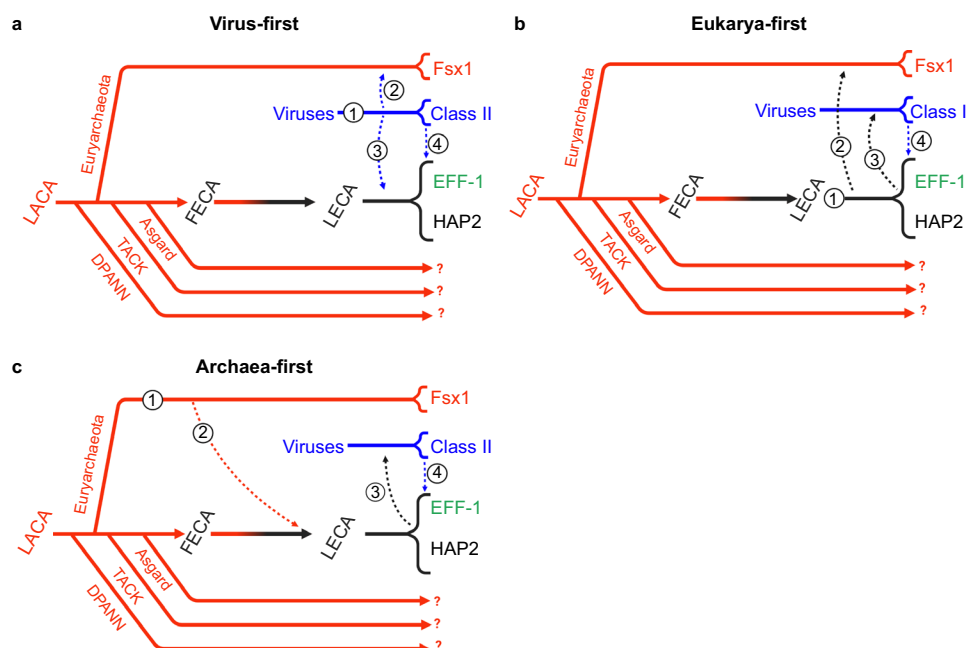
Fig. 9 Possible evolutionary trajectories. a Virus-first. Originating in the virosphere (1), ancestral fusexins were transferred to an ancient eukariotic organism (2) before the eukaryal radiation. Also before the eukaryal radiation, either viral (3) or early eukaryal (not numbered) fusexins were horizontally transferred to Archaea where they became integrated mobile elements. **b** Eukarya-first. Originating before the eukaryal radiation (1), fusexins were horizontally transferred to Archaea (2) where they became integrated in mobile elements. Eukaryal fusexins were captured by eukaryal viruses (3) leading to extant viral (class II) fusexins. **c** Archaea-first. Originating in Euryarchaeota (1), fusexins were horizontally transfered (2) and became fixed during eukaryogenesis and the emergence of meiotic sex. Viral capture of fusexin genes from early eukaryotic cells and further evolution within the virosphere led to extant viral (class II) fusexins (3). Common to all models, viral fusexin genes were captured by different eukaryotic lineages (4), leading to phlebovirus-like integrated fusogens and EFF-1 somatic fusogens[48,67]. Solid lines represent evolutionary trajectories of Archaea (red), viruses (blue), Eukarya (black), and eukaryogenesis (red to black gradient). Dashed arrows represent HGT events. Question marks denote uncertainty regarding the presence of *fsx1*-related genes in the respective lineages. LACA Last Archaeal Common Ancestor.

pHLsec3[77]. The protein construct that yielded the final high-resolution dataset included residues D25-S535 and contained a T369C substitution, introduced by PCR mutagenesis with the aim of facilitating heavy atom derivatization for experimental phasing. Oligonucleotides were from Sigma-Aldrich or IDT and all constructs were verified by DNA sequencing (Eurofins Genomics or Macrogen).

To generate pCI::GFPnes plasmid (see list of plasmids in Supplementary Table 6), an oligo DNA encoding for the nuclear export signal (LQKKLEELELD) was cloned downstream the region encoding EGFP of the pCAGIG plasmid using the enzyme BsrGI. Then, the GFPnes coding sequence was amplified, cut with BmgBI and BglII and used to replace the H2B-GFP coding sequence of the pCI::H2B-GFP plasmid (see list of primers in Supplementary Table 7). Fsx1-V5, AtHAP2-V5[22], EFF-1-V5, VSV-G[15] and other archaeal fusexins (NaFsx1, HQ22Fsx1, HnFsx1) were subcloned into corresponding pCI::H2B-RFP/H2B-GFP/GFPnes vectors separately. For mutagenesis of Fsx1, (i) Fsx1-ΔFL-AG₄A: The mutation of Y142A, Y149A and four glycines inserted between them were achieved using PCR with overlapping primers. (ii) Fsx1-ΔDIV-EFF-1 stem: The stem region of EFF-1 (E510-D561) was amplified from pGene::EFF-1-V5 and fused to the upstream and downstream regions of Fsx1-DIV with overlapping primers. (iii) Fsx1ΔTMs → EFF-1 TM: The TM and cytoplasmic tail of EFF-1 (I562–I658) were amplified from pGene::EFF-1-V5 and fused to the ectodomain of Fsx1 to replace its TMs. (iv) Fsx1ΔTMs→GPI: The Fsx1 TMs were replaced with the carboxy-terminal 37 amino acids of decay accelerating factor (DAF) which confer the signal for GPI anchor[78]. Similarly, the TM and cytoplasmic tail of AtHAP2 were replaced with the GPI signal from DAF to get AtHAP2ΔTM → GPI. All mutants were ligated into pCI::H2B-RFP and pCI::GFPnes vectors for mixing assay. Additional details are found in Supplementary Tables 6 and 7.

Protein expression and purification. HEK293T cells (ATCC CRL-3216)[79] were transiently transfected using 25 kDa branched polyethyleneimine and cultured in DMEM media (Invitrogen) supplemented with 2% (v/v) fetal bovine serum (Biological Industries). 90–96 h after transfection, the conditioned media from HEK293T cells was harvested, 0.2 μm-filtered (Pall) and adjusted to 20 mM Na–HEPES pH 7.8, 2.5 M NaCl, 5 mM imidazole. 10 ml Ni Sepharose excel beads (GE Healthcare) pre-equilibrated with immobilized metal affinity chromatography (IMAC) buffer (20 mM Na–HEPES pH 7.8, 2.5 M NaCl, 10 mM imidazole) were added to 1 l adjusted conditioned media and incubated overnight at 4 °C. After washing the beads with 100 column volumes IMAC buffer, captured Fsx1$_E$ was

batch-eluted with 30 mL 20 mM Na–HEPES pH 7.8, 2.5 M NaCl, 500 mM imidazole, and concentrated with 30 kDa-cutoff centrifugal filtration devices (Amicon). The material was then further purified by SEC at 4 °C, using an ÄKTAfplc chromatography system (GE Healthcare) equipped with a Superdex 200 Increase 10/300 GL column (GE Healthcare) pre-equilibrated with 20 mM Na-HEPES pH 7.8, 2.5 M NaCl. Peak fractions were pooled and concentrated to 5 mg mL^{-1} (Supplementary Fig. 2a, b).

Size-exclusion chromatography-multiangle light scattering (SEC-MALS). Purified Fsx1$_E$ samples (120–150 μg) were measured using an Ettan LC high-performance liquid chromatography system with a UV-900 detector (Amersham Pharmacia Biotech; λ = 280 nm), coupled with a miniDawn Treos MALS detector (Wyatt Technology; λ = 658 nm) and an Optilab T-rEX dRI detector (Wyatt Technology; λ = 660 nm). Separation was performed at 20 °C using a Superdex 200 Increase 10/300 GL column (GE Healthcare) with a flow rate of 0.5 mL min^{-1} and mobile phases consisting of 20 mM Tris–HCl pH 8.5, 150 mM NaCl (normal salt condition) or 20 mM Tris–HCl pH 8.5, 2.0 M NaCl and 0.2 M CaCl$_2$ (high salt condition) (Supplementary Fig. 2c). Data processing and weight-averaged molecular mass calculations were performed using ASTRA (Wyatt Technology). BSA (150 μg) was used as a control.

Small-angle X-ray scattering (SAXS). SAXS experiments were performed at beamline BM29 of the European Synchrotron Radiation Facility (ESRF)[80], using Fsx1$_E$ (4.5 mg mL^{-1}) in 20 mM Na-HEPES pH 7.8, 150 mM NaCl. Sample delivery and measurements were performed using a 1 mm-thick quartz capillary, which is part of the BM29 BioSAXS automated sample changer unit[81]. Data were collected at 1 Å wavelength in 10 frames of 1 s at 20 °C, using an estimated beam size of 1 mm × 100 μm; buffer blank measurements were carried out under the same conditions, both before and after sample measurement. Data were averaged and subtracted using PRIMUS[82] from the ATSAS package[83], which was also used to calculate the pair-distance distribution function, as well as the radius of gyration and the Porod volume. Theoretical scattering curves for monomeric and trimeric Fsx1$_E$ were calculated and compared with the experimental data using CRYSOL[84]. Ab initio envelope reconstruction was performed with DAMMIF[85], resulting in 20 models that were superimposed and averaged with DAMAVER[86]. Chain A of the refined Fsx1$_E$ model was either rigidly fitted with UCSF ChimeraX[87] into the

envelope generated by averaging all 20 independent ab initio SAXS models (Supplementary Fig. 2d, top envelope), or flexibly fit with Namdinator[88] into the average envelopes generated from the two most abundant clusters of SAXS models (accounting for 4 and 5 of the 20 SAXS models, respectively; Supplementary Fig. 2d, middle and bottom envelopes).

Crystallization and X-ray diffraction data collection. Two similar initial hits obtained from extensive screening using a mosquito crystallization robot (TTP Labtech) were manually optimized by setting up vapor diffusion experiments at 20 °C in 24-well plates. To grow diffraction-quality crystals, 1 μl purified $Fsx1_E$ was mixed with 1 μL 23% (w/v) PEG 4000, 0.1 M Tris–HCl pH 8.5, 0.2 M $CaCl_2$ and equilibrated against 1 mL of the same solution. Rhomboidal plates of $Fsx1_E$ grew in 1–3 months from protein precipitate that appeared after overnight equilibration of the crystallization drops (Supplementary Fig. 2e). For data collection, specimens were freed from the precipitate by micromanipulation with MicroMounts (MiTeGen) and flash frozen in liquid nitrogen. More than a hundred crystals were screened at beamlines ID23-1 of the ESRF[89] and I04 of Diamond Light Source, yielding datasets of highly variable quality. The final X-ray diffraction dataset at 2.3 Å resolution was collected at ESRF ID23-1.

Data reduction and non-crystallographic symmetry analysis. Datasets were processed in space group $C2$ with XDS[90] (Supplementary Table 2). By revealing a strong non-origin peak at chi = 120 (Supplementary Fig. 2f), self rotation functions calculated with MOLREP[91] or POLARRFN[92] clearly indicated the presence of three-fold non-crystallographic symmetry (NCS) within the asymmetric unit of the centered monoclinic crystals. Combined with Matthews coefficient calculations[93,94], this strongly suggested that $Fsx1_E$ crystallized as a homotrimer.

Structure determination by molecular replacement with AlphaFold2 models. Multiple attempts to experimentally determine the structure of $Fsx1_E$ using a variety of heavy atoms failed, probably because the high-salt mother liquor composition hindered heavy atom binding. Because molecular replacement (MR) with HAP2-derived homology models also failed, we phased the data by taking advantage of the recent significant advances in protein 3D structure prediction using machine learning[95] to phase the data by MR[96] (Supplementary Fig. 3). To do so, we used AlphaFold2[29] (with default monomer prediction parameters) to generate five independent models of Fsx1 ectodomain residues D25-S535, with per-residue pseudo-B factors corresponding to 100-(per-residue confidence (pLDDT[29])). These models had relative root-mean-square deviations (RMSD) of 1.4–3.3, or 0.7–1.9 Å after excluding 26 C-terminal residues predicted with low-confidence. Initial attempts to solve the structure by MR with Phaser[97], using an ensemble including these models (further truncated to Q453, the predicted C-terminal end of domain III), yielded 4 solutions (with top Log Likelihood Gain (LLG) 188, final translation function Z score (TFZ) 9.6) that were retrospectively correct in terms of domain I/II placement, but completely wrong in the positioning of domain III. Because of the latter, automatic refinement of these solutions did not progress beyond R_{free} ~ 0.53. On the other hand, a parallel consecutive search for three copies of a domain I/II ensemble (D25-A335; RMSD 0.3–0.9 Å) followed by three copies of domain III (P350-Q453; RMSD 0.1–0.3 Å), using a model RMSD variance of 1 Å, yielded a clear single solution (LLG 876, TFZ 23.1) that could be automatically refined to starting R 0.45, R_{free} 0.46.

Remarkably, although a single copy of domain 3 corresponds to only 7% of the total scattering mass in the asymmetric unit of the $Fsx1_E$ crystal, the very high accuracy of its AlphaFold2 model (reflected by *a posteriori*-calculated global RMSD and Distance Test Total Score (GDT_TS) of 0.7 Å and 97.6, respectively) allowed Phaser to also find a correct MR solution using just this part of the structure. Specifically, a consecutive search for three copies of the domain resulted in a trimeric model with LLG 275 and TFZ 15.1, which could be refined to starting R 0.51, R_{free} 0.51.

Also worth mentioning is the observation that the same domain I/II + domain III MR strategy used to phase the 2.3 Å resolution data could also be successfully applied to an initial dataset at much lower resolution (3.5 Å, with outer shell mean $I/\sigma I$ 0.6 and $CC_{1/2}$ 0.31); in this case, the Phaser LLG and TFZ values for the solution were 361 and 13.5, respectively, and initial automatic refinement of the corresponding model yielded R 0.44, R_{free} 0.48.

Model building, refinement, and validation. The initial model of $Fsx1_E$ was first automatically rebuilt using PHENIX AutoBuild[98] (1083 residues; R 0.34, R_{free} 0.38) and then significantly improved with the machine learning-based sequence-docking method of ARP/wARP[99], as implemented in CCP4[92] (1390 residues; REFMAC[100] R 0.23). The resulting set of coordinates was subsequently subjected to alternating cycles of manual rebuilding with Coot[101]/ISOLDE[102] and refinement with phenix.refine[103], using torsion-based NCS restraints and three Translation-Libration-Screw-rotation groups per chain. Putative identities of the metal ions were assigned based on electron density level; difference Fourier maps generated using alternative atom types; correspondence with peaks in phased anomalous difference maps, calculated with PHENIX[104] or ANODE[105] from data collected at low energy; and coordination properties[106]. Protein geometry was validated using MolProbity[107] (Supplementary Table 2).

Sequence-structure analysis. Sequence alignments were rendered with ESPript[108] and manually annotated. Transmembrane helices were predicted using TMHMM[109]. GDT_TS scores were calculated using LGA[110] and structural similarities were assessed with Dali[111] and PDBeFold[112]. Secondary structure was assigned using DSSP[113]. Subunit interfaces were analyzed using PDBsum[114], PIC[115] and PDBePISA[116]. Molecular charge was calculated using the YASARA2 force field of YASARA Structure[117] and electrostatic surface potential calculations were performed with PDB2PQR[118] and APBS[119], via the APBS Tools plugin of PyMOL (Schrödinger, LLC). Mapping of amino acid conservation onto the 3D structure of $Fsx1_E$ was carried out by analyzing a sequence alignment of archaeal homologs with ConSurf[120]. Structural figures were generated with PyMOL.

Structural modeling of trimeric Fsx1. Models of homotrimeric Fsx1 were generated using a local copy of AlphaFold-Multimer[121], installed using the open source code and instructions available at https://github.com/deepmind/alphafold.

Cells and reagents. Baby Hamster Kidney (BHK-21) cells (kindly obtained from Judith White, University of Virginia) were maintained in DMEM supplemented with 10% FBS (Biological Industries), 100 U/ml penicillin, 100 μg/ml streptomycin (Biological Industries), 2 mM L-glutamine (Biological Industries), 1 mM sodium pyruvate (Gibco), and 30 mM HEPES buffer, pH 7.3, at 37 °C with 5% CO_2. Transfections were performed using Fugene HD (Promega) or jetPRIME (Poly-plus) according to the manufacturer's instructions.

Immunofluorescence. BHK cells were grown on 24-well tissue-culture plates with glass coverslips. Permeabilized cells were fixed with 4% paraformaldehyde (EM grade, Bar Naor, Israel) in PBS, followed by incubation in 40 mM NH_4Cl to block free aldehydes, permeabilized in 0.1% Triton X-100 in PBS and blocked in 1% FBS in PBS. After fixation, the coverslips were incubated 1 h with mouse anti-V5 antibody (Invitrogen, 1:500) and 1 h with the secondary antibody which was donkey anti-mouse coupled to Alexa Fluor 488 (Invitrogen, 1:500). Alternatively, for immunofluorescence without permeabilization, cells were blocked on ice in PBS with 1% FBS for 20 min, and then stained with Monoclonal ANTI-FLAG M2 antibody (Sigma, 1:1000) on ice for 1 h. After anti-FLAG staining, cells were washed and fixed with 4% PFA in PBS. Cells were blocked again and stained with the secondary antibody (donkey anti-mouse coupled to Alexa Fluor 488; Invitrogen) diluted 1:500 in PBS for 1 h. In all cases, nuclei were stained with 1 μg/ml DAPI. Images were captured using a Nikon Eclipse E800 with a 60X/1.40 Plan Apochromat objective and an optical zoom lens (Nikon) using a Hamamatsu ORCA-ER camera controlled by Micro-Manager software[122] (Fig. 5f).

Western blots. 24 h post-transfection, cells were treated with lysis buffer (50 mM Tris–HCl pH 8.0, 100 mM NaCl, 5 mM EDTA, 1% Triton X-100 supplemented with chymostatin, leupeptin, antipain and pepstatin) on ice for 10 min. After centrifugation at $21,000 \times g$ for 10 min at 4 °C, supernatants of lysates were mixed with reducing sample buffer (+DTT) and incubated 5 min at 95 °C. Samples were loaded on a 10% SDS–PAGE gel and transferred to PVDF membrane. After blocking, membranes were incubated with primary antibody anti-V5 mouse monoclonal antibody (1:5000; Invitrogen) or anti-actin (1:2000; MP Biomedicals) at 4 °C overnight and HRP-conjugated goat anti-mouse secondary antibody 1 h at room temperature. Membranes were imaged by the ECL detection system using FUSION-PULSE.6 (VILBER).

Content mixing assays with immunofluorescence. BHK-21 cells at 70% confluence were transfected (using JetPrime; Polyplus at a ratio of 1:2 DNA:-transfection reagent) with 1 μg pCI::Fsx1-V5::H2B-eGFP, pCI::Fsx1-V5::H2B-RFP, pCI::AtHAP2-V5::H2B-eGFP, pCI::AtHAP2-V5::H2B-RFP, respectively. Control cells were co-transfected with pCI::H2B-eGFP and pRFPnes or pCI::H2B-RFP and pRFPnes. 4 h after transfection, the cells were washed 4 times with DMEM with 10% serum (Invitrogen), 4 times with PBS and detached using Trypsin (Biological Industries). The transfected cells were collected in Eppendorf tubes, resuspended in DMEM with 10% serum, and counted. Equal amounts of H2B-RFP and H2B-eGFP cells were mixed and seeded on glass-bottom plates (12-well black, glass-bottom #1.5H; Cellvis) and incubated at 37 °C and 5% CO_2. 18 h after mixing, 20 μM 5-fluoro-2'-deoxyuridine (FdUrd) was added to the plates to arrest the cell cycle and 24 h later, the cells were fixed with 4% PFA in PBS and processed for immuno-fluorescence. To assay mixed cells and detect the transfected proteins (Fsx1-V5 or AtHAP2-V5), we stained cells with anti-V5 mAb (Life Science). The secondary antibody was Alexa Fluor 488 goat anti-mouse, 1 μg/ml DAPI[22]. Micrographs were obtained using wide-field illumination using an ELYRA system S.1 microscope (Plan-Apochromat ×20 NA 0.8; Zeiss) and recorded with a iXon+ EMCCD camera (Andor). The GFP + RFP mixing index was calculated as the number of Red and Green nuclei in mixed cells out of the total number of nuclei of fluorescent cells in contact (Fig. 4b).

Cell fusion assay by content mixing with nuclear and cytoplasmic markers. For the unilateral setup, BHK-21 cells were transfected (as explained above) with 1 μg pCI::GFPnes; pCI::Fsx1-V5::GFPnes; 0.25 μg pCI::EFF-1-V5::GFPnes; 1 μg

pCI::VSV-G::GFPnes in respective 35 mm plates. The cells were incubated, washed, and mixed with pCI::H2B-RFP (empty vector) transfected cells (Fig. 4e). For evaluating the mutants, BHK-21 cells were transfected with 1 μg pCI::Fsx1-V5::GFPnes or pCI::Fsx1-V5::H2B-RFP or the plasmids encoding for each mutant: ΔFL → AG$_4$A, ΔDIV → EFF-1 stem, ΔTMs → EFF-1 TM, Fsx1ΔTMs → GPI, or AtHAP2ΔTM → GPI (Fig. 5a). Empty pCI::GFPnes or pCI::H2B-RFP were used as negative controls. 4 h after transfection, the cells were washed, counted, mixed, and incubated as previously described. In all cases, 18 h after mixing, 20 μM FdUrd was added to the plates, and 24 h later, the cells were fixed with 4% paraformaldehyde diluted in PBS. Nuclei were stained with 1 μg/ml DAPI. Images were obtained using wide-field illumination with an ELYRA system S.1 microscope as described above.

The GFP + RFP mixing index was calculated as the number of nuclei in mixed cells, green cytoplasm (GFPnes) with red (H2B-RFP) and blue (DAPI) nuclei out of the total number of nuclei in fluorescent cells in contact (Figs. 4f, 5b). The multinucleation indexes were defined as the ratio between the number of nuclei in multinucleated cells (N_m) and the total number of nuclei in multinucleated cells and expressing cells that were in contact (N_c) but did not fuse, using the following equation: % multinucleation = $N_m/(N_c + N_m) \times 100$. The percentage of multinucleation was calculated for GFPnes cells with RFP and DAPI nuclei. For the unilateral assay, multinucleation was determined as the ratio between the number of nuclei in multinucleated green cells and the total number of nuclei in green multinucleated cells and GFPnes expressing cells that were in contact but did not fuse (Fig. 4f).

Live imaging of fusing cells. BHK cells were plated on 15 mm glass bottom plates (Wuxi NEST Biotechnology Co., Ltd.) and transfected with 1 μg pCI::Fsx1-V5::H2B-GFP together with 0.5 μg myristoylated-mCherry (myr-palm-mCherry; kindly provided by Valentin Dunsing and Salvatore Chiantia[123]). 18 h after transfection, the cells were incubated with 2 μg/ml Hoechst dye for 10 min at 37 °C and washed once with fresh medium. Time-lapse microscopy to identify fusing cells was performed using a spinning disc confocal microscope (CSU-X; Yokogawa Electric Corporation) with an Eclipse Ti and a Plan-Apochromat ×20 (NA, 0.75; Nikon) objective. Images in differential interference contrast and red channels were recorded every 4 min in different positions of the plate using high gain and minimum laser exposure. Time lapse images were captured with an iXon 3 EMCCD camera (Andor Technology). After 5 h, confocal z-series, including detection of the DAPI channel, were obtained to confirm the formation of multinucleated cells. Image analyses were performed in MetaMorph (Molecular Devices) and ImageJ[124] (National Institutes of Health).

Surface biotinylation. Proteins localizing on the surface were detected as previously described[22]. Briefly, BHK cells were transfected with 1 μg pCAGGS, pCAGGS::EFF-1-V5, pCAGGS::Fsx1-V5, pCAGGS::ΔFL → AG$_4$A-V5, pCAGGS::ΔDIV → EFF-1 stem-V5 or pCAGGS::Fsx1ΔTMs → EFF-1 TM-V5. 24 h later, cells were washed twice with ice-cold PBS^{2+} (with Ca^{2+} and Mg^{2+}) and incubated with 0.5 mg/ml EZ-Link Sulfo NHS-Biotin (Thermo Fisher Scientific) for 30 min on ice. The cells were washed four times with ice-cold PBS^{2+}, once with DMEM with 10% FBS (to quench residual biotin), followed by two more washes with PBS^{2+}. To each plate 300 μl of lysis buffer supplemented with 10 mM iodoacetamide were added and the cells detached using a scrapper. The insoluble debris was separated by centrifugation (10 min at 21,000 × g), and the lysate was mixed with NeutrAvidin Agarose Resin (Thermo Fisher Scientific) and 0.3% SDS. After an incubation of 12 h at 4 °C the resin was separated by centrifugation (2 min at 21,000 × g), washed three times with lysis buffer and then mixed with SDS–PAGE loading solution with freshly added 5% β-mercaptoethanol and incubated 5 min at 100 °C. After pelleting by centrifugation, the samples were separated by SDS–PAGE gel and analyzed by Western blotting as described above using anti-V5 mouse monoclonal antibody. Loading was controlled using anti-actin C4 monoclonal (1:2000; MP Biomedicals).

Integrated mobile element (IME) identification by k-mer spectra analysis and comparative genomics. Comparison between close species with presence (fsx1+) or absence (fsx1−) of archaeal fusexins to detect insertion sites was done performing sequence similarity searches in complete genomes from the closest relatives available in the PATRIC database[125] (Fig. 7a and Supplementary Table 4). Coordinates of fsx1-containing IMEs present in PCGs are annotated in Supplementary Table 4.

Among different methodologies that rely on DNA composition to identify horizontally transferred genomic regions[126], k-mer spectrum analysis is a standard tool for this purpose[127,128]. Normalized k-mer spectra for DNA sequences of arbitrary length were generated by counting occurrences of all k-mers and normalizing by the total amount of words counted. k-mer sizes from 3 to 8 bp were tested with no effect on results. A length of 4 bp was selected. To detect possible horizontally transferred regions, an average spectrum for each genome was calculated. A spectrum was calculated for a sliding window of 1 kb using 500 bp steps and subtracted from the genomic average at each window position (Fig. 7b). The absolute value of the difference between the genomic average and window spectra is represented over the entire genome. Gaussian mixture models using two distributions were fitted[129] to the k-mer content of all windows, to classify these as

belonging to either the core genome or transferred elements. This deviation in k-mer spectra has been explored in the context of the archaeal mobilome and contains information on the ecological niche and evolutionary history of DNA sequences[130].

IME gene content and homology analyses. We followed the pipeline depicted in Supplementary Fig. 8. Briefly, PCGs' IMEs were determined by a combination of k-mer spectra and genomic alignments (see Supplementary Table 4). We initially inspected fsx1-containing scaffolds and kept only sequences that were 20 kb or longer for downstream analyses. We generated an enriched annotation for each IME. Then, we obtained an initial set of groups of homologous sequences, and each of these groups was enriched by means of HMM searches. Subsequently, the enriched homology groups showing similarity between them, as judged by HMM–HMM comparisons, were collapsed into unique groups.

In detail, first, we re-annotated the identified mobile elements combining the corresponding segment of the PATRIC[125] GFF annotation file with in-house ORF predictions (minimum ORF length of 30 nucleotides, option by default). ORF inference was done by means of getorf of the EMBOSS package[131], specifying genetic code by Table 11 (Bacteria and Archaea) and other parameters running by default. The similarity of inferred ORFs and annotated features in these mobile elements (i.e., features in their GFF annotation file) was established by means of BLASTP reciprocal searches[74]. We kept all the predicted ORFs and homologs that were at least annotated in one genome, in this way we tried to recover missanotated conserved ORFs.

Initial sets of homologs were generated with get_homologs[132]. Sequence identity and query coverage thresholds were set to 35% and 70%, respectively. In-paralogues were not allowed within these groups (option '-e'), and remaining parameters were run by default.

HMM profiles were constructed for each homolog group. To this aim, homologous sequences were retrieved for members of each group from the UniRef50 database[133] with jackhmmer from the HMMER package[73] running with one iteration ('-N 1' parameter). MSAs were then generated for each group and its relevant hits with MAFFT[134] running under '-auto' parameter, and HMMs were created with HMMER hmmbuild. Homolog groups were enriched by means of HMM searches with HMMER hmmsearch, using each HMM as a query against a database comprising all predicted ORFs described above. Hits showing an e-value < 1e−10 and covering at least 50% of the HMM were added to the groups.

Enriched homology groups showing homology were collapsed. For this purpose, HMM-vs.-HMM comparisons were performed with HHalign from the HHsuite[135]. A graph was created with the networkx Python library (https://networkx.org), each node being an enriched group of homologs. An edge was established between nodes if their HMM-HMM alignment was significant (i.e., e-value < 1e−10, HMM coverage of longest HMM > = 50%). Groups of interconnected nodes were established with the 'connected_components()' routine, creating a collapsed homology group in each case.

Finally, we assessed the gene content similarity between mobile elements using a Jaccard Index based on the homology groups defined above. Usual Jaccard index of two sets is defined as (# of the intersection)/(# of the union). In this case:

$$J(\text{MEA, MEB}) = \frac{N\text{homology groups shared between ME A\&ME B}}{N\text{homol.groups MEA} + N\text{homol.groups MEB} − N\text{homol.groups shared between ME A\&ME B}}$$

We performed a hierarchical clustering of the MEs based on a distance matrix obtained from the pairwise Jaccard Indexes (distance(A,B) = $1 − J_{A,B}$). This was done in Python with seaborn[136], employing the clustermap function. A subset of 11 mobile elements (red cluster in Supplementary Fig. 9), which included ME from PCGs and JGI12330J12834-1000008 (Supplementary Data 1, 3 and 4), was selected for synteny conservation analysis. Plots depicting synteny in gene content between homolog groups were generated employing the MCscan tool[137].

HMMER and Pfam[138] were used on default parameters to assign domains and their associated arCOG[139,140] identifiers to ORFs (Supplementary Data 2).

These analyses, including collapsed clusters, can be found in Zenodo[63].

Sequence and structure phylogenies. Maximum-likelihood phylogenetic trees were generated with sequences aligned with MAFFT (L-INS-i option) as input for IQ-TREE2[141] and selecting the best evolutionary model with ModelFinder[142]. Homology trimeric models of archaeal homologs of Fsx1$_E$ were built with MODELLER using our crystal structure as template.

Protein folds preserve deeper evolutionary signals than sequences[143–145]. Fsx1 models and crystal structures of Fsx1$_E$ and eukaryotic and viral fusexins were all-vs.-all compared with FATCAT[146] to establish their structural distances between them. The following experimental crystal structures from other works were used: Flavivirus E: West Nile virus (2I69)[147]; Dengue virus serotype 1 (4GSX)[148]; Alphavirus E1: Semliki Forest virus (1RER)[149]; Chikungunya (3N43)[150]; C. elegans EFF-1 (4OJC)[16]; Bunyavirus Gc Rift Valley fever virus (6EGU)[151]; eukaryotic HAP2/GCS1 from A. thaliana (5OW3)[25] and C. reinhardtii (6E18)[65]. The PDB files produced by flexible alignment with FATCAT were compared with TMalign[152] to build a TM$_{score}$[153] distance matrix (distance = $1−$TM$_{score}$). This distance matrix was the basis to compute a minimum evolution tree with FastME[154] on default parameters (Supplementary Fig. 10b).

Data availability

Crystallographic structure factors and atomic coordinates have been deposited in the Protein Data Bank under accession code 7P4L.

Source Data for this paper's structure-function analyses (Figs. 4 and 5, and Supplementary Fig. 1) are provided in the Source Data file; sequences of synthesized *fsx1* genes are in Supplementary Data 4. Source data are provided with this paper.

Code availability

All relevant codes, notebooks and datasets necessary for: HHblits and HMMER searches and comparisons (Fig. 1a, Supplementary Fig. 1a); genomic comparisons and K-mer spectra analyses (Fig. 7); bioinformatic workflow for IMEs, IMEs clustering, content and synteny analyses (Supplementary Figs. 8 and 9, Fig. 8 and Supplementary Data 2 and 3); and structure- and sequence-based comparisons (Supplementary Fig. 10 and Supplementary Data 5), are provided on GitHub (https://github.com/DessimozLab/Archaeal-Fusexins) and Zenodo (https://doi.org/10.5281/zenodo.6677729)[63].

References

1. Speijer, D., Lukeš, J. & Eliáš, M. Sex is a ubiquitous, ancient, and inherent attribute of eukaryotic life. *Proc. Natl Acad. Sci. USA* **112**, 8827–8834 (2015).
2. Ramesh, M. A., Malik, S.-B. & Logsdon, J. M. Jr. A phylogenomic inventory of meiotic genes; evidence for sex in Giardia and an early eukaryotic origin of meiosis. *Curr. Biol.* **15**, 185–191 (2005).
3. Podbilewicz, B. Virus and cell fusion mechanisms. *Annu. Rev. Cell Dev. Biol.* **30**, 111–139 (2014).
4. White, J. M., Delos, S. E., Brecher, M. & Schornberg, K. Structures and mechanisms of viral membrane fusion proteins: multiple variations on a common theme. *Crit. Rev. Biochem. Mol. Biol.* **43**, 189–219 (2008).
5. Kielian, M. Mechanisms of virus membrane fusion proteins. *Annu. Rev. Virol.* **1**, 171–189 (2014).
6. Harrison, S. C. Viral membrane fusion. *Virology* **479–480**, 498–507 (2015).
7. Millay, D. P. et al. Myomaker is a membrane activator of myoblast fusion and muscle formation. *Nature* **499**, 301–305 (2013).
8. Leikina, E. et al. Myomaker and myomerger work independently to control distinct steps of membrane remodeling during myoblast fusion. *Dev. Cell* **46**, 767–780.e7 (2018).
9. Brukman, N. G., Li, X. & Podbilewicz, B. Fusexins, HAP2/GCS1 and evolution of gamete fusion. *Front. Cell Dev. Biol.* **9**, 824024 (2021).
10. Mohler, W. A. et al. The type I membrane protein EFF-1 is essential for developmental cell fusion. *Dev. Cell* **2**, 355–362 (2002).
11. Iosilevskii, Y. & Podbilewicz, B. Programmed cell fusion in development and homeostasis. *Curr. Top. Dev. Biol.* **144**, 215–244 (2021).
12. Avinoam, O. Conserved eukaryotic fusogens can fuse viral envelopes to cells. Ph.D. thesis, Technion-Israel Institute of Technology (2012).
13. Podbilewicz, B. et al. The *C. elegans* developmental fusogen EFF-1 mediates homotypic fusion in heterologous cells and in vivo. *Dev. Cell* **11**, 471–481 (2006).
14. Sapir, A. et al. AFF-1, a FOS-1-regulated fusogen, mediates fusion of the anchor cell in *C. elegans*. *Dev. Cell* **12**, 683–698 (2007).
15. Avinoam, O. et al. Conserved eukaryotic fusogens can fuse viral envelopes to cells. *Science* **332**, 589–592 (2011).
16. Pérez-Vargas, J. et al. Structural basis of eukaryotic cell–cell fusion. *Cell* **157**, 407–419 (2014).
17. Johnson, M. A. et al. Arabidopsis hapless mutations define essential gametophytic functions. *Genetics* **168**, 971–982 (2004).
18. Mori, T., Kuroiwa, H., Higashiyama, T. & Kuroiwa, T. GENERATIVE CELL SPECIFIC 1 is essential for angiosperm fertilization. *Nat. Cell Biol.* **8**, 64–71 (2006).
19. Liu, Y. et al. The conserved plant sterility gene HAP2 functions after attachment of fusogenic membranes in *Chlamydomonas* and *Plasmodium* gametes. *Genes Dev.* **22**, 1051–1068 (2008).
20. Cole, E. S. et al. Function of the male-gamete-specific fusion protein HAP2 in a seven-sexed ciliate. *Curr. Biol.* **24**, 2168–2173 (2014).
21. Okamoto, M. et al. Two HAP2-GCS1 homologs responsible for gamete interactions in the cellular slime mold with multiple mating types: Implication for common mechanisms of sexual reproduction shared by plants and protozoa and for male-female differentiation. *Dev. Biol.* **415**, 6–13 (2016).
22. Valansi, C. et al. Arabidopsis HAP2/GCS1 is a gamete fusion protein homologous to somatic and viral fusogens. *J. Cell Biol.* **216**, 571–581 (2017).
23. Fédry, J. et al. The ancient gamete fusogen HAP2 is a Eukaryotic Class II fusion protein. *Cell* **168**, 904–915.e10 (2017).
24. Pinello, J. F. et al. Structure–function studies link Class II viral fusogens with the ancestral gamete fusion protein HAP2. *Curr. Biol.* **27**, 651–660 (2017).
25. Fedry, J. et al. Evolutionary diversification of the HAP2 membrane insertion motifs to drive gamete fusion across eukaryotes. *PLoS Biol.* **16**, e2006357 (2018).
26. Feng, J. et al. Fusion surface structure, function, and dynamics of gamete fusogen HAP2. *Elife* **7**, e39772 (2018).
27. Wong, J. L. & Johnson, M. A. Is HAP2-GCS1 an ancestral gamete fusogen? *Trends Cell Biol.* **20**, 134–141 (2010).
28. Doms, R. W. What came first-the virus or the egg? *Cell* **168**, 755–757 (2017).
29. Jumper, J. et al. Highly accurate protein structure prediction with AlphaFold. *Nature* **596**, 583–589 (2021).
30. Modis, Y., Ogata, S., Clements, D. & Harrison, S. C. Structure of the dengue virus envelope protein after membrane fusion. *Nature* **427**, 313–319 (2004).
31. Mueller, G. A. et al. Serological, genomic and structural analyses of the major mite allergen Der p 23. *Clin. Exp. Allergy* **46**, 365–376 (2016).
32. Tunyasuvunakool, K. et al. Highly accurate protein structure prediction for the human proteome. *Nature* **596**, 590–596 (2021).
33. DuBois, R. M. et al. Functional and evolutionary insight from the crystal structure of rubella virus protein E1. *Nature* **493**, 552–556 (2013).
34. Dubé, M., Etienne, L., Fels, M. & Kielian, M. Calcium-dependent Rubella virus fusion occurs in early endosomes. *J. Virol.* **90**, 6303–6313 (2016).
35. Gattegno, T. et al. Genetic control of fusion pore expansion in the epidermis of *Caenorhabditis elegans*. *Mol. Biol. Cell* **18**, 1153–1166 (2007).
36. Kemble, G. W., Danieli, T. & White, J. M. Lipid-anchored influenza hemagglutinin promotes hemifusion, not complete fusion. *Cell* **76**, 383–391 (1994).
37. Markosyan, R. M., Cohen, F. S. & Melikyan, G. B. The lipid-anchored ectodomain of influenza virus hemagglutinin (GPI-HA) is capable of inducing nonenlarging fusion pores. *Mol. Biol. Cell* **11**, 1143–1152 (2000).
38. Jones, N. A. & Geraghty, R. J. Fusion activity of lipid-anchored envelope glycoproteins of herpes simplex virus type 1. *Virology* **324**, 213–228 (2004).
39. Ludt, K. & Soppa, J. Polyploidy in halophilic archaea: regulation, evolutionary advantages, and gene conversion. *Biochem. Soc. Trans.* **47**, 933–944 (2019).
40. Turgeman-Grott, I. et al. Pervasive acquisition of CRISPR memory driven by inter-species mating of archaea can limit gene transfer and influence speciation. *Nat. Microbiol.* **4**, 177–186 (2019).
41. DeMaere, M. Z. et al. High level of intergenera gene exchange shapes the evolution of haloarchaea in an isolated Antarctic lake. *Proc. Natl Acad. Sci. USA* **110**, 16939–16944 (2013).
42. Sivabalasarma, S. et al. Analysis of cell–cell bridges in *Haloferax volcanii* using electron cryo-tomography reveal a continuous cytoplasm and S-layer. *Front. Microbiol.* **11**, 612239 (2020).
43. Rosenshine, I., Tchelet, R. & Mevarech, M. The mechanism of DNA transfer in the mating system of an archaebacterium. *Science* **245**, 1387–1389 (1989).
44. Naor, A., Lapierre, P., Mevarech, M., Papke, R. T. & Gophna, U. Low species barriers in halophilic archaea and the formation of recombinant hybrids. *Curr. Biol.* **22**, 1444–1448 (2012).
45. Wagner, A. et al. Mechanisms of gene flow in archaea. *Nat. Rev. Microbiol.* **15**, 492–501 (2017).
46. Koonin, E. V. & Krupovic, M. The depths of virus exaptation. *Curr. Opin. Virol.* **31**, 1–8 (2018).
47. Modis, Y. Relating structure to evolution in class II viral membrane fusion proteins. *Curr. Opin. Virol.* **5**, 34–41 (2014).
48. Merchant, M. et al. A bioactive phlebovirus-like envelope protein in a hookworm endogenous virus. *Sci. Adv.* **8**, eabj6894 (2022).
49. Krupovic, M. & Koonin, E. V. Multiple origins of viral capsid proteins from cellular ancestors. *Proc. Natl Acad. Sci. USA* **114**, E2401–E2410 (2017).
50. El Omari, K. et al. The structure of a prokaryotic viral envelope protein expands the landscape of membrane fusion proteins. *Nat. Commun.* **10**, 846 (2019).
51. Brochier-Armanet, C. et al. Complete-fosmid and fosmid-end sequences reveal frequent horizontal gene transfers in marine uncultured planktonic archaea. *ISME J.* **5**, 1291–1302 (2011).
52. Gabaldón, T. Origin and early evolution of the Eukaryotic cell. *Annu. Rev. Microbiol.* **75**, 631–647 (2021).
53. Liu, Y. et al. Expanded diversity of Asgard archaea and their relationships with eukaryotes. *Nature* **593**, 553–557 (2021).
54. Vosseberg, J. et al. Timing the origin of eukaryotic cellular complexity with ancient duplications. *Nat. Ecol. Evol.* **5**, 92–100 (2021).
55. Zaremba-Niedzwiedzka, K. et al. Asgard archaea illuminate the origin of eukaryotic cellular complexity. *Nature* **541**, 353–358 (2017).

56. Imachi, H. et al. Isolation of an archaeon at the prokaryote–eukaryote interface. *Nature* **577**, 519–525 (2020).

57. O'Malley, M. A., Leger, M. M., Wideman, J. G. & Ruiz-Trillo, I. Concepts of the last eukaryotic common ancestor. *Nat. Ecol. Evol.* **3**, 338–344 (2019).

58. Skejo, J. et al. Evidence for a syncytial origin of Eukaryotes from ancestral state reconstruction. *Genome Biol. Evol.* **13**, evab096 (2021).

59. Koonin, E. V. Origin of eukaryotes from within archaea, archaeal eukaryome and bursts of gene gain: eukaryogenesis just made easier? *Philos. Trans. R. Soc. Lond. B Biol. Sci.* **370**, 20140333 (2015).

60. Shalev, Y., Turgeman-Grott, I., Tamir, A., Eichler, J. & Gophna, U. Cell surface glycosylation is required for efficient mating of *Haloferax volcanii*. *Front. Microbiol.* **8**, 1253 (2017).

61. Odell, D., Wanas, E., Yan, J. & Ghosh, H. P. Influence of membrane anchoring and cytoplasmic domains on the fusogenic activity of vesicular stomatitis virus glycoprotein G. *J. Virol.* **71**, 7996–8000 (1997).

62. Tong, S. & Compans, R. W. Oligomerization, secretion, and biological function of an anchor-free parainfluenza virus type 2 (PI2) fusion protein. *Virology* **270**, 368–376 (2000).

63. Moi, D., Langleib, M., Graña, M. & Romero, H. Discovery of archaeal fusexins homologous to eukaryotic HAP2/GCS1 gamete fusion proteins. github.com/DessimozLab/Archaeal-Fusexins https://doi.org/10.5281/zenodo.6677729 (2022).

64. Liu, Y., Pei, J., Grishin, N. & Snell, W. J. The cytoplasmic domain of the gamete membrane fusion protein HAP2 targets the protein to the fusion site in *Chlamydomonas* and regulates the fusion reaction. *Development* **142**, 962–971 (2015).

65. Baquero, E., Fedry, J., Legrand, P., Krey, T. & Rey, F. A. Species-specific functional regions of the green alga gamete fusion protein HAP2 revealed by structural studies. *Structure* **27**, 113–124.e4 (2019).

66. Sali, A. & Blundell, T. L. Comparative protein modelling by satisfaction of spatial restraints. *J. Mol. Biol.* **234**, 779–815 (1993).

67. Malik, H. S., Henikoff, S. & Eickbush, T. H. Poised for contagion: evolutionary origins of the infectious abilities of invertebrate retroviruses. *Genome Res.* **10**, 1307–1318 (2000).

68. Yang, J. et al. The I-TASSER Suite: protein structure and function prediction. *Nat. Methods* **12**, 7–8 (2015).

69. Mirdita, M. et al. Uniclust databases of clustered and deeply annotated protein sequences and alignments. *Nucleic Acids Res.* **45**, D170–D176 (2017).

70. Remmert, M., Biegert, A., Hauser, A. & Söding, J. HHblits: lightning-fast iterative protein sequence searching by HMM–HMM alignment. *Nat. Methods* **9**, 173–175 (2011).

71. Steinegger, M. & Söding, J. Clustering huge protein sequence sets in linear time. *Nat. Commun.* **9**, 2542 (2018).

72. Sievers, F. & Higgins, D. G. Clustal Omega, accurate alignment of very large numbers of sequences. *Methods Mol. Biol.* **1079**, 105–116 (2014).

73. Eddy, S. R. Accelerated profile HMM searches. *PLoS Comput. Biol.* **7**, e1002195 (2011).

74. Altschul, S. F. et al. Gapped BLAST and PSI-BLAST: a new generation of protein database search programs. *Nucleic Acids Res.* **25**, 3389–3402 (1997).

75. Tsirigos, K. D., Peters, C., Shu, N., Kall, L. & Elofsson, A. The TOPCONS web server for consensus prediction of membrane protein topology and signal peptides. *Nucleic Acids Res.* **43**, W401–W407 (2015).

76. Söding, J. Protein homology detection by HMM–HMM comparison. *Bioinformatics* **21**, 951–960 (2005).

77. Raj, I. et al. Structural basis of egg coat–sperm recognition at fertilization. *Cell* **169**, 1315–1326.e17 (2017).

78. Kemble, G. W., Henis, Y. I. & White, J. M. GPI- and transmembrane-anchored influenza hemagglutinin differ in structure and receptor binding activity. *J. Cell Biol.* **122**, 1253–1265 (1993).

79. DuBridge, R. B. et al. Analysis of mutation in human cells by using an Epstein-Barr virus shuttle system. *Mol. Cell. Biol.* **7**, 379–387 (1987).

80. Pernot, P. et al. Upgraded ESRF BM29 beamline for SAXS on macromolecules in solution. *J. Synchrotron Radiat.* **20**, 660–664 (2013).

81. Round, A. et al. BioSAXS Sample Changer: a robotic sample changer for rapid and reliable high-throughput X-ray solution scattering experiments. *Acta Crystallogr. D Biol. Crystallogr.* **71**, 67–75 (2015).

82. Konarev, P. V., Volkov, V. V., Sokolova, A. V., Koch, M. H. J. & Svergun, D. I. PRIMUS: a Windows PC-based system for small-angle scattering data analysis. *J. Appl. Crystallogr.* **36**, 1277–1282 (2003).

83. Manalastas-Cantos, K. et al. ATSAS 3.0: expanded functionality and new tools for small-angle scattering data analysis. *J. Appl. Crystallogr.* **54**, 343–355 (2021).

84. Svergun, D., Barberato, C. & Koch, M. H. J. CRYSOL—a program to evaluate X-ray solution scattering of biological macromolecules from atomic coordinates. *J. Appl. Crystallogr.* **28**, 768–773 (1995).

85. Franke, D. & Svergun, D. I. DAMMIF, a program for rapid ab-initio shape determination in small-angle scattering. *J. Appl. Crystallogr.* **42**, 342–346 (2009).

86. Volkov, V. V. & Svergun, D. I., IUCr. Uniqueness of ab initio shape determination in small-angle scattering. *J. Appl. Crystallogr.* **36**, 860–864 (2003).

87. Pettersen, E. F. et al. UCSF ChimeraX: structure visualization for researchers, educators, and developers. *Protein Sci.* **30**, 70–82 (2021).

88. Kidmose, R. T. et al. Namdinator—automatic molecular dynamics flexible fitting of structural models into cryo-EM and crystallography experimental maps. *IUCrJ* **6**, 526–531 (2019).

89. Nurizzo, D. et al. The ID23-1 structural biology beamline at the ESRF. *J. Synchrotron Radiat.* **13**, 227–238 (2006).

90. Kabsch, W. XDS. *Acta Crystallogr. D. Biol. Crystallogr.* **66**, 125–132 (2010).

91. Vagin, A. & Teplyakov, A. MOLREP: an automated program for molecular replacement. *J. Appl. Crystallogr.* **30**, 1022–1025 (1997).

92. Winn, M. D. et al. Overview of the CCP4 suite and current developments. *Acta Crystallogr. D Biol. Crystallogr.* **67**, 235–242 (2011).

93. Matthews, B. W. Solvent content of protein crystals. *J. Mol. Biol.* **33**, 491–497 (1968).

94. Kantardjieff, K. A. & Rupp, B. Matthews coefficient probabilities: improved estimates for unit cell contents of proteins, DNA, and protein–nucleic acid complex crystals. *Protein Sci.* **12**, 1865–1871 (2003).

95. AlQuraishi, M. Machine learning in protein structure prediction. *Curr. Opin. Chem. Biol.* **65**, 1–8 (2021).

96. Millán, C. et al. Assessing the utility of CASP14 models for molecular replacement. *Proteins* **89**, 1752–1769 (2021).

97. McCoy, A. J. et al. Phaser crystallographic software. *J. Appl. Crystallogr.* **40**, 658–674 (2007).

98. Terwilliger, T. C. et al. Iterative model building, structure refinement and density modification with the PHENIX AutoBuild wizard. *Acta Crystallogr. D Biol. Crystallogr.* **64**, 61–69 (2008).

99. Chojnowski, G., Pereira, J. & Lamzin, V. S. Sequence assignment for low-resolution modelling of protein crystal structures. *Acta Crystallogr. D Struct. Biol.* **75**, 753–763 (2019).

100. Murshudov, G. N. et al. REFMAC5 for the refinement of macromolecular crystal structures. *Acta Crystallogr. D Biol. Crystallogr.* **67**, 355–367 (2011).

101. Casañal, A., Lohkamp, B. & Emsley, P. Current developments in Coot for macromolecular model building of Electron Cryo-microscopy and Crystallographic Data. *Protein Sci.* **29**, 1069–1078 (2020).

102. Croll, T. I. ISOLDE: a physically realistic environment for model building into low-resolution electron-density maps. *Acta Crystallogr. D Struct. Biol.* **74**, 519–530 (2018).

103. Afonine, P. V. et al. Towards automated crystallographic structure refinement with phenix.refine. *Acta Crystallogr. D Biol. Crystallogr.* **68**, 352–367 (2012).

104. Liebschner, D. et al. Macromolecular structure determination using X-rays, neutrons and electrons: recent developments in *Phenix. Acta Crystallogr. D Struct. Biol.* **75**, 861–877 (2019).

105. Thorn, A. & Sheldrick, G. M. ANODE: anomalous and heavy-atom density calculation. *J. Appl. Crystallogr.* **44**, 1285–1287 (2011).

106. Zheng, H. et al. *CheckMyMetal*: a macromolecular metal-binding validation tool. *Acta Crystallogr. D Biol. Crystallogr.* **73**, 223–233 (2017).

107. Williams, C. J. et al. MolProbity: more and better reference data for improved all-atom structure validation. *Protein Sci.* **27**, 293–315 (2018).

108. Gouet, P., Robert, X. & Courcelle, E. ESPript/ENDscript: extracting and rendering sequence and 3D information from atomic structures of proteins. *Nucleic Acids Res.* **31**, 3320–3323 (2003).

109. Sonnhammer, E. L., von Heijne, G. & Krogh, A. A hidden Markov model for predicting transmembrane helices in protein sequences. *Proc. Int. Conf. Intell. Syst. Mol. Biol.* **6**, 175–182 (1998).

110. Zemla, A. LGA: a method for finding 3D similarities in protein structures. *Nucleic Acids Res.* **31**, 3370–3374 (2003).

111. Holm, L. Using Dali for protein structure comparison. *Methods Mol. Biol.* **2112**, 29–42 (2020).

112. Krissinel, E. & Henrick, K. Secondary-structure matching (SSM), a new tool for fast protein structure alignment in three dimensions. *Acta Crystallogr. D Biol. Crystallogr.* **60**, 2256–2268 (2004).

113. Kabsch, W. & Sander, C. Dictionary of protein secondary structure: pattern recognition of hydrogen-bonded and geometrical features. *Biopolymers* **22**, 2577–2637 (1983).

114. de Beer, T. A. P., Berka, K., Thornton, J. M. & Laskowski, R. A. PDBsum additions. *Nucleic Acids Res.* **42**, D292–D296 (2014).

115. Tina, K. G., Bhadra, R. & Srinivasan, N. PIC: Protein Interactions Calculator. *Nucleic Acids Res.* **35**, W473–W476 (2007).

116. Krissinel, E. & Henrick, K. Inference of macromolecular assemblies from crystalline state. *J. Mol. Biol.* **372**, 774–797 (2007).

117. Krieger, E. et al. Improving physical realism, stereochemistry, and side-chain accuracy in homology modeling: Four approaches that performed well in CASP8. *Proteins* **77**, 114–122 (2009).

118. Dolinsky, T. J. et al. PDB2PQR: expanding and upgrading automated preparation of biomolecular structures for molecular simulations. *Nucleic Acids Res.* **35**, W522–W525 (2007).

119. Baker, N. A., Sept, D., Joseph, S., Holst, M. J. & McCammon, J. A. Electrostatics of nanosystems: application to microtubules and the ribosome. *Proc. Natl Acad. Sci. USA* **98**, 10037–10041 (2001).

120. Ashkenazy, H. et al. ConSurf 2016: an improved methodology to estimate and visualize evolutionary conservation in macromolecules. *Nucleic Acids Res.* **44**, W344–W350 (2016).

121. Evans, R. et al. Protein complex prediction with AlphaFold-Multimer. Preprint at *bioRxiv* https://doi.org/10.1101/2021.10.04.463034 (2022).

122. Edelstein, A. D. et al. Advanced methods of microscope control using µManager software. *J. Biol. Methods* **1**, e10 (2014).

123. Dunsing, V. et al. Optimal fluorescent protein tags for quantifying protein oligomerization in living cells. *Sci. Rep.* **8**, 1–12 (2018).

124. Schneider, C. A., Rasband, W. S. & Eliceiri, K. W. NIH Image to ImageJ: 25 years of image analysis. *Nat. Methods* **9**, 671–675 (2012).

125. Davis, J. J. et al. The PATRIC Bioinformatics Resource Center: expanding data and analysis capabilities. *Nucleic Acids Res.* **48**, D606–D612 (2020).

126. Lu, B. & Leong, H. W. Computational methods for predicting genomic islands in microbial genomes. *Comput. Struct. Biotechnol. J.* **14**, 200–206 (2016).

127. Sievers, A. et al. K-mer content, correlation, and position analysis of genome DNA sequences for the identification of function and evolutionary features. *Genes* **8**, 122 (2017).

128. Zhou, F., Olman, V. & Xu, Y. Barcodes for genomes and applications. *BMC Bioinform.* **9**, 546 (2008).

129. Dempster, A. P., Laird, N. M. & Rubin, D. B. Maximum likelihood from incomplete data via the EM algorithm. *J. R. Stat. Soc. Ser. B Stat. Methodol.* **39**, 1–38 (1977).

130. Bize, A. et al. Exploring short k-mer profiles in cells and mobile elements from Archaea highlights the major influence of both the ecological niche and evolutionary history. *BMC Genom.* **22**, 186 (2021).

131. Rice, P., Longden, I. & Bleasby, A. EMBOSS: the European Molecular Biology Open Software Suite. *Trends Genet.* **16**, 276–277 (2000).

132. Contreras-Moreira, B. & Vinuesa, P. GET_HOMOLOGUES, a versatile software package for scalable and robust microbial pangenome analysis. *Appl. Environ. Microbiol.* **79**, 7696–7701 (2013).

133. Suzek, B. E. et al. UniRef clusters: a comprehensive and scalable alternative for improving sequence similarity searches. *Bioinformatics* **31**, 926–932 (2015).

134. Katoh, K. & Standley, D. M. MAFFT multiple sequence alignment software version 7: improvements in performance and usability. *Mol. Biol. Evol.* **30**, 772–780 (2013).

135. Steinegger, M. et al. HH-suite3 for fast remote homology detection and deep protein annotation. *BMC Bioinform.* **20**, 473 (2019).

136. Waskom, M. seaborn: statistical data visualization. *J. Open Source Softw.* **6**, 3021 (2021).

137. Tang, H. et al. Synteny and collinearity in plant genomes. *Science* **320**, 486–488 (2008).

138. Bateman, A. et al. The Pfam protein families database. *Nucleic Acids Res.* **32**, D138–D141 (2004).

139. Makarova, K. S., Sorokin, A. V., Novichkov, P. S., Wolf, Y. I. & Koonin, E. V. Clusters of orthologous genes for 41 archaeal genomes and implications for evolutionary genomics of archaea. *Biol. Direct* **2**, 1–20 (2007).

140. Makarova, K. S., Wolf, Y. I. & Koonin, E. V. Archaeal Clusters of Orthologous Genes (arCOGs): an update and application for analysis of shared features between thermococcales, methanococcales, and methanobacteriales. *Life* **5**, 818–840 (2015).

141. Nguyen, L.-T., Schmidt, H. A., von Haeseler, A. & Minh, B. Q. IQ-TREE: a fast and effective stochastic algorithm for estimating maximum-likelihood phylogenies. *Mol. Biol. Evol.* **32**, 268–274 (2015).

142. Kalyaanamoorthy, S., Minh, B. Q., Wong, T. K. F., von Haeseler, A. & Jermiin, L. S. ModelFinder: fast model selection for accurate phylogenetic estimates. *Nat. Methods* **14**, 587–589 (2017).

143. Chothia, C. & Lesk, A. M. The relation between the divergence of sequence and structure in proteins. *EMBO J.* **5**, 823–826 (1986).

144. Holm, L. & Sander, C. Mapping the protein universe. *Science* **273**, 595–603 (1996).

145. Lundin, D., Poole, A. M., Sjöberg, B.-M. & Högbom, M. Use of structural phylogenetic networks for classification of the ferritin-like superfamily. *J. Biol. Chem.* **287**, 20565–20575 (2012).

146. Ye, Y. & Godzik, A. FATCAT: a web server for flexible structure comparison and structure similarity searching. *Nucleic Acids Res.* **32**, W582–W585 (2004).

147. Kanai, R. et al. Crystal structure of West Nile Virus envelope glycoprotein reveals viral surface epitopes. *J. Virol.* **80**, 11000–11008 (2006).

148. Klein, D. E., Choi, J. L. & Harrison, S. C. Structure of a Dengue virus envelope protein late-stage fusion intermediate. *J. Virol.* **87**, 2287–2293 (2013).

149. Gibbons, D. L. et al. Conformational change and protein-protein interactions of the fusion protein of Semliki Forest virus. *Nature* **427**, 320–325 (2004).

150. Voss, J. E. et al. Glycoprotein organization of Chikungunya virus particles revealed by X-ray crystallography. *Nature* **468**, 709–712 (2010).

151. Guardado-Calvo, P. et al. A glycerophospholipid-specific pocket in the RVFV class II fusion protein drives target membrane insertion. *Science* **358**, 663–667 (2017).

152. Zhang, Y. & Skolnick, J. TM-align: a protein structure alignment algorithm based on the TM-score. *Nucleic Acids Res.* **33**, 2302–2309 (2005).

153. Xu, J. & Zhang, Y. How significant is a protein structure similarity with TM-score = 0.5? *Bioinformatics* **26**, 889–895 (2010).

154. Lefort, V., Desper, R. & Gascuel, O. FastME 2.0: a comprehensive, accurate, and fast distance-based phylogeny inference program. *Mol. Biol. Evol.* **32**, 2798–2800 (2015).

Acknowledgements

Author contributions

B.P. conceived the experiments; performed some imaging work; designed, supervised and analyzed cell fusion experiments. C.D. helped devise analysis strategies for k-mer and phylogenetic analysis. C.V. designed, performed and analyzed cell fusion assays. DdeS collected X-ray data, took part in structural analysis and validated metal substructure. D.M. carried out deep homology detection of Fsx1; designed gene content analysis strategies and phylogenetic analysis, collected sequence data; performed k-mer, functional, structural and phylogenomics analyses, built homology models; coded analysis routine pipelines. H.R. supervised the bioinformatics part of the work; designed and performed sequence phylogenetic analyses and phylogenomic surveys. K.F. made constructs of Fsx1 mutants. K.T. and J.J. generated AlphaFold2 models of monomeric Fsx1$_E$. L.J. supervised the biochemical and structural part of the work; collected X-ray data; solved the Fsx1 structure, refined and analyzed it; generated AlphaFold-Multimer models of trimeric Fsx1. M.G. designed bioinformatic strategies; supervised bioinformatic aspects of the work; analyzed sequence and structural data. M.L. performed I.M.E. synteny analyses, phylogenetic and phylogenomic surveys. N.G.B. carried out live imaging and surface biotinylation experiments; assisted with the preparation and design of plasmids; analyzed data. P.S.A. supervised the bioinformatics part of the work and analyzed data. S.N. expressed, purified and crystallized Fsx1; performed SEC-MALS experiments; analyzed SAXS data; collected X-ray data and took part in structure determination, model building and structure analysis. X.L. designed and constructed plasmids; carried out immunofluorescence and western blots for archaeal fusexins in mammalian cells; performed imaging work. D.M., S.N., X.L., N.G.B., M.G., H.R., P.S.A., L.J., and B.P. made figures and tables. D.M., S.N., X.L., M.G., H.R., P.S.A., L.J., and B.P. wrote the manuscript, which was reviewed by all authors.

Competing interests

J.J. has filed provisional patent applications relating to machine learning for predicting protein structures. The other authors declare no competing interests.

Additional information

Supplementary information The online version contains supplementary material available at https://doi.org/10.1038/s41467-022-31564-1.

Correspondence and requests for materials should be addressed to Martin Graña, Héctor Romero, Pablo S. Aguilar, Luca Jovine or Benjamin Podbilewicz.

Peer review information *Nature Communications* thanks the anonymous reviewers for their contribution to the peer review of this work. Peer reviewer reports are available.

Reprints and permission information is available at http://www.nature.com/reprints

Publisher's note Springer Nature remains neutral with regard to jurisdictional claims in published maps and institutional affiliations.

Supplementary Information for

Discovery of archaeal fusexins homologous to eukaryotic HAP2/GCS1 gamete fusion proteins

David Moi[1,2,3]†,, Shunsuke Nishio[4]†, Xiaohui Li[5]†, Clari Valansi[5], Mauricio Langleib[6,7], Nicolas G. Brukman[5], Kateryna Flyak[5], Christophe Dessimoz[2,3,8,9], Daniele de Sanctis[10], Kathryn Tunyasuvunakool[11], John Jumper[11], Martin Graña[7,*], Héctor Romero[6,12,*], Pablo S. Aguilar[1,13,*], Luca Jovine[4,*], Benjamin Podbilewicz[5,*]

[1]Instituto de Fisiología, Biología Molecular y Neurociencias (IFIBYNE-CONICET), Buenos Aires, Argentina.

[2]Department of Computational Biology, University of Lausanne, Lausanne, Switzerland.

[3]Swiss Institute of Bioinformatics, Lausanne, Switzerland.

[4]Department of Biosciences and Nutrition, Karolinska Institutet, Huddinge, Sweden.

[5]Department of Biology, Technion- Israel Institute of Technology, Haifa, Israel.

[6]Unidad de Genómica Evolutiva, Facultad de Ciencias, Universidad de la República, Uruguay.

[7]Unidad de Bioinformática, Institut Pasteur de Montevideo, Uruguay.

[8]Centre for Life's Origins and Evolution, Dept. of Genetics, Evolution and Environment, University College London, United Kingdom.

[9]Department of Computer Science, University College London, United Kingdom.

[10]The European Synchrotron, Grenoble, France

[11]DeepMind, London, UK

[12]Centro Universitario Regional Este - CURE, Centro Interdisciplinario de Ciencia de Datos y Aprendizaje Automático - CICADA, Universidad de la República, Uruguay.

[13]Instituto de Investigaciones Biotecnológicas Universidad Nacional de San Martín (IIB-CONICET), San Martín, Buenos Aires, Argentina.

*Corresponding authors. Email: mgrana@pasteur.edu.uy, eletor@fcien.edu.uy, paguilar@iib.unsam.edu.ar, luca.jovine@ki.se, podbilew@technion.ac.il

†These authors contributed equally to this work.

This PDF file includes:

a

Q89292 Yellow fever virus	(blue)
P14336 Tick-borne encephalitis virus	(blue)
P12823 Dengue virus type 2	(blue)
P03315 Semliki forest virus	(blue)
Q1H8W5 Chikungunya virus	(blue)
P08668 Hantaan virus	(blue)
P08563 Rubella virus	(blue)
P03518 Rift valley fever virus	(blue)
D2W008 *Naegleria gruberi*	(green)
CRY7J9 *Branchiostoma floridae*	(green)
T1ISJ2 *Strigamia maritima*	(green)
G5ECA1 *Caenorhabditis elegans*	(green)
A0A0K2SR10 *Dictyostelium discoideum*	
A0A5J4UPK0 *Streblomastix strix*	
A4GRC6 *Chlamydomonas reinhardtii*	
A0A0D2WS34 *Caspaspora owczarzaki*	
A0A1X7UDL0 *Amphimedon queenslandica*	
M1V8A6 *Cyanidioschyzon merolae*	
A9V179 *Monosiga brevicollis*	
D2VN83 *Naegleria gruberi*	
A0A060A682 *Tetrahymena thermophila*	
A0A0K0VK49 *Malawimonas californiana*	
F4JP36 *Arabidopsis thaliana*	
R7UM94 *Capitella teleta*	
Q4DKJ2 *Trypanosoma cruzi*	
A3FEQ2 *Hydra vulgaris*	
RLI53188 *Cand. Thorarchaeota archaeon*	(red)
WP_049937247 *Haloplanus natans*	(red)
WP_007110832 *Natrinema altunense*	(red)
Fsx1_E	(red)
WP_174701778 *Haloterrigena* sp.	(red)
RLG58774 *Cand. Geothermarchaeota archaeon*	(red)
WP_058826362 *Haloferax* sp. Q22	(red)

Virus (class II)
Eukarya (EFF-1)
Eukarya (HAP2/GCS1)
Archaea (Fsx1)

b

NaFsx1   HQ22Fsx1

HnFsx1   Fsx1

c

αV5

αActin

d

% of multinucleation

Vector, AtHAP2, NaFsx1, HQ22Fsx1, HnFsx1, Fsx1

e

% of multinucleation

pH 7.4   pH 5.5   pH 7.4   pH 5.5
      Fsx1   VSV G

3

Supplementary Fig. 1. Sequence similarities between fusexins and ectopic expression of archaeal fusexins in mammalian cells.

a Fsx1s are members of the fusexin superfamily. HMM homology probabilities of fusexins and archaeal candidates ectodomains evidence sequence similarity between archaeal candidates and sexual (HAP2/GCS1) fusexins. HMMs were constructed for each ectodomain sequence (UniProt and NCBI identifiers shown). HAP2/GCS1 and EFF-1 sequences were chosen from representative species of the major eukaryotic lineages where these fusexins are present. Flavi-, alpha-, rubi- and bunyaviruses encompass all currently known viral fusexins. All vs all probabilities of homology as determined by HHblits were clustered along rows and columns using UPGMA with Hamming distance. Several sequences selected for this analysis have corresponding crystal structures: Yellow fever virus (UniProt Q89292], PDB 6IW5[1]), Chikungunya virus (UniProt Q1H8W5, PDB 3N43[2]), Dengue virus (UniProt P12823, PDB 1OAN[3]), Semliki forest virus (UniProt P03315, PDB 1RER[4]), Tick-borne encephalitis virus (UniProt P14336, PDB 1SVB[5]), *Arabidopsis thaliana* (UniProt F4JP36, PDB 5OW3[6]), Rubella virus (UniProt P08563, PDB 4ADG[7]), *Chlamydomonas reinhardtii* (UniProt A4GRC6, PDB 5MF1[8]), Hantavirus (UniProt P08668, PDB 5LK1[9]) and Rift valley fever virus (UniProt P03518, PDB 4HJC[10]). Although all of the sequences used as input belong to the fusexin structural superfamily, HMM vs HMM comparisons can only detect homology within subsets of the superfamily.

b-d Ectopic expression of archaeal fusexins in BHK cells. **b-c** Ten archaeal genes were synthesized (Supplementary Table 5) and independently expressed in BHK cells using an inducible promoter. **b** Immunofluorescence (n=2) and **c** Western blot showing ectopic expression detected with anti-V5 antibody (n=2). EFF-1 from *C. elegans* was used as a positive control. NaFsx1, *Natrinema altunense* Fsx1. HQ22Fsx1, *Haloferax* sp. Q22 Fsx1. HnFsx1, *Haloplanus natans* Fsx1. LKMP01000007_1 was obtained from Nanohaloarchaea B1-Br10_U2g21 LB-BRINE-C121. Fsx1 (the protein subsequently characterized), SAMEA2619974 and sequences starting with "330" were obtained from metagenomic databases (see Supplementary Table 5 for complete accession numbers). M, marker. Scale bars, 10 µm.

d Quantification of multinucleation in cells expressing archaeal fusexins. Cells were transfected with archaeal fusexins cloned into pCI::H2B-RFP/GFP vectors

separately. 48 h post-transfection, immunofluorescence was performed with anti-V5 antibody. Empty vector pCI::H2B-RFP or pCI::H2B-GFP co-transfected with myr-EGFP were the negative controls. AtHAP2 was used as a positive control. Multinucleation was determined as the ratio between the number of nuclei in multinucleated cells and the total number of nuclei in multinucleated cells and expressing cells that were in contact but did not fuse. The percentage of multinucleation is presented as individual data and means ± SEM of independent experiments (n≥4). Total number of nuclei counted in multinucleated cells and in cells in contact n ≥ 1,000 for each experimental condition. Comparisons were made with one-way ANOVA followed by Dunett's test against the empty vector. **** p< 0.0001. **e** VSV G activity, but not Fsx1, is enhanced at low pH. Quantification of multinucleation in cells expressing Fsx1 or VSV G. Cells were transfected with pCI::H2B-RFP bearing the coding sequence for Fsx1 or VSV G. 48 h post-transfection, a 5-minute incubation at pH 5.5 buffer was performed to some cells. After 2 h, cells were fixed and immunofluorescence was performed with anti-V5 antibody or anti-G for Fsx1 and VSV G, respectively. Multinucleation was determined as the ratio between the number of nuclei in multinucleated cells and the total number of nuclei in multinucleated cells and expressing cells that were in contact but did not fuse. The percentage of multinucleation is presented as individual data and means ± SEM of three independent experiments. Total number of nuclei counted in multinucleated cells and in cells in contact n ≥ 1,000 for each experimental condition. Comparisons were made with two-way ANOVA. ns, non-significant, ** p < 0.01. Source data are provided as a Source Data file.
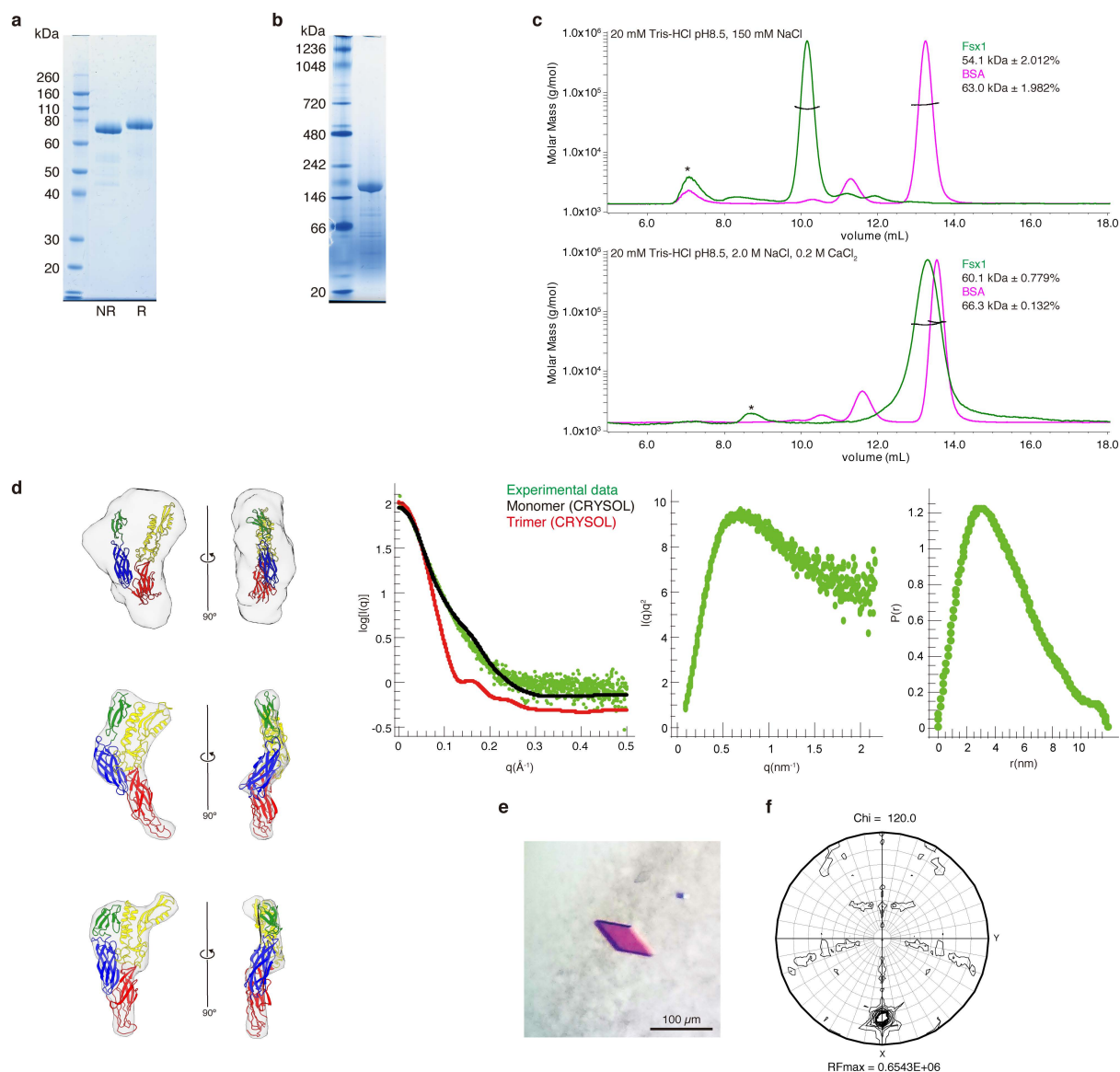
Supplementary Fig. 2 The Fsx1 ectodomain is a monomer in solution but crystallizes as a trimer.

a, b SDS-PAGE (a) and blue native PAGE (b) gels of purified Fsx1 ectodomain (Fsx1$_E$). NR; non-reducing conditions. R; reducing conditions (see Supplementary Fig. 11). n=2.

c Size exclusion chromatography-multiangle light scattering (SEC-MALS) shows that, although Fsx1$_E$ has a very different elution volume depending on the salt concentration, it is a monomer in solution in both normal and high salt conditions. BSA, whose elution volume does not change significantly at different salt concentrations, is used as a control. Asterisks indicate the high-molecular weight aggregate. n=2.

d SAXS analysis of Fsx1$_E$. Left panel, The SAXS envelope of Fsx1$_E$, obtained by averaging 20 *ab initio* shape reconstructions, is consistent with the crystallographic model of Fsx1$_E$ chain A (top). However, as also indicated by the corresponding Kratky plot (see below), its relatively broad profile suggests that there is some flexibility between the domains of Fsx1 in solution. Accordingly, improved agreements can be obtained by flexibly fitting the Fsx1$_E$ monomer model to envelopes generated by averaging the two most abundant clusters of SAXS models (middle and bottom). Center-left panel, Comparison of the experimental SAXS profile of Fsx1$_E$ (green dots) and theoretical scattering curves calculated from the refined coordinates of Fsx1$_E$ chain A (black dots) or the whole Fsx1$_E$ trimer (red dots). Center-right panel, the Kratky plot of Fsx1$_E$ suggests the presence of significant flexibility between the domains of the monomeric protein. Right panel, Pairwise interatomic distance distribution of Fsx1$_E$.

e Representative rhomboidal plate crystal of Fsx1$_E$.

f The Chi=120 section of the self-rotation function of Fsx1$_E$ (calculated using a 67.3-2.6 Å resolution range) shows a prominent peak with a height of 72% of the origin peak.
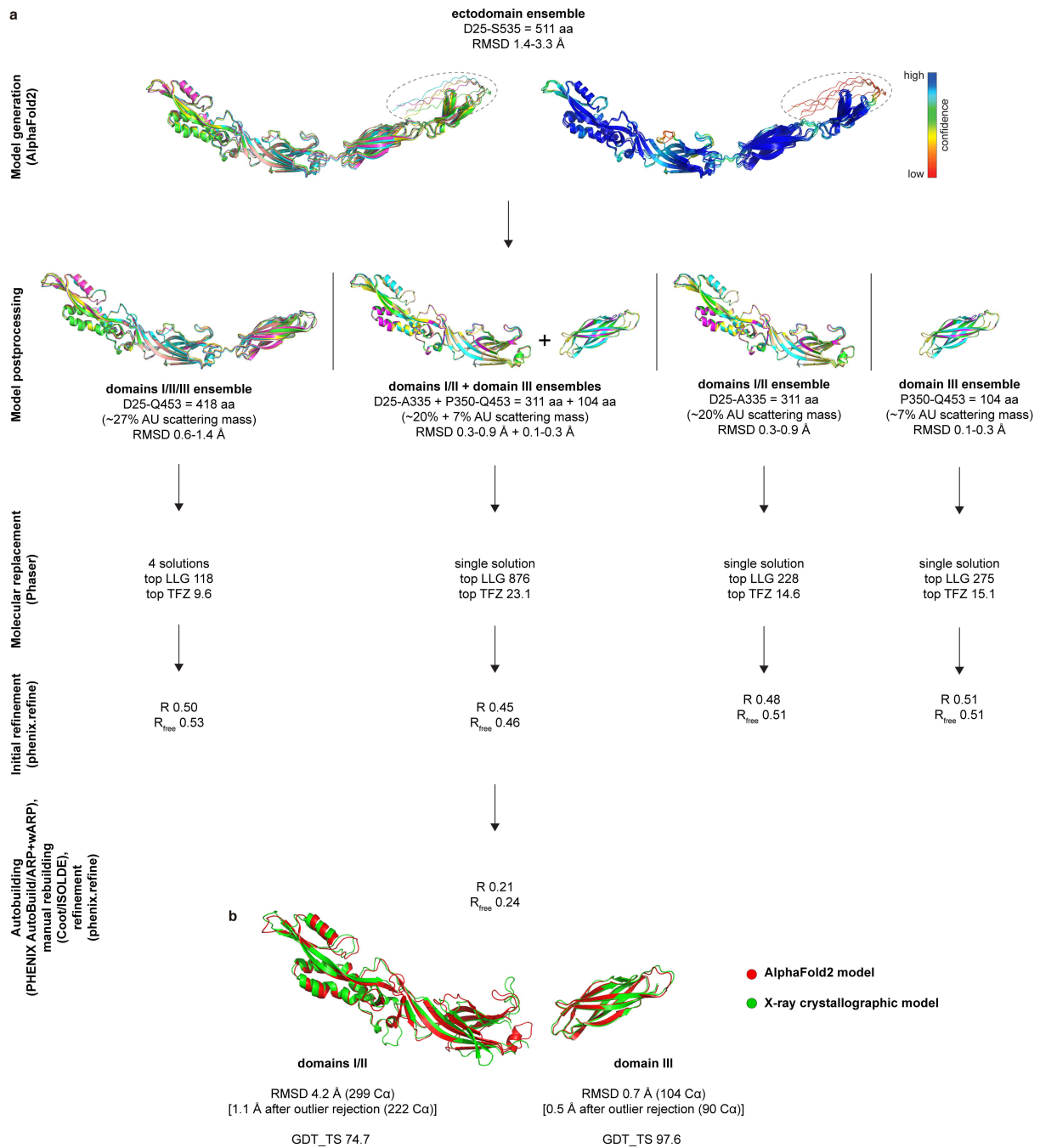
Supplementary Fig. 3 AlphaFold2-aided MR phasing of Fsx1$_E$.

a Flowchart of Fsx1$_E$ structure determination using different AlphaFold2 model fragments or a combination thereof. The top panel shows a superposition of the five initial predictions, colored by model (left) or by confidence (right); the dashed ovals indicate C-terminal residues D510-S535, which were predicted with low confidence by AlphaFold2. aa, amino acid; AU, asymmetric unit.

b Comparison of the top-ranked AlphaFold2 prediction and the refined experimental model of Fsx1 domains I/II and III.
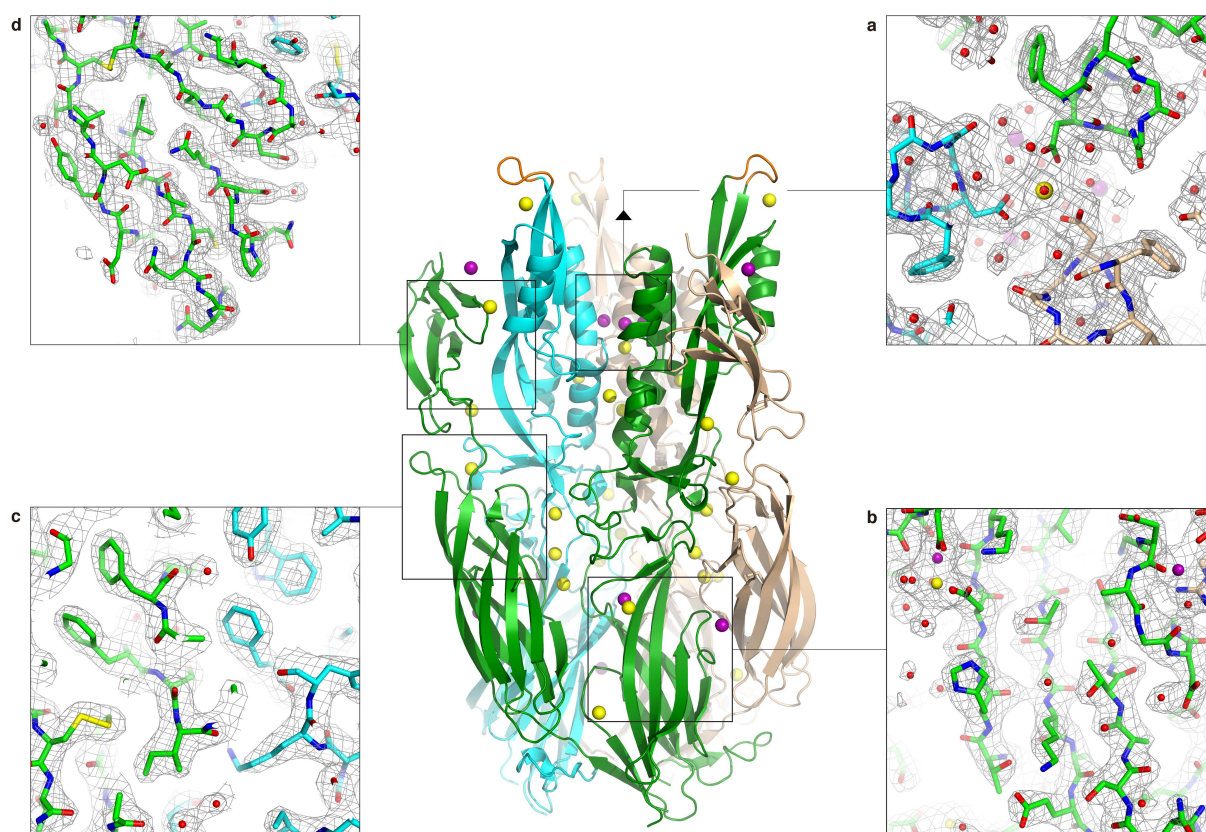
Supplementary Fig. 4 Details of the electron density map of Fsx1$_E$.

a View of the domain II helical bundle, looking down the molecular three-fold axis from the center of the structure towards the putative fusion loop end. Domain II α1 helix residues D260 and D263 coordinate a Ca^{2+} ion sitting on the NCS axis and three symmetrically positioned Na$^+$ ions, respectively. The refined *2mFo-DFc* electron density map, contoured at 1.0 σ, is shown as a gray mesh superimposed onto the protein model in stick representation. Fsx1 subunits and metal ions are coloured as in Fig. 3c.

b Section of the map centered around β-strands D$_0$, E$_0$ and F$_0$ of domain I.

c Closeup of the map region where domain III of one protein subunit interacts with domains I and II of another. Clear density for the C$_3$389-C$_4$432 disulfide is visible near the bottom left corner.

d Map of domain IV. The conserved C$_7$490-C$_8$506 disulfide is at the top left corner, whereas C$_6$477 of the C$_5$457-C$_6$477 disulfide is visible at the bottom and the domain II C$_1$125-C$_2$155 disulfide of the adjacent subunit can be seen on the top right corner.
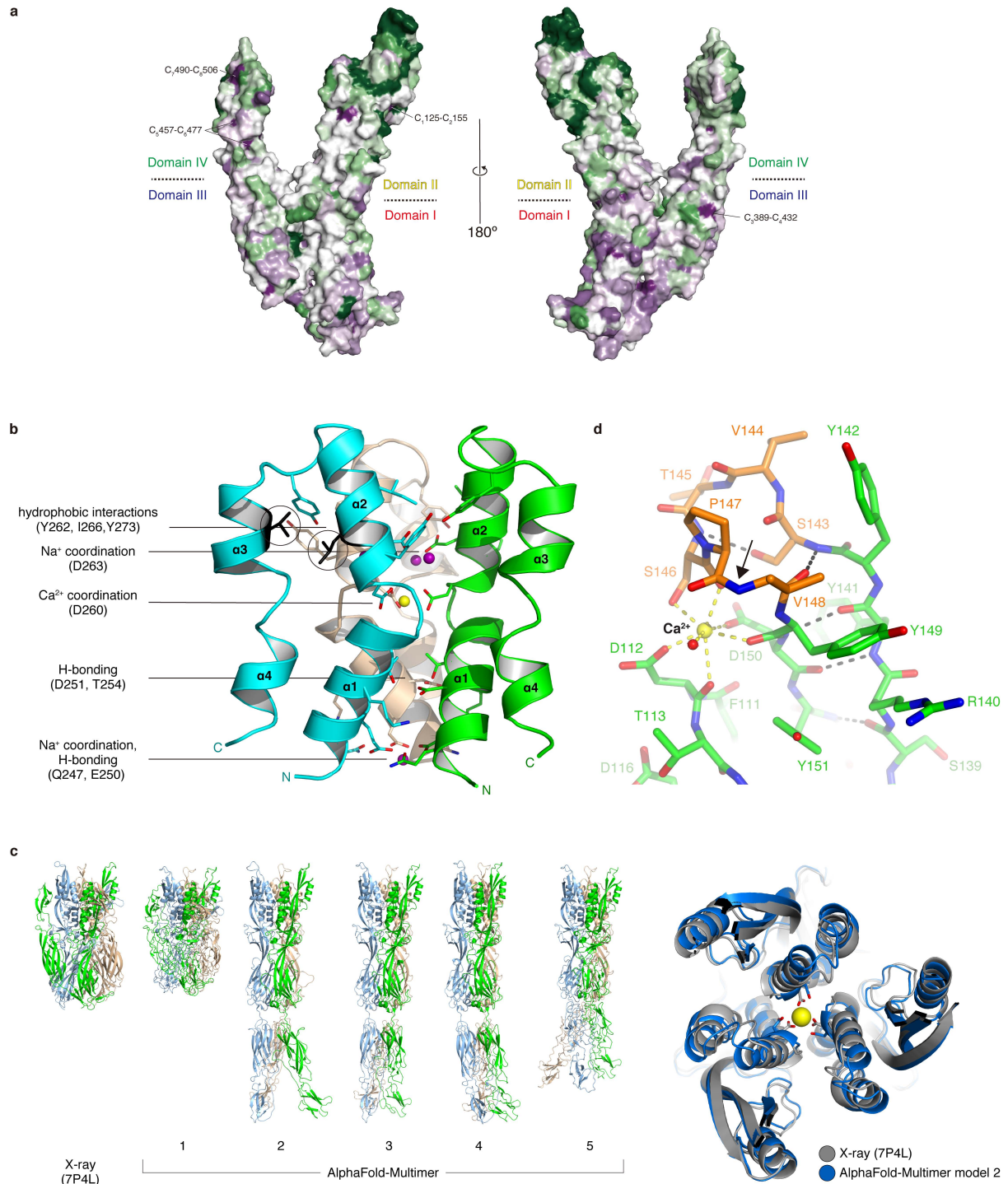
Supplementary Fig. 5 3D mapping of the evolutionary conservation of Fsx1 residues and key structural features of its domain II.

a Fsx1 domains I and III are more evolutionarily conserved than domains II and IV. Surface representation of the Fsx1$_E$ monomer, with residues coloured from green to violet by increasing conservation among archaeal homologs. Approximate domain

boundaries are marked, and the position of the four highly conserved disulfides of Fsx1 is indicated.

b Helices α1 and α2 of domain II form a six-helix bundle around the molecular three-fold axis. Subunits are shown in cartoon representation and coloured as in Fig. 3c, with residues mediating direct or ion-mediated interactions between chains depicted in stick representation (for clarity, water-mediated interactions are not shown). The side chains of residues α2 L264 and α3 V278 (black circles), which face each other in the $Fsx1_E$ structure, are both replaced by Cys in the sequences of *Halogeometricum borinquense* and *Halobonum* sp. (Supplementary Fig. 6), suggesting that an additional disulfide bond stabilizes the helical bundle of the Fsx1 homologs from these species.

c AlphaFold-Multimer prediction of the $Fsx1_E$ homotrimer (left panel) generates models that either approximate the overall post-fusion conformation of the crystal structure (albeit with significant interchain clashes; model 1) or adopt an extended conformation that resembles an intermediate state thought to exist before fusion[11] (models 2-5). In both cases, the models contain the experimentally observed six-helix bundle and, as shown for the Ca^{2+} coordinated by D260 (yellow sphere), in some instances even reproduce the orientation of side chains that bind ions in the crystal (right panel). Considering that these residues are poorly conserved in other homologs of Fsx1 (Supplementary Fig. 6) and taking into account that AlphaFold2 does not explicitly predict ions, this suggests that Ca^{2+} and Na^+ stabilize the trimeric structure of Fsx1 rather than being required for its formation.

d Structure of the fusion loop of $Fsx1_E$. The domain II region encompassing the loop is shown in the same orientation as in Fig. 3f, with black and yellow dashes indicating protein hydrogen bonds and the coordination of the Ca^{2+} ion, respectively. Note how binding of the ion locally twists the protein main chain, with the peptide bond between P147 and V148 adopting a *cis* configuration (black arrow).

a

Multiple sequence alignment (Fsx1E/7P4L and haloarchaeal homologues).

Block 1 — secondary structure: A0, B0, C0, D0 (residues ~30–80)

```
                    A0              B0                 C0                              D0
                    30        40          50              60            70          80
Fsx1E/7P4L          DSITYNSGTSEFFDGDVFAIEVTADQSTDE...IDIYLG............ASELSEKTDGEVNQDLSIEFTHQDSKLKY
Haloterrigena sp.   DRIDFQS.NSDFFGNEAFVISYLSDFSTDK...IDVVLG............QSDLSDAADGEVSQDLSIFVESQNTYAEY
Halovivax sp.       DSIQFDS.NSKFFSGEVFVIQYISNFDTDR...IDVVLS............SNDLEQAADGEVDQDLSIDVVQQDTAALY
Natrinema_altunense DQIEYTS.NSEFFDGEVFVINYIGDRTTDK...IHAEIP............SELASAADGEVTKELTIDITSQETYARY
Haloferax Q22       DTVTYES.NSDFFDGQVLQVGYTSNFATDK...INVYLS............ESKIESETGAVADEPITFDVSHQNTYAKY
Haloplanus natans   DTVSYKS.NSEFFDGEVLQAGYVSNFATDK...INVHLG............ASEIESKTGATAREDLTLSVSHQNTYARY
Halogeometricum borinquense DEVFIDN.NARERSG.............DKAWVIDANLGCDNKIFGGGGTIAAEDISSDGVSALKDFSLGINNFEAWFSN
Halobonum sp.       DEVRIES.SVLEFSG.............DRGWSINAAAGCDNKIVGGTTTLPKDSISTDEASAERDFTLGLTSFDAWFYQ
```

Block 2 — secondary structure: a, TT, b, αS, TT, c (residues ~90–140); Fusion Loop

```
                    a    TT      b            αS        TT              c
                    90        100        110        120        130            140
Fsx1E/7P4L          STSTSDELRDIVTLTTTYYEDGF.DTEQDAI.....DAIKSDCYDLNQNG....NG....SGR....YSRYYSVT.SPVY.
Haloterrigena sp.   SIADSVEQD.LVNLEPIKSDPL.SSSDTAD.....DWAVQHCYDIGQNG...........NIQ....YVVQSTLT.FTGT.
Halovivax sp.       SISPSGEPR.LGNLELTTAEK..STFEELD.....RWAWDTCYDINGDG...........GKE....YAYESVLT.WSGT.
Natrinema_altunense STTSTSLSR.IYAFKAINSEVFTDTSSSEVESRKQSWAEQNCYDIDGDS.......EIEQGDDYTQRFWVD.GAIA.
Haloferax Q22       PTQDTGLES.ITGWDAVKKTV..SSKQELW.....DWTTTNCVDTNDAGTFTVDGYGTTDVD....ARANRWFDTWTGQY
Haloplanus natans   PLQETGLKK.IYGWEGMKKTF..TKDQLW.....NWVTSNCADFTEGGVAIGD..RTSKVE....AAAKSWYDYWTGSY
Halogeometricum borinquense PVI........DDRENVYRVR..MATY.NCGF....DG.......GSNDQAKQDFQAESPYT.SQAET
Halobonum sp.       GIR........DTRSPVYTVR..SAVFSDCGLFSGDEC.......PNSQDDCDAFQAESSES.SPAEF
                                                    1                                            Fusion Loop
```

Block 3 — secondary structure: d, E0, TT, F0, TT, G0, H0 (residues ~150–210)

```
                         d            E0      TT    F0      TT     G0                  H0
                    150        160        170        180        190        200        210
Fsx1E/7P4L          DY...EIYCPQKNEKLATPAYIDNPDEIFTAKAELQAGDKTIQSATLSNGDAGDGTVTDLG....D.SKISWNGNL.
Haloterrigena sp.   KY....EVYCARYNGEWGPIGNIQTPRELFETTWQVEADDEPAQTPTLSNNDIGEGRTTRIG....DHVVVQWDGNV..
Halovivax sp.       VY....RGYCARENGFYGPVGRITKDREVFTTEWRVEASGESAQTALSNGDTGRGVVSDIG....DHVKVRWDGNL..
Natrinema_altunense DIYYN.AQVYCWRENGYYGNIAELSSPDKEFEAAEVEVKADGETPQSTTLSNSDLGQGRCDNIG....EYVRACWTGSLN..
Haloferax Q22       KY....TIYCWQRNDYYGAVANDIGSPDEVFRTEWRLQAGDKNPQTAVIITNGDGGTGVTNLG....RYAKVSWDGSL..
Haloplanus natans   NY.....QAFCLRKNGYYGDVADIGSPDEIFRTEWRLQAGDKNPQTAITTNGDGGSGVVSNLG....RYAKVKWQGNI..
Halogeometricum borinquense RRTAVTELYCPKVEKTGEAASFGLNQDSSFSATVQASADGRSDSDPISKDDPTASVNVGDVNRDGDSEEALVTWRGSPIG
Halobonum sp.       RYTDGSDLYCYKVERVGSVSDWTLAQGTDFDGTFTVEAAGRSDTDTISKDDVTARLQVADVNVGDREHAHVTWTGSLAG
                         1
```

Block 4 — secondary structure: η1, f, TT, η2, g, α1, α2, α3, α4 (residues ~220–280)

```
                              η1    f  TT  η2  g         α1              α2          α3       α4
                    220        230        240        250        260        270        280
Fsx1E/7P4L          .....DLGASEPENSRV..IALYSNDFENGWRIGNKQSYEDVKTFIGGGDAYDLLI.DWQDGTYTASEVEDELVNTDANQ
Haloterrigena sp.   .....DLGRDPPNPGDEGAAALYVRT.ANDWRVISASRYDDWDTYV.RDTLVTRYD.DWAEGSISQDELRREI.QSRAES
Halovivax sp.       .....DTGEEAPPADKE..YALHGNQFEDGWRIIDRGRYADWRQHV.R.DLDTAYE.QWRDGDRSRDYLQNQL.DTATEQ
Natrinema_altunense .....PTGEGVPEPYNV..YAIHSNTFSPEWRVISAERYSSYNSYV.ENNLYSQIE.AWKEGSLSQEEVVSTA.NDQAAQ
Haloferax Q22       .....STGENPPLVDDE..YALHSNDYEGGWRVISELYSSYQSFV.QNNADDLLG.EWGAGLTTESHIESEM.NGKAEE
Haloplanus natans   .....DTGQNPPLVDDE..LAIHGNNYEGGWRVISEQRYDNYWNYI.KNDGNRLLD.KWKSGDYSESYIEGLL.NGKAEN
Halogeometricum borinquense DTRSIDISPVKPVCDSN..CERPTNNVD..WIVGSQDLFTEWNQYD.EGGFDQCVQNSNIDRLS...CVIRY.NDRAAN
Halobonum sp.       ELRSMDLSEFIATCENN..CEQHTNEIS..WGVGAESQYSAYSAYD.GGGFQSCVE.TEVDANGAPHTCVNAY.NNRASN
```

Block 5 — secondary structure: I, I0', I0, J0, A, A (residues ~290–360)

```
                                            I    I0'     I0        J0      A         A
                    290        300        310        320        330        340        350       360
Fsx1E/7P4L          AVEEASSSTTDLVNAKVKDSSLDTGSFVY..DTPELLSYPSTVYVDAGENGYIEVTKPTGDPDIIS.TSSTEIKEGDEG
Haloterrigena sp.   AASVYSSS..DLATASTSGDA.SSGHLRL..NMDGELAWPQQTVYVDGAE..YVRVEKPVGTPEIVS.TDGDRFGELESG
Halovivax sp.       AAAEYTGS..PLTSAETSVYTDGQLRL..EMDTDLAVYPSTVYVDGAE..YVSVSKPVGRPRITS.TNGDEFGELDTG
Natrinema_altunense AAQRVSSG..SFTDYQVEDSSYENGQIRL..NPSYDLAVYPETFTFVDGAD..YISVEKPVGEPRIIVM.VEGDEFGEKQSG
Haloferax Q22       AASBFTES..PLSDSEILDSSFQNGAFKL..DMERSLMYPEQSVYVDGAGNDYIATISKFVGKPRITV.TSGAEFGELGQG
Haloplanus natans   AQKRYSES..PLANAEVLDSSFQSGALKA..DMDSRLAYPENVYVDAGENGYITVSKPVGKPRIIVS.SSGASFGELSSG
Halogeometricum borinquense VFADSSRTIQDQTSIDIARVDVIGTELRMYTEKAELVERPDFRITVD.AD..WIGFDTRVGRFVFQTPLPEIDIVGNSRT
Halobonum sp.       VFADASSGIRSFAGFDVADVRFQDGQIQVVADRGTAIDRPEFRILVD.AD..WIGFSIPTVQPRFES.VPDVTVIGNSQS
```

Block 6 — secondary structure: B, C, D, D, E, F (residues ~370–440)

```
                    B           C          D    D         E          F
                    370        380        390        400        410        420        430        440
Fsx1E/7P4L          TVTATVENVGDGEGEFSGRLS.SCGEGFSIVDDQNTKNVGAGESVTYSFDVAFSSVSSESKEISGSCTFEVNGV...ESS
Haloterrigena sp.   TVSMTVENVGDGDGSFSARIQ.SCSSGFGFDDVQQTEDVAESSTVTYEFDVSLLTDA..DDEVSGQGTVEVANQ..EGFA
Halovivax sp.       YVTGTVRNVGDGEGSFAGRLT.SCSDGFSFDSTQRTQRVDPGASVTYEFPVSFTSTG.DQDEVGGSGTIEVTDTG.SGER
Natrinema_altunense TVTAEVRNTASYEGSFSARVS.KCSDSFGYDSLQETKTVGPGETVSFDFRVSFTSDSFDQKTVSGSGEIVVSDTGDSSNS
Haloferax Q22       TISVEABNVGDSEGSFSARTD.SCGEYFSGNSLQDTQRVSPGGTASFDFRVTFTSTSMTQSEFSDQCEVVVEDTG.SGNE
Haloplanus natans   RISVDVKNVGAEPGSFSARAG.SCSQYFQADALQNTKRVAPGETASYSFRVTFTSTSMQQASYTGRCSITVEDTG.SGRE
Halogeometricum borinquense TADFQVLNDAAG.GSHRIRVNLECPRPLSGGS..TAKRVQAGISETFSVPIEIGATN....TRTYTCDVEAFDT..DDDS
Halobonum sp.       TAAIDVRNTG..LETGEMQVFAECPSPISGGS..DTAMVPSGETGRFFIPISAGPTE....TRDYTGTVTSQDT..DTAE
                                              2                                            2
```

Block 7 — secondary structure: G, A1, TT, B1, TT, C1, D1, TT, E1 (residues ~450–510)

```
                    G             A1    TT    B1     TT   C1     D1    TT     E1
                    450        460        470        480        490        500        510
Fsx1E/7P4L          DSTSVSVTGIQQSDCNPGDQRREKNEND...RWEIYTCQDNCLTYEYDVTCAEDEKAVAQGDNQFS......CEKQD
Haloterrigena sp.   VTDDVEVTGIPEQTCTPGERFDQVDANG...VYTIYECTEDCSDYFVDEFCGHGEETDIVDDELQ......CVEEE
Halovivax sp.       DFATAAVTGVQENECSPGERFSKVASGG...QHVIYQCSEDCMTFTEVERCEQGEEARQI.DSELQ......CVVPD
Natrinema_altunense DTAVVVEATQSNECTPNEEFVRTINST...HSRILECSSDCLTTTEVDVCGDGEEAAFR.DSSWT......CVSDG
Haloferax Q22       VSASVSVTATQEDECTEGDETKKEKQVNGETVDVIMSCT.NCLKLEEDEVCSADEEARYI.DDDVQ.....YECRDKD
Haloplanus natans   VSTSVSVEATQQSECTQGKEIVKQKNGN....DVIYSCP.DCLKIQKQDTCTGELKAVFV.NNDIQ.....YDCREEG
Halogeometricum borinquense TRAIAQVTVNAQNSCPDQDEDGVCDQFDA..CPSVAGASTNGCGPTK..EVCGDSI......DNNGNGRVDEDCGTTG
Halobonum sp.       TAQTTELTVHAKTSCPDGDGDGVCDQLDA..CPDEPGAGSNNGCPLE..EVCGNDV......DDDGDGRVDEGCEEPG
                                      3                 3            4                      4
```

12

b

Fsx1E/7P4L — A0 · B0 · C0 · D0 · *a* · *b* · αS · *c* · Fusion Loop · *d* · E0 · F0 · G0 · H0 · η1 · *f* · η2 · *g* · α1 · α2 · α3 · α4 · I · I0' · I0 · J0 · A · A · B · C · D · D · E · F · G · A1 · B1 · C1 · D1 · E1

Sequence rows (multiple sequence alignment):

- Fsx1E/7P4L
- *Haloterrigena sp.*
- *Halovivax sp.*
- *Natrinema altunense*
- *Haloferax sp. Q22*
- *Haloplanus natans*
- *Halogeometricum borinquense*
- *Halobonum sp.*
- HAP2 *A. thaliana*
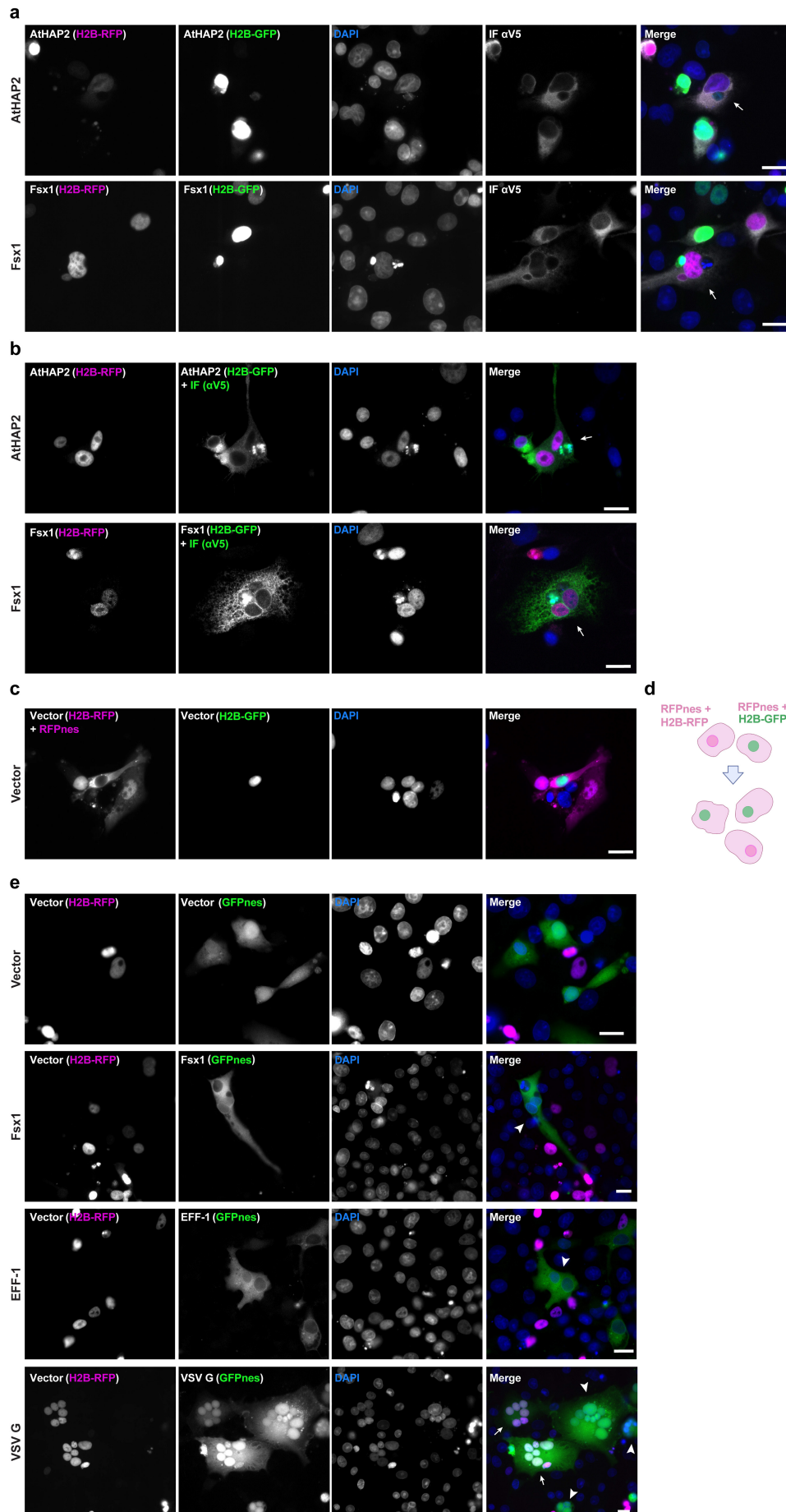- HAP2 *C. reinhardtii*
- 6E18

Supplementary Fig. 6 Alignments of archaeal Fsx1s from cultivated species and with HAP2 fusexin ectodomains.

For reproducibility, no gap or block was altered from alignments. Identical column residues are depicted in bold white on a red background; conserved positions are boxed and labeled red. On top are displayed secondary structure elements and sequence numbering corresponding to Fsx1$_E$/7P4L.

a Archaeal sequences from pure culture genomes (PCGs), with N- and C-terminal regions cropped to match Fsx1$_E$ (PDB 7P4L). Secondary structure elements are shown within boxed domains, coloured and labeled following the previous nomenclature (domain I, red; domain II, yellow; domain III, blue). Disulfide bonds are indicated by orange numbers below the alignment. Additional, lineage-specific cysteines are black-boxed and depicted in bold white. The fusion (cd) loop is highlighted in light orange within the alignment; as in eukaryotic HAP2, it has poor sequence conservation (Supplementary Fig. 5a) but shows a high prevalence of hydrophobic residues (Fig. 6). Domain IV (green) has relatively poor sequence conservation within archaea (Supplementary Fig. 5a), yet preserves its disulfide bonds.

b Sequence alignment of HAP2s from *A. thaliana* and *C. reinhardtii* (PDB 6E18[12]) and archaeal fusexins from cultivated genomes. Of note are the inserts of HAP2 relative to Fsx1s, as well as the absence of domain IV, which seems confined to Archaea. The conserved fusion loop region is orange shaded; lineage-specific cysteines black boxed. C-terminal regions shaded with a gradient from gray to white indicate portions absent from Fsx1$_E$ (PDB 7P4L) and HAP2 (PDB 5OW3 and 6E18) crystal structures, either with no electron density or absent from the expression construct. HAP2s introduce gaps; for clarity, disulfide bonds shown in panel a are omitted and replaced by secondary structure elements from PDB 6E18.

f

Fsx1 WT (H2B-RFP)	**Fsx1 WT (GFPnes)**	**DAPI**	**Merge**
ΔFL→AG₄A (H2B-RFP)	**ΔFL→AG₄A (GFPnes)**	**DAPI**	**Merge**
ΔDIV→EFF-1 st. (H2B-RFP)	**ΔDIV→EFF-1 st. (GFPnes)**	**DAPI**	**Merge**
ΔTMs→GPI (H2B-RFP)	**ΔTMs→GPI (GFPnes)**	**DAPI**	**Merge**
ΔTMs→EFF-1 TM (H2B-RFP)	**ΔTMs→EFF-1 TM (GFPnes)**	**DAPI**	**Merge**
HAP2ΔTM→GPI (H2B-RFP)	**HAP2ΔTM→GPI (GFPnes)**	**DAPI**	**Merge**

Row labels (left margin, top to bottom): Fsx1 (WT); ΔFL→AG$_4$A; ΔDIV→EFF-1 stem; ΔTMs→GPI; ΔTMs→EFF-1 TM; AtHAP2ΔTM→GPI

Supplementary Fig. 7 Fsx1 mediates bilateral cell-cell fusion and structure-function analysis.

a Images from Fig. 4a in each separate channel (red, green, DAPI and far red) and merge. Scale bars, 20 μm. n=4.

b Multinucleated cells containing green nuclei (H2B-GFP) and magenta nuclei (H2B-RFP) (arrows). Immunofluorescence against the V5 tag was performed in green to facilitate counting. n=4.

c, d in the negative control, cell-cell fusion was measured by content-mixing, indicated by the appearance of multinucleated cells containing green nuclei (H2B-GFP) and magenta nuclei (H2B-RFP). To reveal the cytoplasm of the transfected cells, a plasmid encoding for cytoplasmic RFP (RFPnes) was co-transfected. n=3. **c** Representative images of mononucleated cells with a green or red nucleus. DAPI staining is shown in blue. **d** Cartoon showing the experimental design for negative control.

e Images from Fig. 4d in each separate channel (red, green and DAPI) and merge. Multinucleated GFPnes only (arrowheads) or mixed cells (arrows). Scale bars, 20 μm. n=3.

f Images from Fig. 5c in each separate channel: red (RFP); green (GFP) and blue (DAPI) and the merged images. Scale bars, 20 μm. n>3 as specified in Fig. 5b for each condition.

g Surface expression of Fsx1, mutants and eukaryotic fusexins. For colors and abbreviations see legend of Fig. 2. BHK cells were transfected with FLAG-tagged

Fsx1 (WT) and the indicated mutants; the FLAG tag was inserted before the membrane anchor. Non-permeabilized staining using anti-FLAG antibody showed surface expression of Fsx1 and the various mutants as detected by immunofluorescence. The proportion of non-permeabilized cells showing surface expression was: AFF-1-FLAG (negative control; 0%, n=2), Fsx1-FLAG (3.9%, n=1), Fsx1-ΔFL→AG$_4$A-FLAG (4.4%, n=1), Fsx1-ΔDIV→EFF-1 stem-FLAG (2.6%, n=1), Fsx1ΔTMs→EFF-1 TM-FLAG (3.3%, n=2), Fsx1ΔTMs→GPI-FLAG (32.6%, n=3), AtHAP2ΔTM→GPI-FLAG (22.8%, n=2). Total number of cells with red nuclei counted n ≥850 for each experimental condition; the percentage of surface expression was counted by at least two different observers. Another group of transfected BHK cells in parallel were fixed, permeabilized and stained with anti-FLAG antibody. Permeabilized staining showed the main distribution in the cytoplasm (endoplasmic reticulum) of Fsx1 WT, Fsx1 mutants and AtHAP2ΔTM→GPI mutant. *C. elegans* AFF-1 tagged with FLAG at the C terminus (cytoplasmic tail) worked as a negative control for non-permeabilized staining. Scale bars, 10 μm.

Sequences from MAGs, PCGs & metagenome assemblies

* Final analysis shows elements > 20 kbp

getorf
minimum 30 residues
Genetic Code 11
(Bac+Arch)

INITIAL HOMOLOG DETECTION

Database annotation

Each sequence from annotation corresponds to one ORF

ORFs

Groups with some ORF corresponding to sequence within IMEs

get_homologues;
cov >= 70% AND %id >= 35;
no in-paralogues allowed

Initial homolog group
("corrected" annotation)

jackhmmer -N 1
(phmmer equivalent)

Homolog group 1

Homolog group 2

(...)

Homolog group N

Hits are added to enrich homolog groups

Filters:
target length >= 100
query lenth *1.5 >= target length
full qcov (full aln/qlen) >= 0.5
full seq e-value < 1e-15

EXPANSION/COLLAPSE OF HOMOLOGOUS GROUPS

Enriched homolog groups with UniRef50 entries

Enriched homolog group 1

Enriched homolog group 2

(...)

Enriched homolog group N

UniRef50

Alignment
(MAFFT --auto)
+
HMM building
(hmmbuild)

hmmsearch
(get ORFs missed by 'get_homologues')

HMM 1

HMM 2

HMM N

Pairwise
HMM-vs-HMM
comparisons
(hhalign)

Filters:
cov >= 50% of
longest HMM

e-value < 1e-10

All ORFs

Groups built by 'get_homologues'
are enriched with relevant ORFs

1 2 3   4 5

Collapse based on
significant results
using networkx

CG 1   CG 2   (...)   CG N

Jaccard Matrix based on shared
homolog groups between IMEs

JCVI rendering for selected IMEs

Final result: collapsed homolog groups
(initial groups enriched with relevant ORFs)

19

Supplementary Fig. 8 Bioinformatics workflow for IMEs.

The general workflow is divided into two parts. First, we re-annotated the ORFs of each IME and searched for potential homologs between them. Then we enriched these initial groups by searching the UniRef50 database and generated new HMM profiles. With these new HMMs we searched again within each IME to capture any potentially missing homolog. Finally, we performed HMM vs HMM[13] search to collapse similar groups into one. CG1, CG2...CGN are final collapsed homologous groups which are the basis for IME clustering, synteny conservation and gene content analyses shown in Supplementary Fig. 9, Fig. 8 and Supplementary Table 3, respectively.
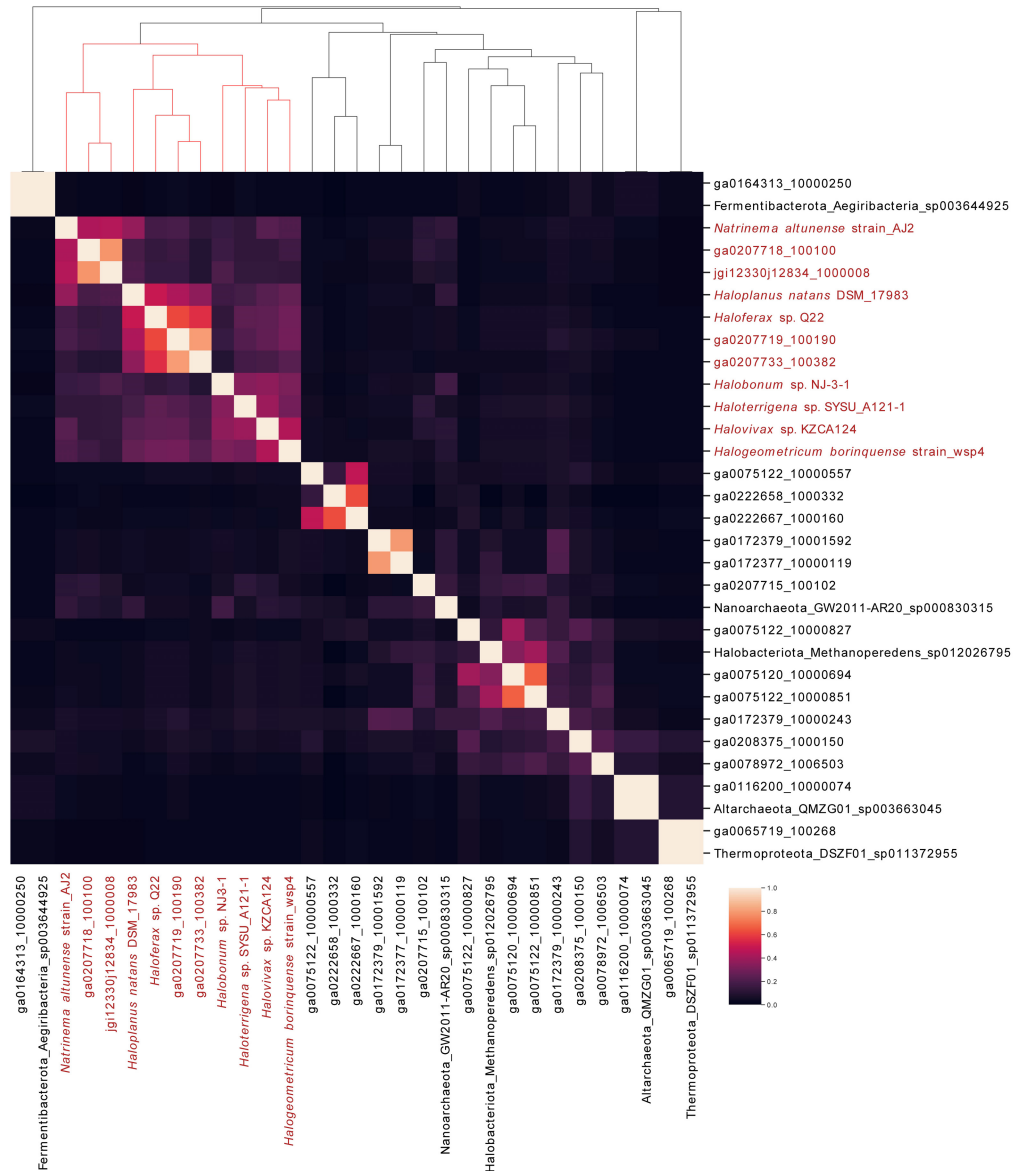
Supplementary Fig. 9 Clustering of IMEs from complete genomes, MAGs and metagenomic contigs based on gene content.

A distance metric based on the sharing of homologous genes between all IMEs was computed (see Methods). Then a pairwise distance matrix was built to perform hierarchical clustering. There is a clear cluster, marked in red, which contains all PCG IMEs and the DNA contig containing the crystallized Fsx1 (jgi12330j12834_1000008). This cluster of 11 IMEs was used for the synteny conservation analysis shown in Fig. 8.

Supplementary Fig. 10 Unrooted phylogenetic tree of Archaea/Eukarya fusexins and structure-based tree of all fusexins.

a Unrooted phylogenetic sequence tree of archaeal and eukaryotic fusexins. Archaeal Fsx1s from cultivated species are shown in red; eukaryotic HAP2 major clades are indicated in colors. Relevant branch support values are indicated, raw tree available in Supplementary Data 5.

b Monomer models based on the $Fsx1_E$ crystal structure and experimental structures of other fusexins were compared using flexible structural alignment to build a minimum evolutionary tree. Scale bar represents distance as 1-TMscore, which supports their homology.

Supplementary Fig. 11 Uncropped gel images from Supplementary Fig. 2.

a SDS-PAGE gel stained with Coomassie G-250. The section indicated by a red dashed square is used in Supplementary Fig. 2a**.** n=2.

b BN-PAGE gel stained with Coomassie G-250. The section indicated by a red dashed square is used in Supplementary Fig. 2b. n=2.
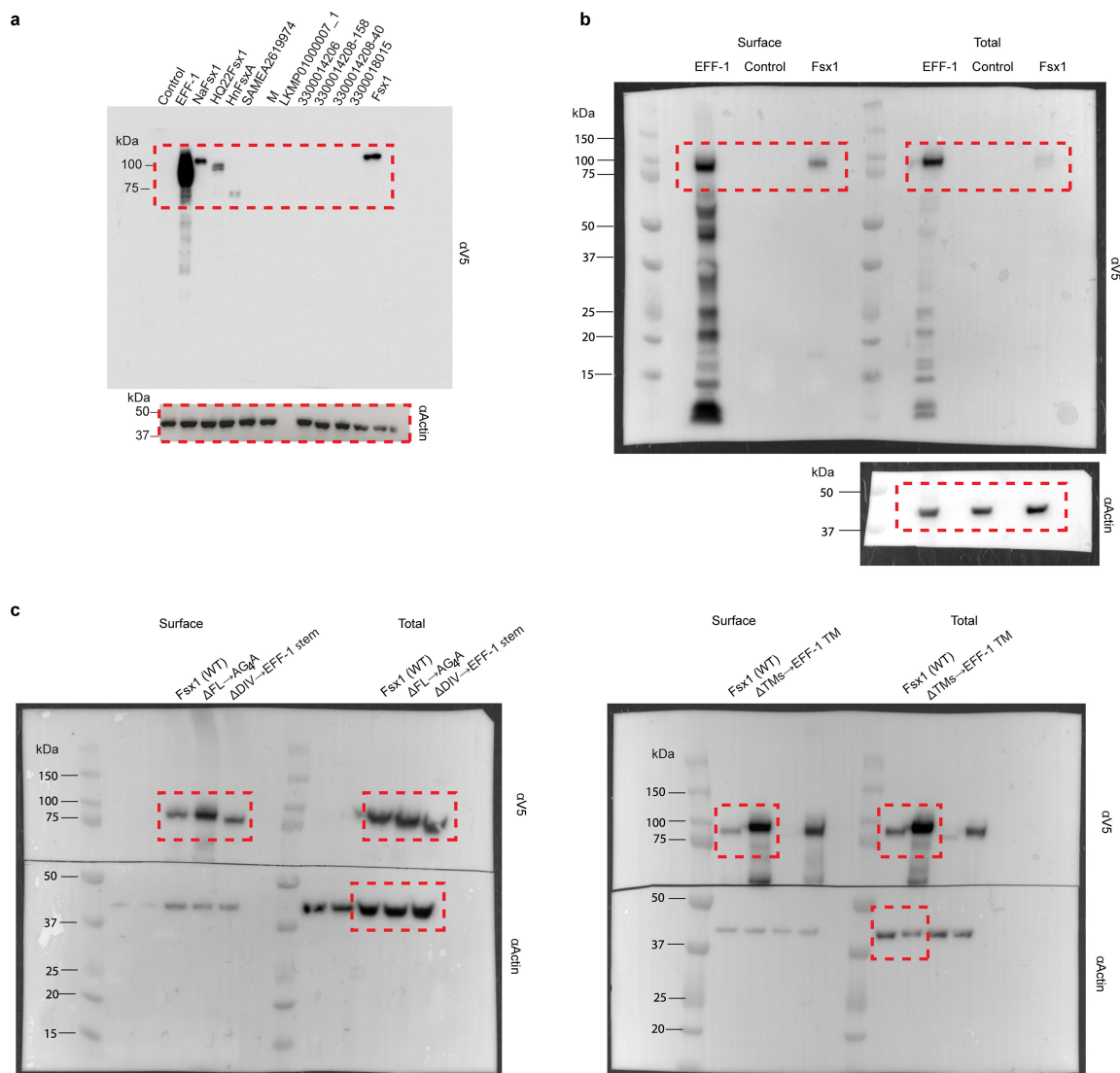
Supplementary Fig. 12 Uncropped Western blot images from Supplementary Fig. 1c and Fig. 5d, e.

a Western blot probed with anti-V5 (upper) and anti-actin (lower) antibodies. The sections indicated by red dashed squares are used in Supplementary Fig. 1c. n=3.

b Western blot probed with anti-V5 (upper) and anti-actin (lower) antibodies. The sections indicated by red dashed squares are used in Fig. 5d. n=3.

c Western blots probed with anti-V5 (upper) and anti-actin (lower) antibodies. The sections indicated by red dashed squares are used in Fig. 5e. n=3.

Supplementary Table 1. Fsx1s in genomes with assigned taxonomy

Fsx1s in Pure Culture Genomes (PCGs)

Sequence ID	Species	Taxonomy
WP_058826362.1	*Haloferax* sp. Q22	Archaea › Euryarchaeota › Stenosarchaea group › Halobacteria › Haloferacales › Haloferacaceae
WP_144240185.1	*Natrinema altunense* (AJ2)	Archaea › Euryarchaeota › Stenosarchaea group › Halobacteria › Natrialbales › Natrialbaceae
ELY83688.1	*Natrinema altunense* JCM12890)	Archaea › Euryarchaeota › Stenosarchaea group › Halobacteria › Natrialbales › Natrialbaceae
WP_157573584.1	*Haloplanus natans* DSM 17983	Archaea › Euryarchaeota › Stenosarchaea group › Halobacteria › Haloferacales › Haloferacaceae
WP_174701778.1	*Haloterrigena* sp. SYSU A121-1	Archaea › Euryarchaeota › Stenosarchaea group › Halobacteria › Natrialbales › Natrialbaceae
WP_179268568.1	*Halobonum* sp. NJ-3-1	Archaea › Euryarchaeota › Stenosarchaea group › Halobacteria › Haloferacales › Halorubraceae
WP_163487151.1	*Halogeometricum borinquense* strain wsp4	Archaea › Euryarchaeota › Stenosarchaea group › Halobacteria › Haloferacales › Haloferacaceae
WP_207587115.1	*Halovivax* sp. KZCA124	Archaea › Euryarchaeota › Stenosarchaea group › Halobacteria › Natrialbales › Natrialbaceae

Fsx1s in Metagenome-Assembled Genomes (MAGs)

Sequence ID	Assigned taxon	Taxonomy
MGYP000598426430	Halobacteriales	Archaea › Euryarchaeota › Stenosarchaea group › Halobacteria › Halobacteriales
LKMP01000007_1	Nanohaloarchaea archaeon B1-Br10_U2g21	Archaea › Euryarchaeota › Stenosarchaea group › Candidatus Nanohaloarchaeota
RLG58774.1	Candidatus Geothermarchaeota B85_G16	Archaea ›TACK group › Candidatus Geothermarchaeota
RLI53188.1	Candidatus Thorarchaeota archaeon	Archaea › Asgard group › Candidatus Thorarchaeota
RKX41251.1	Thermotogae bacterium	Bacteria › Thermotogae
RKZ11204.1	Candidatus Fermentibacteria bacterium	Bacteria › Candidatus Fermentibacteria
RLG94066.1	Candidatus Bathyarchaeota archaeon	Archaea ›TACK group › Candidatus Bathyarchaeota
AJF63093.1	archaeon GW2011_AR20	Archaea ›unclassified
HEX32987.1	Candidatus Aenigmarchaeota archaeon	Archaea › DPANN group › Candidatus Aenigmarchaeota
HDD44259.1	Candidatus Desulfofervidus auxilii	Bacteria › Proteobacteria › Deltaproteobacteria › Candidatus Desulfofervidaceae
HDI72891.1	Candidatus Altiarchaeales archaeon	Archaea › DPANN group › Candidatus Altiarchaeota › Candidatus Altiarchaeales
HHR27186.1	Candidatus Bathyarchaeota archaeon	Archaea ›TACK group › Candidatus Bathyarchaeota
NJD53946.1	Candidatus Methanoperedens sp.	Archaea › Euryarchaeota › Stenosarchaea group › Methanomicrobia › Methanosarcinales › Cand. Methanoperedenaceae
NOZ47386.1	Chlorobi bacterium	Bacteria › Chlorobi
HGF63239.1	Candidatus Micrarchaeota archaeon	Archaea › DPANN group › Candidatus Micrarchaeota
HID09282.1	Candidatus Micrarchaeota archaeon	Archaea › DPANN group › Candidatus Micrarchaeota

Supplementary Table 2. Fsx1$_E$ data collection and refinement statistics

Data collection

Space group	*C*2 (5)
Cell dimensions	
a, *b*, *c* (Å)	262.51, 111.33, 68.51
α, *β*, *γ* (°)	90, 100.709, 90
Wavelength (Å)	1.005
Resolution range (Å)	67.3-2.3 (2.38-2.30)[§]
Unique reflections	85618 (8536)
Multiplicity	4.2 (4.4)
Completeness (%)	99.5 (99.9)
Mean I / σI	11.4 (1.4)
Wilson B-factor	42.8
R_{merge}	0.100 (1.218)
R_{meas}	0.115 (1.385)
R_{pim}	0.055 (0.651)
$CC_{1/2}$	1.0 (0.58)
CC*	1.0 (0.86)

Refinement

Reflections used in refinement	85574 (6092)[**]
Reflections used for R_{free}	2012 (149)
R_{work}	0.199 (0.303)
R_{free}	0.243 (0.377)
Number of non-H atoms	11733
macromolecules / ligand / solvent	11051 / 66 / 616
Protein residues	1432
RMS	
bonds (Å)	0.004
angles (°)	0.58
Ramachandran favored / allowed / outliers (%)	98.9 / 1.1 / 0.0
Rotamer outliers (%)	0.2
Clashscore	2.5
Average B-factor	53.4
macromolecules / ligand / solvent	53.5 / 58.8 / 50.0

[§] Values in parenthesis are for the highest resolution shell
[**] The highest resolution shell used in refinement included reflections between 2.36 and 2.30 Å

Supplementary Table 3. Most common arCOGs from 11 IMEs[a]

Collapsed Group Name	IMEs count[b]	arCOG count[c]	arCOG	Category	Annotation
CG_2	11	22	arCOG00280, arCOG00285, arCOG06224	L	HerA helicase
CG_17	10	21	arCOG01241, arCOG01248, arCOG01250	X	XerC XerD/XerC family integrase
41684	10	3	arCOG01680, arCOG02808, arCOG04362	K	Transcriptional regulator containing HTH domain
43214	9	9	arCOG08903	S	Uncharacterized protein
CG_1	8	8	arCOG12186	S	Uncharacterized protein
CG_2	7	7	arCOG04816	U	TraG/TraD/VirD4 family enzyme, ATPase
43797	7	7	arCOG12187	S	Uncharacterized membrane protein
43810	7	7	arCOG10296	S	Uncharacterized membrane protein
43833	7	7	arCOG08907	S	Uncharacterized protein
43868	7	7	arCOG10381	S	Uncharacterized protein
CG_2	6	7	arCOG00467	L	Cdc6-related protein, AAA superfamily ATPase
CG_2	6	6	arCOG07496	U	VirB4, Type IV secretory pathway
42763	6	6	arCOG06216	K	Transcriptional regulator
CG_2	5	5	arCOG01308	O	ATPase of the AAA+ class , CDC48 family
CG_21	3	3	arCOG07871	K	Helicase
CG_2	2	2	arCOG00439	L	ATPase involved in replication control
CG_2	2	2	arCOG03779	V	GTPase subunit of restriction endonuclease
CG_2	2	2	arCOG05935	R	Helicase of FtsK superfamily
CG_21	2	2	arCOG00878	V	restriction-modification related helicase
CG_9	1	1	arCOG03600	E	Transglutaminase-like cysteine protease
CG_21	1	1	arCOG04818	K	Superfamily II DNA/RNA helicase, SNF2 family

a. Collapsed Homology Groups (Supplementary Fig. 8) corresponding to the 11 IME clusters (Supplementary Fig. 9) were analyzed using HMMER against the arCOGs database. Collapsed Homology Groups with zero identified arCOGs are not shown. Full dataset with results is in Supplementary Data 3.

b. Number of IMEs where the indicated arCOGs are present.

c. Total number of ORFs belonging to arCOGs in the next column identified in the set of 11 IMEs.

Supplementary Table 4. IMEs carrying the *fsx1* gene in completely sequenced genomes

Species with *fsx1*	NCBI TaxID	PATRIC ID	sequence ID[a]	ME start k-mer[b]	ME end k-mer[b]	Length ME k-mer	ME start CG[c]	ME end CG[c]	Length ME CG	Species w/o *fsx1*[d]	NCBI TaxID	PATRIC ID	ANI[e]
Haloplanus natans DSM 17983	926690	926690.3	ATYM01000002	1422500	1526500	104001	1422548	1535558	113011	*Haloplanus* sp. CBA1112	1547898	1547898.3	88.0
Natrinema altunense strain AJ2	222984	222984.5	JNCS01000001	496500	593500	97001	497005	591892	94888	*Natrinema altunense* strain 4.1R	222984	222984.10	98.0
Halobonum sp. NJ-3-1	2743089	2743089.3	CP058579	1918000	2078500	160501	1906722	2078630	171909	*Halobonum* sp. Gai3-2	2743090	2743090.3	85.0
Haloferax sp. Q22	1526048	1526048.3	LOEP01000012	1	56511	56511	1	56511	56511	*Haloferax gibbonsii* strain LR2-5	35746	35746.12	94.8
Haloterrigena sp. SYSU A121-1	2496101	2496101.3	JABURA010000001	1761500	1860500	99001	1761690	1860499	98810	*Haloterrigena turkmenica* DSM 5511	543526	543526.13	92.4
Halogeometricum borinquense strain wsp4	60847	60847.21	CP048739	2797000	2827000	30001	2763703	2853374	89672	*Halogeometricum borinquense* strain wsp3	60847	60847.22	99.6
Halovivax sp. KZCA124	2817025	2817025.3	NZ_CP071597	3085000	3179500	94501	_f	--	--	--	--	--	--

a. Genomic contig carrying the IME.

b. Sequence coordinates of the start and end of the IME identified by k-mer spectrum.

c. Sequence coordinates of the start and end of the IME identified by comparative genomics (CG).

d. Closest species not carrying the *fsx1* gene with a completely sequenced genome (used for CG analysis).

e. Average nucleotide identity between the complete genomes of compared species.

f. No species with a completely sequenced genome was similar enough to *Halovivax* sp. KZCA124 to compute an accurate estimate of IME's insertion sites with CG.

Supplementary Table 5. Synthesized archaeal fusexin genes for fusogenic tests in mammalian cells

Synthesized plasmids	Accession number/Sequence	Species/Assembly source
pBPT01	WP_007110832	*Natrinema altunense*
pBPT02	WP_058826362	*Haloferax* sp.Q22
pBPT03	WP_049937247	*Haloplanus natans*
pBPT04	SAMEA2619974_10776_4	MAG
pBPT05	LKMP01000007_1	Nanohaloarchaea archaeon B1-Br10_U2g21 LB-BRINE-C121
pBPT06	3300014206-Ga0172377-10000119-870930-129	unassembled metagenome
pBPT07	3300014208-Ga0172379-10000243-871512-158	unassembled metagenome
pBPT08	3300014208-Ga0172379-10001592-871560-40	unassembled metagenome
pBPT10	3300018015-Ga0187866_1000629|915963_9	unassembled metagenome
pBPT11	3300000868-JGI12330J12834-1000008-299010-8, **Fsx1**	unassembled metagenome

Supplementary Table 6. Plasmids used in this study

Plasmid name	Description	Use	Source
pLJFX11B	pLJ6-Fsx1$_E$	For SAXS and SEC-MALS (Supplementary Fig. 2)	this study, amplified from pBPT11
pLJFX11B_T369C	pLJ6-Fsx1$_E$-T369C mutant	For crystallographic study (Figs. 2-3; Supplementary Fig. 2)	this study, amplified from pBPT11
pBPT01	*Natrinema altunense fsx1* synthesized into pGene/V5-His	Inducible expression in mammalian cells (Supplementary Fig.1)	this study
pBPT02	*Haloferax* sp. Q22 *fsx1* synthesized into pGene/V5-His	Inducible expression in mammalian cells (Supplementary Fig.1)	this study
pBPT03	*Haloplanus natans fsx1* synthesized into pGene/V5-His	Inducible expression in mammalian cells (Supplementary Fig. 1)	this study
pBPT04	SAMEA2619974 synthesized into pGene/V5-His	Inducible expression in mammalian cells (Supplementary Fig. 1)	this study
pBPT05	LKMP01000007_1 synthesized into pGene/V5-His	Inducible expression in mammalian cells (Supplementary Fig. 1)	this study
pBPT06	3300014206 synthesized into pGene/V5-His	Inducible expression in mammalian cells (Supplementary Fig. 1)	this study
pBPT07	3300014208-158 synthesized into pGene/V5-His	Inducible expression in mammalian cells (Supplementary Fig. 1)	this study
pBPT08	3300014208-40 synthesized into pGene/V5-His	Inducible expression in mammalian cells (Supplementary Fig. 1)	this study
pBPT10	3300018015 synthesized into pGene/V5-His	Inducible expression in mammalian cells (Supplementary Fig. 1)	this study
pBPT11	*fsx1* synthesized into pGene/V5-His	Inducible expression in mammalian cells (Supplementary Fig. 1)	this study
pGene/V5-His	pGene/V5-His	GeneSwitch™ inducible Mammalian Expression	INVITROGEN
pSwitch	pSwitch	Regulatory vector for Mifepristone induction	INVITROGEN
pOA34	pGene::EFF-1-V5	*C. elegans eff-1* fused to a C-terminal V5 tag (EFF-1-V5) in pGene	Avinoam et al., 2011[14]
pCI H2B-RFP	pCI::H2B-RFP	A CAG promoter (CMV immediate early enhancer and chicken beta actin promoter) and IRES controlled Histone2B-mRFP1 reporter.	Addgene plasmid # 92398[15]
pCI H2B-GFP	pCI::H2B-GFP	A CAG promoter (CMV immediate early enhancer and chicken beta actin promoter) and IRES controlled Histone2B-EGFP reporter.	Addgene plasmid # 92399[15]
pCAGIG	pCAGIG	A CAG promoter (CMV immediate early enhancer and chicken beta actin promoter) and IRES controlled EGFP reporter.	Addgene plasmid # 11159[16]
pNB25	pCAGIGnes	Intermediate construct to create pNB32	this study
pNB32	pCI::GFPnes	Content-mixing, Fig. 4a-c	this study
pRFPnes	DsRed2 with a nuclear export signal	Content-mixing, Fig. 4a-c	Avinoam et al., 2011[14]
pXL27	pCI::Fsx1-V5::H2B-RFP	Content-mixing, Fig. 4a-c	this study
pXL28	pCI::Fsx1-V5::H2B-GFP	Content-mixing, Fig. 4a-c; live imaging of fusion, Fig. 4g	this study
pXL29	pCI::AtHAP2-V5::H2B-RFP	Content-mixing, Fig. 4a-c; Multinucleation assay (Supplementary Fig. 1)	this study
pXL30	pCI::AtHAP2-V5::H2B-GFP	Content-mixing, Fig. 4a-c; Multinucleation assay (Supplementary Fig. 1)	this study
pXL49	pCI::Fsx1-V5::GFPnes	Content-mixing, Fig. 4d-e	this study
pNB34	pCI::EFF-1-V5::GFPnes	Content-mixing, Fig. 4d-e	this study
pXL68	pCI::VSV-G::GFPnes	Content-mixing, Fig. 4d-e	this study
pOA19	pCAGGS::EFF-1-V5	Surface biotinylation of EFF-1 (Fig. 5d)	Avinoam et al., 2011[14]
pXL50	pCAGGS::Fsx1-V5	Surface biotinylation of Fsx1 (Fig. 5d)	this study
myr-mCherry	myr-mCherry	mCherry linked to a myristoylated and palmitoylated peptide, live imaging of fusion (Fig. 4g)	Dunsing et al., Sci. Rep. 2018[17]
myr-EGFP	myr-EGFP	EGFP linked to a myristoylated and palmitoylated peptide (Supplementary Fig. 1)	Dunsing et al., Sci. Rep. 2018[17]
pXL21	pCI::NaFsx1-V5::H2B-RFP	Multinucleation assay (Supplementary Fig. 1)	this study
pXL22	pCI::NaFsx1-V5::H2B-GFP	Multinucleation assay (Supplementary Fig. 1)	this study
pXL23	pCI::HQ22Fsx1-V5::H2B-RFP	Multinucleation assay (Supplementary Fig. 1)	this study

Plasmid name	Description	Use	Source
pXL24	pCI::HQ22Fsx1-V5::H2B-GFP	Multinucleation assay (Supplementary Fig. 1)	this study
pXL25	pCI::HnFsx1-V5::H2B-RFP	Multinucleation assay (Supplementary Fig. 1)	this study, subcloned from pBPT03 with modification of complete signal peptide
pXL26	pCI::HnFsx1-V5::H2B-GFP	Multinucleation assay (Supplementary Fig. 1)	this study, subcloned from pBPT03 with modification of complete signal peptide
pXL57	pCI::Fsx1-ΔFL-AG₄A::GFPnes	Content-mixing, Fig. 5a-c	this study
pXL58	pCI::Fsx1-ΔFL-AG₄A::H2B-RFP	Content-mixing, Fig. 5a-c	this study
pXL63	pCI::Fsx1-ΔDIV-EFF-1-stem::H2B-RFP	Content-mixing, Fig. 5a-c	this study
pXL64	pCI::Fsx1-ΔDIV-EFF-1-stem::GFPnes	Content-mixing, Fig. 5a-c	this study
pXL108	pCAGGS::Fsx1-ΔDIV-EFF-1-stem	Surface biotinylation of Fsx1-ΔDIV-EFF-1-stem mutant (Fig. 5e)	this study
pXL82	pCI::Fsx1-WT-FLAG-3TMs::H2B-RFP	Surface expression tests, FLAG tag inserted before the first TM segment of Fsx1 (Fig. 5f)	this study
pXL86	pCI::Fsx1-ΔFL-AG₄A-FLAG-3TMs::H2B-RFP	Surface expression tests, FLAG tag inserted before the first TM segment of Fsx1-ΔFL-AG₄A mutant (Fig. 5f)	this study
pXL92	pCI::Fsx1-ΔDIV-EFF-1-stem-FLAG-3TMs::H2B-RFP	Surface expression tests, FLAG tag inserted before the first TM segment of Fsx1-ΔDIV-EFF-1-stem mutant (Fig. 5f)	this study
pOA20	pCAGGS::AFF-1-FLAG	*C. elegans aff-1* fused to a C-terminal FLAG tag (AFF-1-FLAG) in pCAGGS	Avinoam et al., 2011[14]
pXL100	pCI::AFF-1-FLAG::H2B-RFP	Surface expression tests of AFF-1 (Fig. 5f)	this study
pXL106	pCAGGS-Fsx1-ΔFL-AG₄A	Surface biotinylation of Fsx1-ΔFL-AG₄A mutant (Fig. 5e)	this study
pXL123	pCAGGS-Fsx1ΔTMs-EFF-1 TM	Surface biotinylation of Fsx1ΔTMs-EFF-1 TM mutant (Fig. 5e)	this study
pXL119	pCI::Fsx1ΔTMs-EFF-1 TM::H2B-RFP	Content-mixing, Fig. 5a-c; Surface expression tests, FLAG tag inserted before the EFF-1 TM region (Fig. 5f)	this study
pXL120	pCI::Fsx1ΔTMs-EFF-1 TM::GFPnes	Content-mixing, Fig. 5a-c	this study
pXL115	pCI::Fsx1ΔTMs-GPI::H2B-RFP	Content-mixing, Fig. 5a-c; Surface expression tests, FLAG tag inserted before the GPI (Fig. 5f)	this study
pXL116	pCI::Fsx1ΔTMs-GPI::GFPnes	Content-mixing, Fig. 5a-c	this study
pXL117	pCI::AtHAP2ΔTM-GPI::H2B-RFP	Content-mixing, Fig. 5a-c; Surface expression tests, FLAG tag inserted before the GPI (Fig. 5f)	this study
pXL118	pCI::AtHAP2ΔTM-GPI::GFPnes	Content-mixing, Fig. 5a-c	this study

Supplementary Table 7. Primers used in this study

Primer name	Sequence	Description
SNFX11_F	CGTAGCTGAAACCGGTGATTCAATCACGTATAACTCTGG	Forward primer for cloning Fsx1$_E$ and T369C mutant into pLJ6 with AgeI
SNFX11_R	GGTGATGGTGCTCGAGGGAACCAGAACCTCCGAA	Reverse primer for cloning Fsx1$_E$ and T369C mutant into pLJ6 with XhoI
SNFX11_T369C_F	ACTGTAtgcGCCACCGTTGAGAATGTC	Forward primer for T369C mutant
SNFX11_T369C_R	GGTGGCgcaTACAGTTCCCTCATCTCCCTC	Reverse primer for T369C mutant
seq_up	GCTGGTTGTTGTGCTGTCTCATC	Sequencing primer for pLJ6
seq_down	CACCAGCCACCACCTTCTGATAG	Sequencing primer for pLJ6
LXH1	GATGGTGCGATTGCGGAT	Sequencing primer for pBPT01
LXH2	CCTACGAGAATGGGCAGA	Sequencing primer for pBPT01
LXH3	TTGCTGGCAGAGAAATGA	Sequencing primer for pBPT02
LXH4	TGATGTACCCCGAGTTCA	Sequencing primer for pBPT02
LXH5	GGATGAAATCTTCAGAAC	Sequencing primer for pBPT03
LXH6	ACTGTCTCGAAGCCGGTT	Sequencing primer for pBPT03
LXH7	CAAAATCACCCTCACATC	Sequencing primer for pBPT04
LXH8	CCTACAATATTAAGTTGTG	Sequencing primer for pBPT04
LXH9	TGAGTCTGAATGGATTAT	Sequencing primer for pBPT05
LXH10	TAGGACTACAGCGAAAAT	Sequencing primer for pBPT05
LXH11	TTGGGGAGGAAATGTAAA	Sequencing primer for pBPT06
LXH12	TAGAAGAATAAATATTCC	Sequencing primer for pBPT06
LXH13	TCCTCTTCCCTCGGAGAA	Sequencing primer for pBPT07
LXH14	CCTACTCAGGTAACGTAA	Sequencing primer for pBPT07
LXH15	CAGTAACAATAAATGGTG	Sequencing primer for pBPT08
LXH16	CAGAAGAATAAACATTCC	Sequencing primer for pBPT08
LXH17	AACAATAGGACAAGCAAA	Sequencing primer for pBPT10
LXH18	ACCAAAAATATTGTCTGC	Sequencing primer for pBPT10
LXH19	AGCATACATAGACAACCC	Sequencing primer for pBPT11, Fsx1
LXH20	ACGTCGATGCCGGAGAAA	Sequencing primer for pBPT11, Fsx1
pGene FW	CTGCTCAACCTTCCTATC	pGene backbone sequencing forward primer
pGene REV	TTAGGAAAGGACAGTGGGAGTG	pGene backbone sequencing reverse primer
PCA-5	GGTTCGGCTTCTGGCGTGTGACC	pCI::H2B-RFP/H2B-GFP/GFPnes backbones sequencing forward primer
IRES-REV	GCATTCCTTTGGCGAGAG	pCI::H2B-RFP/H2B-GFP/GFPnes backbones sequencing reverse primer
pCAGGS FW	GCAACGTGCTGGTTGTTGTGCTGTC	pCAGGS backbone sequencing forward primer
pCAGGS RV	TCCCATATGTCCTTCCGAGTGA	pCAGGS backbone sequencing reverse primer
LXH24	CGGGGTACCATGAGACGTGCAGCATTG	Forward primer for cloning Fsx1 and its mutants into pCAGGS vector with KpnI
LXH42	CTAGCTAGCGGTACCATGAGACGTGCAGCATTGATT	Forward primer for cloning Fsx1 into pCI::H2B-RFP/H2B-GFP/GFPnes vectors with NheI and KpnI
LXH44	CTAGCTAGCGGTACCATGGAACCGCCGTTTGAGTGG	Forward primer for cloning EFF-1 into pCI::GFPnes vector with NheI and KpnI
LXH45	CTAGCTAGCGGTACCATGGTGAACGCGATTTTAATG	Forward primer for cloning AtHAP2 into pCI::H2B-RFP/GFP vectors with NheI and KpnI
LXH79	TCCCCCGGGCTAATGGTGATGGTGATGATGACC	Reverse primer for cloning fusexins into pCI vectors with SmaI which binds to 6xHis tag
LXH81	CTAGCTAGCTCAATGGTGATGGTGATGATGACC	Reverse primer for cloning Fsx1 and its mutants into pCAGGS vector with NheI
LXH111	CTAGCTAGCATGAAGTGCCTTTTGTACTTAG	Forward primer for cloning VSV-G into pCI::GFPnes vector with NheI

Primer name	Sequence	Description
LXH112	TCCCCCGGGTTACTTTCCAAGTCGGTTCATC	Reverse primer for cloning VSV-G into pCI::GFPnes vector with SmaI
LXH39	CTAGCTAGCGGTACCATGCGGGCGGTGTCTGATTTC	Forward primer for cloning NaFsx1 into pCI::H2B-RFP/GFP vectors with NheI and KpnI
LXH40	CTAGCTAGCGGTACCATGAAAAACGGGTTGAAGGCC	Forward primer for cloning HQ22Fsx1 into pCI::H2B-RFP/GFP vectors with NheI and KpnI
LXH134	CTAGCTAGCATGGTGAAACGAGTGGGTAATTGTTGG AAGGCCTCAGTAGCGGCATTCTTCCTTCTCATGTTCACTGCATTT	Forward primer for cloning HnFsx1 into pCI::H2B-RFP/GFP vectors with NheI; containing modification of complete signal peptide
LXH107	GCGGAAGGTACAGCAGGTACGCCGGTGGAGGTGGAGCTGATTACGA GATCTATTGTTT	Forward primer for cloning downstream of Fsx1-ΔFL-AG$_4$A mutant by overlap PCR
LXH108	AAACAATAGATCTCGTAATCAGCTCCACCTCCACCGGCGTACCTGCTG TACCTTCCGC	Reverse primer for cloning upstream of Fsx1-ΔFL-AG$_4$A mutant by overlap PCR
LXH101	ACCGGTATCCAGCAGGAAATCGATCTTGTT	Forward primer 1 for cloning Fsx1-ΔDIV-EFF-1-stem by overlap PCR
LXH102	AACAAGATCGATTTCCTGCTGGATACCGGT	Reverse primer 1 for cloning Fsx1-ΔDIV-EFF-1-stem by overlap PCR
LXH103	ATGATTGCTACGGATCAGGACGATGATTCA	Forward primer 2 for cloning Fsx1-ΔDIV-EFF-1-stem by overlap PCR
LXH104	TGAATCATCGTCCTGATCCGTAGCAATCAT	Reverse primer 2 for cloning Fsx1-ΔDIV-EFF-1-stem by overlap PCR
LXH128	TGTTCGGAGGTTCTGGTTCCGACTACAAGGACGACGATGACAAAGGA GATCTGCTTAC	Forward primer for cloning downstream of Fsx1-WT/mutants-FLAG by overlap PCR
LXH129	GGAACCAGAACCTCCGAACA	Reverse primer for cloning upstream of Fsx1-WT/mutants-FLAG by overlap PCR
LXH135	CTAGCTAGCATGGTACTGTGGCAATGGTCAATAG	Forward primer for cloning *C. elegans* AFF-1-FLAG into pCI::H2B-RFP vector with NheI
LXH136	TCCCCCGGGTTATTTGTCATCGTCGTCCTTGTAGTC	Reverse primer for cloning *C. elegans* AFF-1-FLAG into pCI::H2B-RFP vector with SmaI
LXH140	GACGGGTAGTACCTGAAGTGGTTCCACTTCCTTTATTTGGAGAACCT CCTTTGTCATCGTCGTCCTTGTAGTCGGAACCAGAACCTCCG	Reverse primer 1 for fusing GPI signal from DAF to Fsx1
LXH141	TCCCCCGGGCTAAGTCAGCAAGCCCATGGTTACTAGCGTCCCAAGC AAACCTGTCAACGTGAAACACGTGTGCCCAGATAGAAGACGGGTAG TACCTGAAGTG	Reverse primer 2 for fusing GPI signal from DAF to Fsx1; Reverse primer for cloning downstream of AtHAP2ΔTM-GPI mutant by overlap PCR
LXH142	AATACGTTTGCTTAAGCTGGGGTGGAAGCGACTACAAGGACGACGA T	Forward primer for cloning downstream of AtHAP2ΔTM-GPI mutant by overlap PCR
LXH143	CCAGCTTAAGCAAACGTATT	Reverse primer for cloning upstream of AtHAP2ΔTM-GPI mutant by overlap PCR
LXH144	GGAGGTTCTGGTTCCGACTACAAGGACGACGATGACAAAATTGTTG TGTATCTC	Forward primer for cloning downstream of Fsx1ΔTMs-EFF-1 TM mutant by overlap PCR which contains one FLAG tag

Supplementary References

1. Lu, X. *et al.* Double Lock of a Human Neutralizing and Protective Monoclonal Antibody Targeting the Yellow Fever Virus Envelope. *Cell Rep.* **26**, 438–446.e5 (2019).

2. Voss, J. E. *et al.* Glycoprotein organization of Chikungunya virus particles revealed by X-ray crystallography. *Nature* **468**, 709–712 (2010).

3. Modis, Y., Ogata, S., Clements, D. & Harrison, S. C. A ligand-binding pocket in the dengue virus envelope glycoprotein. *Proc. Natl. Acad. Sci. U. S. A.* **100**, 6986–6991 (2003).

4. Gibbons, D. L. *et al.* Conformational change and protein-protein interactions of the fusion protein of Semliki Forest virus. *Nature* **427**, 320–325 (2004).

5. Rey, F. A., Heinz, F. X., Mandl, C., Kunz, C. & Harrison, S. C. The envelope glycoprotein from tick-borne encephalitis virus at 2 Å resolution. *Nature* **375**, 291–298 (1995).

6. Fedry, J. *et al.* Evolutionary diversification of the HAP2 membrane insertion motifs to drive gamete fusion across eukaryotes. *PLoS Biol.* **16**, e2006357 (2018).

7. DuBois, R. M. *et al.* Functional and evolutionary insight from the crystal structure of rubella virus protein E1. *Nature* **493**, 552–556 (2013).

8. Fédry, J. *et al.* The Ancient Gamete Fusogen HAP2 Is a Eukaryotic Class II Fusion Protein. *Cell* **168**, 904–915.e10 (2017).

9. Guardado-Calvo, P. *et al.* Mechanistic Insight into Bunyavirus-Induced Membrane Fusion from Structure-Function Analyses of the Hantavirus Envelope Glycoprotein Gc. *PLoS Pathog.* **12**, e1005813 (2016).

10. Dessau, M. & Modis, Y. Crystal structure of glycoprotein C from Rift Valley fever virus. *Proc. Natl. Acad. Sci. U. S. A.* **110**, 1696–1701 (2013).

11. Kielian, M. Mechanisms of Virus Membrane Fusion Proteins. *Annu. Rev. Virol.* **1**, 171–189 (2014).

12. Baquero, E., Fedry, J., Legrand, P., Krey, T. & Rey, F. A. Species-Specific Functional Regions of the Green Alga Gamete Fusion Protein HAP2 Revealed by Structural Studies. *Structure* **27**, 113–124.e4 (2019).

13. Söding, J. Protein homology detection by HMM–HMM comparison. *Bioinformatics* **21**, 951–960 (2004).

14. Avinoam, O. *et al.* Conserved eukaryotic fusogens can fuse viral envelopes to cells. *Science* **332**, 589–592 (2011).

15. Williams, R. M. *et al.* Genome and epigenome engineering CRISPR toolkit for in vivo modulation of cis-regulatory interactions and gene expression in the chicken embryo. *Development* **145**, dev160333 (2018).

16. Matsuda, T. & Cepko, C. L. Electroporation and RNA interference in the rodent retina in vivo and in vitro. *Proc. Natl. Acad. Sci. U. S. A.* **101**, 16–22 (2004).

17. Dunsing, V. *et al.* Optimal fluorescent protein tags for quantifying protein oligomerization in living cells. *Sci. Rep.* **8**, 1–12 (2018).

nature portfolio

Corresponding author(s): Martin Graña, Héctor Romero, Pablo S. Aguilar, Luca Jovine, Benjamin Podbilewicz

Last updated by author(s): Jun 21, 2022

Reporting Summary

Nature Portfolio wishes to improve the reproducibility of the work that we publish. This form provides structure for consistency and transparency in reporting. For further information on Nature Portfolio policies, see our Editorial Policies and the Editorial Policy Checklist.

Statistics

For all statistical analyses, confirm that the following items are present in the figure legend, table legend, main text, or Methods section.

n/a	Confirmed	
☐	☒	The exact sample size (*n*) for each experimental group/condition, given as a discrete number and unit of measurement
☐	☒	A statement on whether measurements were taken from distinct samples or whether the same sample was measured repeatedly
☐	☒	The statistical test(s) used AND whether they are one- or two-sided *Only common tests should be described solely by name; describe more complex techniques in the Methods section.*
☒	☐	A description of all covariates tested
☐	☒	A description of any assumptions or corrections, such as tests of normality and adjustment for multiple comparisons
☐	☒	A full description of the statistical parameters including central tendency (e.g. means) or other basic estimates (e.g. regression coefficient) AND variation (e.g. standard deviation) or associated estimates of uncertainty (e.g. confidence intervals)
☐	☒	For null hypothesis testing, the test statistic (e.g. *F*, *t*, *r*) with confidence intervals, effect sizes, degrees of freedom and *P* value noted *Give P values as exact values whenever suitable.*
☒	☐	For Bayesian analysis, information on the choice of priors and Markov chain Monte Carlo settings
☒	☐	For hierarchical and complex designs, identification of the appropriate level for tests and full reporting of outcomes
☒	☐	Estimates of effect sizes (e.g. Cohen's *d*, Pearson's *r*), indicating how they were calculated

Our web collection on statistics for biologists contains articles on many of the points above.

Software and code

Policy information about availability of computer code

Data collection	MetaMorph(v7.8.1.0), Micro-Manager(v1.4.22), MicroMounts(MiTeGen) , MXCuBE3, ZEN.
Data analysis	Adobe Illustrator 2021 , Adobe Photoshop CS6, AlphaFold2(v2.1.1), AlphaFold-Multimer(v2.1.1),ANODE(v2013/1), APBS(v1.5), ASTRA(v7.1.3), BioRender, BLASTP,ChimeraX(v1.2.4), ClustalO(v1.2.2) , ConSurf, Coot(v0.8.9.3-0.9.6), CRYSOL(ATSAS v3.0.3), Dali(v5), DAMMIF(ATSAS v3.0.2) , DSSP(v4.0-67), EMBOSS(v6.5.7), ETE Toolkit, FastME(v2.0), FATCAT(v2.0), GraphPad Prism 9, HHblits(v3.3.0), HH-suite(v3.3.0), HMMER (v3.3.2), I-TASSER(v5.1), ImageJ(v1.53c), IQ-TREE2(v1.6.12) , ISOLDE(v1.1.0), JCVI, kClust, MAFFT (v7.310) , MCscan(v0.8), MetaMorph (v7.8.1.0), ModelFinder, MODELLER(v10.2), MolProbity(v4.5.1), MOLREP(v11.7.03), PDB2PQR(v2.1.2), PDBeFold, PDBsum, Pfam(v33), Phaser (v2.8.3), PHENIX AutoBuild(v1.19.2) , PIC, PISA(v1.52), POLARRFN(v7.1.010), POSA, PRIMUS(ATSAS v3.0.3), PyMOL(v2.4.2), Python, R, trim-Al, TMalign(v20210224) , TMHMM(v2.0), TOPCONS(v2.0), XDS(version Jan 31, 2020 BUILT=20200417) , YASARA2(v.21.7.1). All relevant codes, notebooks and datasets necessary for: HHblits and Hmmer searches and comparisons (Fig. 1a, Supplementary Fig. 1a); Kmer spectra analyses (Fig. 7); IMEs clustering, content and synteny analyses (Fig. 8, Supplementary Figs. 8, 9 and Supplementary Tables 3, 4), protein sequence and structure-based comparisons (Supplementary Fig. 9) are available on GitHub (https://github.com/DessimozLab/Archaeal-Fusexins) and Zenodo (https://doi.org/10.5281/zenodo.6669786).

For manuscripts utilizing custom algorithms or software that are central to the research but not yet described in published literature, software must be made available to editors and reviewers. We strongly encourage code deposition in a community repository (e.g. GitHub). See the Nature Portfolio guidelines for submitting code & software for further information.

Data

Policy information about [availability of data](#)

All manuscripts must include a [data availability statement](#). This statement should provide the following information, where applicable:

- Accession codes, unique identifiers, or web links for publicly available datasets
- A description of any restrictions on data availability
- For clinical datasets or third party data, please ensure that the statement adheres to our [policy](#)

All relevant data are included in the manuscript and as Supplementary Information files (see Suppl. Inf. Guide). Crystallographic structure factors and atomic coordinates have been deposited in the Protein Data Bank under accession code 7P4L.

Field-specific reporting

Please select the one below that is the best fit for your research. If you are not sure, read the appropriate sections before making your selection.

[✗] Life sciences   [ ] Behavioural & social sciences   [ ] Ecological, evolutionary & environmental sciences

For a reference copy of the document with all sections, see [nature.com/documents/nr-reporting-summary-flat.pdf](#)

Life sciences study design

All studies must disclose on these points even when the disclosure is negative.

Sample size	We did not perform calculations to determine sample sizes; however, when we added more data the conclusions of the experiments did not change.
Data exclusions	No data were excluded from the analyses.
Replication	Functional experiments were independently repeated on different days and using independently transfected cells. Interobserver error was estimated for counting of multinucleated cells, cells in contact, and content-mixing experiments: the differences in percentages of multinucleation and content mixing obtained by two observers was <10%.
Randomization	In our study we did not allocate experimental groups; thus, randomization was not necessary.
Blinding	Counting of content mixing and multinucleation was made blind for the experiments included in Figs. 4f and 5b. Other experiments in this study were analyzed using the same methodologies and all data were included in the results reported.

Reporting for specific materials, systems and methods

We require information from authors about some types of materials, experimental systems and methods used in many studies. Here, indicate whether each material, system or method listed is relevant to your study. If you are not sure if a list item applies to your research, read the appropriate section before selecting a response.

Materials & experimental systems

n/a	Involved in the study
[ ]	[✗] Antibodies
[ ]	[✗] Eukaryotic cell lines
[✗]	[ ] Palaeontology and archaeology
[✗]	[ ] Animals and other organisms
[✗]	[ ] Human research participants
[✗]	[ ] Clinical data
[✗]	[ ] Dual use research of concern

Methods

n/a	Involved in the study
[✗]	[ ] ChIP-seq
[✗]	[ ] Flow cytometry
[✗]	[ ] MRI-based neuroimaging

Antibodies

Antibodies used	Anti-FLAG M2, catalog number F3165, lot number 065K6236 (Sigma); Anti-V5 mouse monoclonal, catalog number R960-25, lot number 2001339 (Invitrogen/Life Science); Donkey anti-mouse coupled to Alexa Fluor 488, catalog number A21202, lot number 1423052 (Invitrogen); Mouse Anti-Actin monoclonal C4, catalog number 691001, lot number Q1642 (MP Biomedicals); HRP-conjugated goat anti-mouse, catalog number 115-035-003, lot number n/a (Jackson ImmunoResearch Laboratories, Inc.) .
Validation	Negative controls for immunofluorescence and western blots were un-transfected cells, cells transfected with vector alone or cells

transfected with a plasmid that did not contain the V5 or FLAG tags. Secondary antibodies were used on cells that were not incubated with first antibodies to determine the background. Positive controls were tagged proteins that have been used previously in the lab (CeEFF-1-V5, CeAFF-1-FLAG, AtHAP2-V5). Additional information can be found here: https://www.sigmaaldrich.com/IL/en/product/sigma/f3165; https://www.thermofisher.com/antibody/product/V5-Tag-Antibody-Monoclonal/R960-25; https://www.mpbio.com/au/08691001-mouse-anti-actin-monoclonal-clone-c4-cf; https://www.jacksonimmuno.com/catalog/products/115-035-003.

Eukaryotic cell lines

Policy information about cell lines

Cell line source(s)	HEK293T: ATCC catalog number CRL-3216 (PMID 3031469); BHK-21: kindly obtained from Judith White (University of Virginia).
Authentication	None of the cell lines used were authenticated.
Mycoplasma contamination	Cells were routinely tested for mycoplasma and no contamination was detected; in particular, we confirmed that HEK293T were mycoplasma-free by using a PCR Mycoplasma Test Kit II (Applichem cat. no. A8994).
Commonly misidentified lines (See ICLAC register)	Cell lines HEK293T (CVCL_0063) and BHK-21 are not listed in version 8 of the Database of Cross-Contaminated or Misidentified Cell Lines.